An LES and RANS Study of the Canonical Shock-Turbulence Interaction

Thesis by
Noah Oakley Braun

In Partial Fulfillment of the Requirements for the
Degree of
Doctor of Philosophy

CALIFORNIA INSTITUTE OF TECHNOLOGY
Pasadena, California

2018
Defended 4 May 2018

Noah Oakley Braun
ORCID: 0000-0002-9710-0686

ACKNOWLEDGEMENTS

I would like to acknowledge my thesis advisers, Professors Dale Pullin and Dan Meiron, for their dedicated support and mentorship throughout my time at Caltech. I likewise thank Dr. Rob Gore for his guidance during the summers I spent at Los Alamos National Laboratory (LANL), and am grateful for the aid of Prof. Ralf Dieterding, who provided extensive help with numerical codes. I would also like to thank Dr. Daniel Livescu of LANL, Prof. John Dabiri of Stanford University, and Prof. Tim Colonius, Prof. Paul Dimotakis, Prof. Dennis Kochmann, Prof. Tony Leonard, Prof. Michael Ortiz, and many other members of the Caltech faculty for insightful discussions and their instruction throughout the years.

The contributions of past and present group members — Wan Cheng, Wouter Mostert, Dustin Summy, and Akshay Sridhar — and my fellow students at Caltech cannot be overstated. Likewise, this work would not have been possible without the support of Ms. Peggy Blue, Ms. Dimity Nelson, Ms. Christine Ramirez, Ms. Barbara McKinzie Slater, and the rest of the administrative staff.

Finally, this work was supported by the U.S. Department of Energy, subcontract #DE-AC52-06NA25396, and under Los Alamos National Laboratory (LANL) contract number 74372-001-09. This work used the Extreme Science and Engineering Discovery Environment (XSEDE) [86], which is supported by National Science Foundation grant number ACI-1053575.

ABSTRACT

The canonical problem of a nearly stationary, nearly planar shockwave passing through isotropic turbulence is investigated within high Reynolds number regimes. The subject flow contains a wide range of turbulent scales and is addressed in Large Eddy Simulation (LES) to relax the otherwise prohibitive computational cost of simulating these flows. Aliasing errors in the LES of the upstream isotropic turbulence are shown to interact with the mean compression of the shock in a problematic matter, and may result in nonphysical behavior such as a reduction in the dissipation rate as the flow crosses the shock. A method for the regularization of LES of shock-turbulence interactions is presented which is constructed to enforce that the energy content in the highest resolved wavenumbers decays as $k^{-5/3}$, and is computed locally in physical space at low computational cost. The application of the regularization to an existing subgrid scale model is shown to remove high wavenumber errors while maintaining agreement with DNS of forced and decaying isotropic turbulence. Comparisons to analytical models suggest that the regularization significantly improves the ability of the LES to predict amplifications in subgrid terms over the modeled shockwave.

The regularization method is then employed in high resolution LES intended to illustrate the physical behavior of the shocked, turbulent flow. Turbulent statistics downstream of the interaction are provided for a range of weakly compressible upstream turbulent Mach numbers $M_t = 0.03 - 0.18$, shock Mach numbers $M_s = 1.2 - 3.0$, and Taylor-based Reynolds numbers $Re_\lambda = 20 - 2500$. The LES displays minimal Reynolds number effects once an inertial range has developed for $Re_\lambda > 100$. The inertial range scales of the turbulence are shown to quickly return to isotropy, and downstream of sufficiently strong shocks this process generates a net transfer of energy from transverse into streamwise velocity fluctuations. The streamwise shock displacements are shown to approximately follow a $k^{-11/3}$ decay with wavenumber as predicted by linear analysis. In conjunction with other statistics this suggests that the instantaneous interaction of the shock with the upstream turbulence proceeds in an approximately linear manner, but nonlinear effects immediately downstream of the shock significantly modify the flow even at the lowest considered turbulent Mach numbers.

LES allows consideration of high Re_λ flows, but remains expensive to compute relative to lower cost modeling approaches such as Reynolds-Averaged Navier Stokes

(RANS). Conventional RANS models are often not well suited for simulations containing discontinuous features such as shocks and, in an effort to improve the performance of RANS, models for averaged shock corrugation effects and the impact of turbulent entropy or acoustic modes on the energy equation are presented. Unlike previous RANS work that has focused on the modification of turbulent statistics by the shock, the proposed models are introduced to capture the effects of the turbulence on the profiles of primitive variables — mean density, velocity, and pressure. By producing accurate profiles for the primitive variables, it is shown that the proposed models improve numerical convergence behavior with mesh refinement about a shock, and introduce the physical effects of shock asphericity in a converging shock geometry. These effects are achieved by local closures to turbulent statistics in the averaged Navier-Stokes equations, and can be applied in conjunction with existing Reynolds stress closures that have been constructed for broader applications beyond shock-turbulence interactions.

PUBLISHED CONTENT AND CONTRIBUTIONS

[1] N.O. Braun and R.A. Gore. On primitive variable behavior near shocks in ensemble-averaged methods. *Journal of Turbulence*, Under peer review.

[2] N.O. Braun, D.I. Pullin, and D.I. Meiron. Regularization method for large eddy simulations of shock-turbulence interactions. *Journal of Computational Physics*, 361:231–246, 2018. doi: https://doi.org/10.1016/j.jcp.2018.01.052.

[3] N.O. Braun, D.I. Pullin, and D.I. Meiron. Inertial-range dynamics downstream of the canonical shock-turbulence *Journal of Fluid Mechanics*, Under peer review.

The author of this thesis wrote these papers and manuscripts, performed the numerical simulations, and analyzed the results of the simulations. The co-authors on these works provided extensive feedback during these studies, assisted in editing the manuscripts, and were instrumental in determining fundamental problem specifications and approaches.

TABLE OF CONTENTS

Acknowledgements . . . iii
Abstract . . . iv
Published Content and Contributions . . . vi
Bibliography . . . vi
Table of Contents . . . vii
List of Illustrations . . . ix
List of Tables . . . xxi
Nomenclature . . . xxii
Chapter I: Introduction . . . 1
1.1 Governing equations . . . 4
1.2 Flow characterization . . . 5
1.3 Dissertation outline . . . 8
Chapter II: LES of the Canonical Shock-Turbulence Problem: Background . . . 9
2.1 Introduction . . . 9
2.2 Flow description . . . 10
2.3 LES Governing Equations . . . 11
2.4 Stretched-Vortex Model (SVM) . . . 12
2.4.1 Turbulent statistics in LES . . . 14
Chapter III: LES of the Canonical Shock-Turbulence Problem: Regularization Method . . . 16
3.1 Introduction . . . 16
3.2 Numerical Method . . . 18
3.3 Dynamic Regularization Technique . . . 18
3.3.1 Background . . . 18
3.3.2 Dynamic Hyperviscosity . . . 19
3.3.3 Hybrid Stretched-Vortex Model (HSVM) . . . 21
3.4 Forced Isotropic Turbulence . . . 21
3.5 Decaying Isotropic Turbulence . . . 24
3.6 Modeled Post Shock Turbulence . . . 25
3.6.1 SGS Model Response to LIA . . . 25
3.6.2 Decay of LIA Turbulence . . . 30
3.7 Shock-Turbulence Interaction . . . 32
3.7.1 Flow Description . . . 32
3.7.2 Numerical Approach . . . 33
3.7.3 Results and Discussion . . . 33
3.8 Discussion . . . 36
Chapter IV: LES of the Canonical Shock-Turbulence Problem: Results . . . 39
4.1 Introduction . . . 39
4.2 Governing equations and subgrid model . . . 39

4.2.1 SGS model near the shock . . . 39
4.3 Numerical method . . . 40
4.4 Turbulence statistics . . . 41
4.5 LES performed . . . 42
4.5.1 Summary of simulations . . . 42
4.5.2 Mesh sensitivity . . . 43
4.5.3 Comparison to DNS . . . 47
4.6 Results and discussion . . . 50
4.6.1 Shock Mach number effects . . . 50
4.6.2 Reynolds number effects . . . 51
4.6.3 Density fluctuations . . . 53
4.6.4 Post shock anisotropy . . . 56
4.7 Discussion . . . 68
Chapter V: Ensemble averaging of a corrugated shock . . . 70
5.1 Introduction . . . 70
5.2 The BHR-3 RANS Model . . . 72
5.3 Ensemble Averaging of a Corrugated Shock . . . 73
5.3.1 Reynolds Stress Transport . . . 76
5.3.2 A Localized Shock Corrugation Model . . . 78
5.3.3 Extension to higher dimensions . . . 80
5.4 Energy Equation Closure . . . 81
5.5 Model Evaluation . . . 83
5.5.1 Canonical Shock-Turbulence Interaction . . . 83
5.5.2 Converging Shockwave . . . 88
5.6 Discussion . . . 94
Chapter VI: Conclusions . . . 96
Appendix A: Linear Interaction Analysis . . . 99
A.1 Introduction . . . 99
A.2 Interaction of a shock with a plane-wave vorticity/entropy disturbance 99
A.3 Integration over a spectrum of upstream turbulence . . . 101
A.4 Application to 3D turbulence . . . 102
Appendix B: Model for turbulent kinetic energy near a shock . . . 104
B.1 Convective SGS kinetic energy model . . . 104
B.2 Amplification of the SGS kinetic energy by the shock . . . 105
Appendix C: Statistics within the region of a corrugated shock . . . 110
Bibliography . . . 114

LIST OF ILLUSTRATIONS

Number *Page*

1.1 Large eddy simulation of the canonical shock-turbulence problem. Flow is from left to right. Isotropic turbulence is introduced at the left boundary and passes through a Mach 1.5 shock with a stationary mean position located at the red line. The contours show turbulent kinetic energy, with lighter colors corresponding to greater turbulence intensity. 2

2.1 Layout of the LES. Isotropic turbulence with the same mean velocity as the flow upstream of the shock is forced at a statistical steady state in a periodic box LES (left). A plane of the flow in the periodic box (red) is copied into the inlet of a transversely periodic channel (right) containing a nearly stationary shock. 10

3.1 Compensated energy spectra from forced periodic isotropic turbulence with the dynamic hyperviscous model and no resolved viscosity. Solid line: 256^3 resolution, $M_t = 0.18$, $\alpha_{max} = 10$. Dashed line: 256^3 resolution, $M_t = 0.06$, $\alpha_{max} = 10$. Circles: 32^3 resolution, $M_t = 0.18$, $\alpha_{max} = 10$. Triangles: 32^3 resolution, $M_t = 0.18$, $\alpha_{max} = 5$. 22

3.2 Energy spectra from forced, periodic, isotropic turbulence. DNS results are for $M_t = 0.18$ and $Re_\lambda = 100$, and the wavenumbers are normalized by the value of η calculated from DNS. The viscosity and the energy injection rate of the forcing are the same for all simulations. The inset shows the behavior of the spectra in the vicinity of the LES cutoff wavenumber. Solid line: DNS. Pluses: hyperviscosity-LES. Circles: SVM-LES. Triangles: HSVM-LES. Dotted line: SVM-LES subgrid spectrum. Dash-dot line: HSVM-LES subgrid spectrum . . . 23

3.3 Fraction of the dissipation that arises from each dissipative term in HSVM-LES of forced, isotropic turbulence at a resolution of 256^3. Each bar represents a different simulation with parameters given in the table on the bottom of the plot. 24

3.4 Turbulent kinetic energy decay. At $t = 0$ the DNS has $M_t = 0.18$ and $Re_\lambda = 100$. Solid line: DNS. Circles: DNS restricted to 64^3 in physical space. Dash-dotted line: resolved scale HSVM-LES. Dashed line: combined resolved and subgrid scale HSVM-LES. . . . 25

3.5 Turbulent kinetic energy decay in flow initialized with $M_t = 0.50$ and $Re_\lambda = 72$. Solid line: DNS of Samtaney et al. [77]. Circles: combined resolved and subgrid scale HSVM-LES. Triangles: combined resolved and subgrid scale SVM-LES. Dotted line: subgrid scale HSVM-LES. Dashed line: subgrid scale SVM-LES. 26

3.6 LIA predicted amplification of the energy spectrum over a $M_s = 1.2$ shock applied to turbulence produced with the stretched-vortex model. The pre-LIA flow field is statistically steady turbulence from a 64^3 SVM-LES with $Re_\lambda \approx 500$ and $M_t \approx 0.18$. The inset shows the behavior of the spectra in the vicinity of the LES cutoff wavenumber. Circles: pre-LIA resolved spectrum. Triangles: post-LIA resolved spectrum. Solid line: pre-LIA averaged SGS spectrum. Dashed line: post-LIA averaged SGS spectrum. 27

3.7 Amplification of the SGS kinetic energy under application of LIA. The LES are on a 64^3 grid with pre-LIA conditions of $Re_\lambda \approx 500$ and $M_t \approx 0.18$. Circles: HSVM-LES. Triangles: SVM-LES. Solid line: LIA kinetic energy amplification above $k = 32$ for isotropic turbulence with a model shell-summed energy spectrum. 29

3.8 Amplification of the SGS components of the streamwise and transverse Reynolds stresses under application of LIA. The LES are on a 64^3 grid with pre-LIA conditions of $Re_\lambda \approx 500$ and $M_t \approx 0.18$. The streamwise direction is defined as the direction parallel to the mean shock normal direction in LIA. Circles: HSVM-LES streamwise Reynolds stress. Triangles: HSVM-LES transverse Reynolds stress. Solid and dashed line: streamwise and transverse Reynolds stress amplification, respectively, above $k = 32$ from LIA applied to a model shell-summed energy spectrum. 29

3.9 Decay of the streamwise and transverse Reynolds stresses in post-LIA periodic, anisotropic turbulence. The flow upstream of the $M_s = 1.5$ shock has $Re_\lambda = 60$ and $M_t = 0.18$. Solid line: DNS. Circles: DNS restricted to 64^3 in physical space. Dashed line: resolved scale HSVM-LES. Dotted line: combined resolved and subgrid scale HSVM-LES. 31

3.10 Reynolds stress anisotropy in post-LIA decaying turbulence. The flow upstream of the modeled $M_s = 1.5$ shock has $Re_\lambda = 60$ and $M_t = 0.18$. Solid Line: DNS. Dotted Line: combined resolved and SGS HSVM-LES. Dashed lined: LIA far field result for shell-summed isotropic spectrum. 31

3.11 Decay of the streamwise Reynolds stress and transverse vorticity in spatial coordinates over a $M_s = 1.2$ shock, with a $Re_\lambda = 20$ upstream. The lines show the DNS of Ryu and Livescu [76] at various upstream turbulent Mach numbers: solid ($M_t = 0.04$), dashed ($M_t = 0.08$), dotted ($M_t = 0.15$). The post-LIA DNS is given by the symbols: pluses ($M_t = 0.04$), triangles ($M_t = 0.08$), circles ($M_t = 0.15$). . . . 32

3.12 Plane-averaged statistics in flow over a $M_s = 1.28$ shock, with upstream $M_t = 0.22$. The figures show streamwise Reynolds stress (a), transverse Reynolds stress (b), dissipation rate (c), and density-specific volume correlation (d). The dissipation rate amplification from LIA is approximated by the predicted amplification in $\langle T \rangle^{0.76} \langle \omega_i \omega_i \rangle / \langle \rho \rangle$. The LES has $Re_\lambda = 300$ upstream of the shock, and the near-shock behavior of DNS with $Re_\lambda = 39$ [45] is plotted for comparison. Solid line: LIA. Dashed line: SVM-LES. Circles: HSVM-LES. Crosses: DNS [45]. 35

3.13 Plane-averaged Reynolds stresses in flow over a $M_s = 1.5$ shock. The LES has upstream conditions of $Re_\lambda = 300$, $M_t = 0.15$, and the DNS [46] has $Re_\lambda = 73$, $M_t = 0.14$. Solid line: DNS [46]. Dashed line: SVM-LES. Circles: HSVM-LES. 36

3.14 Radial spectra of density fluctuations in planes upstream and downstream of a $M_s = 1.5$ shock. The LES has $M_t = 0.15$ and $Re_\lambda = 300$ upstream of the shock. The upstream and downstream results are taken in planes located at $k_0 x = -2$ and $k_0 x = 7$, respectively. Circles: pre-shock SVM-LES. Triangles: post-shock SVM-LES. Dashed line: pre-shock HSVM-LES. Dotted line: post-shock HSVM-LES. 36

4.1 Evolution of the streamwise Reynolds stress downstream of a $M_s = 1.2$ shock, for upstream conditions of $M_t = 0.02$ and $Re_\lambda = 20$. Solid line: LIA. Dashed line: shock-captured DNS. Dotted line: shock-resolved DNS of Ryu and Livescu [76]. 42

4.2 LES behavior for $M_s = 1.5$, $M_t = 0.06$, $Re_\lambda = 500$ on a $96 \times 64 \times 64$ base mesh with increasing local mesh refinement at the shock. Lines with symbols show the total statistics, including the contribution from the SGS model. (a) Streamwise Reynolds stress, (b) transverse Reynolds stress, (c) density-specific volume correlation $b = -\langle \rho' v' \rangle$, and ($d$) squared vorticity trace, $\Omega_{ii} = \omega_i \omega_i$. Dashed line (△): uniform grid. Dot-dashed line (○): 2× refinement. Dotted line (□): 4× refinement. Solid line (+): 8× refinement. Thick solid line: LIA of (3.10). 45

4.3 Time-averaged radial spectrum of shock displacement, for $M_s = 1.5$, $Re_\lambda \approx 500$, and $M_t \approx 0.06$ on a $96 \times 64 \times 64$ base mesh. The symbols show the results from LES with varying levels of AMR at the shock. (△): uniform grid. (○): 2× refinement. (□): 4× refinement. (+): 8× refinement. Dashed line: LIA of (3.10), which follows a $k^{-11/3}$ slope in the inertial range. 47

4.4 Streamwise (a) and transverse (b) Reynolds stresses averaged over time and cross sectional planes for a $M_s = 2.0$ shock and upstream $Re_\lambda \approx 500$ on a $512 \times 128 \times 128$ base mesh. Solid line: LIA. Dotted line: $M_t = 0.12$ and ×4 AMR. Dashed line: $M_t = 0.06$ and ×4 AMR. Dot-dashed line: $M_t = 0.03$ and ×4 AMR. Pluses: $M_t = 0.03$ and ×8 AMR. 48

4.5 Streamwise (a) and transverse (b) Reynolds stresses averaged over time and cross sectional planes for a $M_s = 1.5$ shock. Inlet conditions are $M_t = 0.16$, $Re_\lambda = 75$, and $k_0 = 6$. The lines show the resolved scale statistics and the symbols show the total statistics, including the contribution from the SGS model. The LES have a factor of 4× AMR at the shock, and are normalized by their total upstream value interpolated to the mean shock position. Dotted line (□): LES with a $192 \times 128 \times 128$ base grid. Dash-dotted line (○): LES with a $96 \times 64 \times 64$ base grid. Thick solid line: shock-captured DNS of Larsson et al. [46] [data from 35]. 49

4.6 Streamwise (a) and transverse (b) Reynolds stresses averaged over time and cross sectional planes for a $M_s = 1.5$ shock, with upstream conditions of $M_t = 0.06$ and $Re_\lambda = 500$. LES are conducted with a factor of 4× AMR at the shock, and results include the contribution from the SGS model. Solid line: LES with $1024 \times 256 \times 256$ coarse mesh. Circles: LES with $512 \times 128 \times 128$ coarse mesh. Dashed line: LIA of (3.10). 49

4.7 Streamwise and transverse Reynolds stress amplifications over a shock. LES has upstream flow conditions of $M_t \approx 0.06$ and $Re_\lambda \approx 500$, and is on a $512 \times 128 \times 128$ coarse mesh with 4× AMR. The DNS was performed by Ryu and Livescu [76] at $Re_\lambda = 20$ with M_t ranging between $0.05 - 0.12$ immediately upstream of the shock. Post shock values are taken at the position of the maximum post-shock streamwise Reynolds stress and include contributions from the SGS model. Streamwise Reynolds stress amplifications are given by the squares (LES), triangles (DNS), and solid line (LIA). Transverse Reynolds stress amplifications are the circles (LES), pluses (DNS), and dashed line (LIA). 51

4.8 Squared vorticity trace $\Omega_{ii} = \omega_i \omega_i$ and kinetic energy dissipation rate immediately downstream of the shock, normalized by their upstream value. The LES conditions are the same as in figure 4.7. The LIA amplification in dissipation rate is approximated by the amplification in $\langle \mu \rangle \langle \Omega_{ii} \rangle / \langle \rho \rangle$. Vorticity amplifications $\langle \Omega_{ii} \rangle / \langle \Omega_{ii} \rangle_0$ are the circles (LES) and dashed line (LIA). Dissipation rate amplifications are given by the triangles (LES) and solid line (LIA). 52

4.9 Amplification in the streamwise Reynolds stress over a $M_s = 1.5$ shock, and the fraction of that Reynolds stress held in the subgrid scales downstream of the shock. Downstream quantities are sampled at the position of the peak streamwise Reynolds stress. The dashed line has an upstream $M_t \approx 0.06$ and the dotted line has $M_t \approx 0.18$. The squares are LES done on a $512 \times 128 \times 128$ coarse mesh and the circles are done on a $1024 \times 256 \times 256$ coarse mesh. Both meshes use 4× AMR. 53

4.10 Radial power spectra of density fluctuations (a) and co-spectra of density-velocity fluctuations (b) for a $M_s = 1.5$ shock, with upstream conditions of $M_t \approx 0.18$ and $Re_\lambda \approx 500$ on a $1024 \times 256 \times 256$ base grid with 4× AMR. In (b), the lines show the co-spectrum of $\overline{\rho}\tilde{u}_1$, and the symbols show the co-spectrum of $\overline{\rho}\tilde{u}_2$. Solid line (∘): $k_0 x = -1.34$. Dotted line (+): $k_0 x = 5.57$. Dashed line (△): $k_0 x = 28.3$. 54

4.11 Averaged density-specific volume correlation $b = -\langle \rho' v' \rangle$ in LES with upstream $M_t \approx 0.06$ and $Re_\lambda \approx 500$ on a $512 \times 128 \times 128$ base grid with 4× AMR. Solid line: $M_s = 1.2$. Dashed line: $M_s = 1.5$. Dotted line: $M_s = 2$. Dash-dotted line: $M_s = 2.2$. Long-dashed line: $M_s = 2.6$. The circle and triangle symbols show LIA of (3.10) at $M_s = 1.5$ and $M_s = 2.6$, respectively 55

4.12 Averaged mass-weighted velocity fluctuations $a_i = \langle \rho' u_i' \rangle / \langle \overline{\rho} \rangle$. The LES is shown by the symbols and has upstream $Re_\lambda \approx 500$ on a $1024 \times 256 \times 256$ base grid with 4× AMR. Solid line: $M_s = 1.5$ LIA of (3.10). Circles : $M_s = 1.5$, $M_t = 0.06$. Pluses: $M_s = 1.5$, $M_t = 0.18$. Triangles: $M_s = 2.2$, $M_t = 0.18$. 55

4.13 Evolution of post-shock Reynolds stress anisotropy in the plane of the b_{ij} tensor invariants ξ_l and η_l. The upstream flow has $M_t = 0.06$ and $Re_\lambda \approx 500$, and are performed in LES on a $512 \times 128 \times 128$ mesh with 4× AMR. The symbols show the LES results, and are colored by their streamwise position downstream of the shock. The lines show the boundaries of the Lumley triangle, corresponding to the domain of realizable flow conditions. 57

4.14 Evolution of post-shock Reynolds stress anisotropy in the plane of the b_{ij} tensor invariants ξ_l and η_l. The upstream flow has $M_t = 0.18$ and $Re_\lambda \approx 500$, and are performed in LES on a $1024 \times 256 \times 256$ mesh with 4× AMR. The symbols show the LES results, and are colored by their streamwise position downstream of the shock. The lines show the boundaries of the Lumley triangle, corresponding to the domain of realizable flow conditions. 58

4.15 Time averaged radial velocity spectra about a $M_s = 2.2$ shock, for upstream conditions of $M_t \approx 0.18$ and $Re_\lambda \approx 500$ on a $1024 \times 256 \times 256$ base grid with 4× AMR. The symbols show the resolved spectra in planes located at $k_0 x = -1.47(\circ)$, $k_0 x = 5.52(+)$, $k_0 x = 28.1(\triangle)$. The averaged spectra of the modeled subgrid flows at each plane are given by the solid, dotted, and dashed lines, respectively, and these are extended into the resolved scales to show agreement with the resolved spectra. 59

4.16 Time averaged anisotropy parameter in isotropic upstream turbulence upstream of a $M_s = 1.5$ shock, with $M_t \approx 0.18$ and $Re_\lambda \approx 500$ on a $1024 \times 256 \times 256$ base grid. The solid line shows χ^{2D} calculated under the assumption of isotropy using the model spectrum (3.10), and the dashed line is the result for an infinite $k^{-5/3}$ spectrum. The circles are the LES, given at a plane located at $k_0 x = -2$, just upstream of the mean shock position shock. 60

4.17 Time averaged anisotropy parameter downstream of a shock, for upstream conditions of $M_t \approx 0.18$ and $Re_\lambda \approx 500$ on a $1024 \times 256 \times 256$ base grid with 4× AMR. The solid line shows χ^{2D} calculated from the results of LIA applied to the model spectrum (3.10), and the dashed line is the preshock result for (3.10). The dotted line is the result for an infinite $k^{-5/3}$ spectrum. The LES results are given by the symbols, and are calculated in cross-sectional planes downstream of the shock at streamwise locations given in the subcaptions. 61

4.18 Time averaged radial power spectra of the streamwise and transverse velocities downstream of a $M_s = 2.2$ shock, for upstream conditions of $M_t \approx 0.18$ and $Re_\lambda \approx 500$ on a $1024 \times 256 \times 256$ base grid with 4× AMR. The symbols show the LES, and the lines show LIA applied to the model spectrum (3.10). Solid line ($\circ$): $k_0 x = -1.5$ upstream spectra. Dotted line ($\triangle$): $k_0 x = 0.7$. Dashed line ($\square$): $k_0 x = 2.3$. . . 62

4.19 Three dimensional spectra of streamwise and transverse velocity fluctuations in LIA-processed LES, in which a periodic, anisotropic 256^3 LES is initialized by applying LIA to an isotropic LES with $Re_\lambda \approx 500$ and $M_t \approx 0.18$. The LIA models a $M_s = 2.2$ shock. An equivalent downstream position $k_0 x$ is produced by scaling the simulation time by the mean convection velocity downstream of a stationary shock. Dotted line: $E_{11}(k)$ pre-LIA. Dot-dashed line: $E_{22}(k)$ pre-LIA. Solid line: $E_{11}(k)$ at $k_0 x = 0$. Dashed line: $E_{22}(k)$ at $k_0 x = 0$. Circles: $E_{11}(k)$ at $k_0 x = 6.0$. Triangles: $E_{22}(k)$ at $k_0 x = 6.0$. 65

4.20 Three dimensional spectra of streamwise and transverse velocity fluctuations in LIA-processed LES. Pre-LIA flow conditions are the same as in Figure 4.19. Dotted line: $E_{11}(k)$ pre-LIA. Dot-dashed line: $E_{22}(k)$ pre-LIA. Solid line: $E_{11}(k)$ at $k_0 x = 0$. Dashed line: $E_{22}(k)$ at $k_0 x = 0$. Circles: $E_{11}(k)$ at $k_0 x = 6.0$. Triangles: $E_{22}(k)$ at $k_0 x = 6.0$. 65

4.21 Reynolds stress anisotropy. The symbols show the anisotropy from shock-processed LES with $M_s = 2.2$, upstream $M_t \approx 0.18$ and $Re_\lambda \approx 500$ on a $1024 \times 256 \times 256$ base grid with $4\times$ AMR. The line shows LIA-processed LES, in which LES in a periodic 256^3 box is initialized by applying LIA to an LES of homogeneous isotropic turbulence with the same upstream conditions. The temporal decay in the LIA-processed LES is converted to a spatial coordinate using the mean convection velocity downstream of the shock. 66

4.22 Anisotropy parameter calculated from 2D radial spectra in planes parallel to the shock. The pre-shock flow has $Re_\lambda = 500$ and $M_t = 0.18$. The lines show shock-processed LES, in which the shock is explicitly simulated, and the symbols show LIA-processed LES. The temporal decay in the LIA-processed LES is converted to a spatial coordinate using the mean convection velocity downstream of the shock. Solid lines and circles: $k_0 x \approx 2.3$. Dashed line and triangles : $k_0 x \approx 7.7$. Dotted line: $\chi^{2D} = 1/33$ analytical result for an infinite isotropic $k^{-5/3}$ spectrum. 67

4.23 Reynolds stress anisotropy. The symbols show the anisotropy at the location of the peak downstream value of R_{11} in LES with upstream $M_t \approx 0.06$ and $Re_\lambda \approx 500$ on a $512 \times 128 \times 128$ base grid with $4\times$ AMR. The solid line is the far field result of LIA. The dashed line is produced by applying LIA to the model spectrum (3.10) and post-processing the results to enforce that all wavenumbers $k/k_0 > 2$ have returned to isotropy downstream of the shock. 68

5.1 Reynolds stress distribution within the region of interface corrugation. The solid line corresponds to $\overline{u_1' u_1'}$ at all M_s and $\widetilde{R}_{11}$ at $M_s = 1$. Dashed line : $\widetilde{R}_{11}$ at $M_s = 1.5$. Dotted line : $\widetilde{R}_{11}$ at $M_s = 5$. 75

5.2 Reynolds stress source terms integrated from upstream to the peak-$\widetilde{R}_{11}$ location. Solid line : $2\int_{-\infty}^{x_0} a_1 \frac{\partial \overline{P}}{\partial x_1} dx$. Dashed line : $-2\int_{-\infty}^{x_0} \overline{\rho}\tilde{R}_{11}\frac{\partial \tilde{u}_1}{\partial x_1} dx$. Dotted line : $-\Delta_{x_0}\left(\overline{u_1'' P'}\right)$. All results are normalized with respect to $\overline{\rho}_u \tilde{u}_u \Delta\overline{u}_1^2/4$. 77

5.3 Fit of 1-D cutoff function ϕ_{1D} to LIA integral. Solid line : $\left(1 - \frac{\overline{u}_{1,d}}{\overline{u}_{1,u}}\right)\int_{\psi=0}^{\pi/2} \frac{\sqrt{\tilde{L}\tilde{L}^*}}{m} \sin\psi \, d\psi$ calculated from LIA. Dotted line : $1 - \exp\left(-\frac{1}{2\overline{c}_u}\sqrt{\frac{\Delta\overline{u}_1^2}{4}}\right)$. 80

5.4 Absolute error in the streamwise Reynolds stress amplification in 1-D shock turbulence simulations, with $M_s = 5$. Error is calculated relative to the finest mesh resolution simulation available for the same code and model, which has $\theta_{max} = 21$ in the AMROC simulations and $\theta_{max} = 126$ in the xRAGE simulations, where $\theta = (S_{T_u} K_u^{1/2})/(\Delta x V_s)$. The mesh resolution becomes finer moving from left to right. Circles : mBHR-3 with shock-corrugation and entropic mode transport models. Triangles : standard BHR-3 model. Pluses : standard BHR-3 model, implemented in the xRAGE hydrocode [80]. 85

5.5 Maximum streamwise Reynolds stress attained at the center of a shock, normalized by the upstream sound speed. Circles: mBHR-3 model. Line: $\Delta\overline{u}_1^2/4$ as calculated from the laminar Euler equations. . 86

5.6 Shock thickness from the mBHR-3 model compared to the LIA of Mahesh [63] and $Re_\lambda = 40$ DNS of Larsson et al. [46]. The DNS and RANS have an upstream $M_t = 0.22$. The shock thickness in the DNS and RANS is defined as the region where the divergence of the mean velocity is at least five percent of its maximum value. The DNS is normalized by M_t/k_0, and the mBHR-3 result is normalized by $S_T M_t/\pi$. The LIA result shows the RMS shock perturbation amplitude, normalized by $M_t/(3k_0)$. The factor of 3 applied to the LIA results is included to show the consistent scaling behavior of the methods. Solid line: LIA [63]. Pluses: DNS [46]. Circles: mBHR-3. 87

5.7 Reynolds stress amplifications through a shock. Triangles and circles: mBHR-3 streamwise Reynolds stress at $M_t = 0.1$ and $M_t = 0.22$, respectively. Diamonds and crosses: mBHR-3 transverse Reynolds stress at $M_t = 0.1$ and $M_t = 0.22$. The pluses and squares show the streamwise and transverse Reynolds stresses with $M_t = 0.1$, and $R_{11,shock}$ set to twice its normal value. Solid line: LIA streamwise Reynolds stress. Dashed line: LIA transverse Reynolds stress. 88

5.8 Mean density and pressure profiles in shock-turbulence interactions, with an upstream $M_t = 0.22$. The DNS was performed by Larsson and Lele [45] and has an upstream $Re_\lambda = 40$. The mBHR model uses the normalization $k_0 \approx \pi/S_T$ in the streamwise coordinate. Results are shown for shock Mach numbers of $M_s = 1.28$, $M_s = 1.5$, and $M_s = 1.87$, in order of increasing density and pressure amplification. Solid black lines: laminar Euler equations. Solid blue lines: DNS[45]. Dashed lines: mBHR-3 model. 89

5.9 Density profiles in shock-turbulence interactions, for a $M_s = 1.5$ shock. The DNS was performed by Larsson et al. [46] and has an upstream $Re_\lambda \approx 75$. Solid line: DNS, $M_t = 0.22$. Circles: mBHR-3 model, $M_t = 0.22$. Dash-dotted line: DNS, $M_t = 0.38$. Pluses: mBHR-3 model, $M_t = 0.38$. 90

5.10 Density profiles in shock-turbulence interactions, for a $M_s = 1.5$ shock. The DNS was performed by Larsson et al. [46] and has an upstream $Re_\lambda \approx 75$. The colours indicate the upstream turbulent Mach number. Blue: $M_t = 0.22$. Red: $M_t = 0.38$. The solid black line is the laminar shock jump condition. Solid line: DNS. Dashed line: mBHR-3 model. Dotted line: BHR-3 with the shock corrugation model but not the entropy mode closure. 91

5.11 Density profiles in shock-turbulence interactions with $M_t = 0.22$. The DNS was performed by Larsson and Lele [45] and has an upstream $Re_\lambda \approx 40$. Results are shown for shock Mach numbers of $M_s = 1.28$ and $M_s = 1.5$, in order of increasing density amplification. The solid black lines are the laminar shock jump condition. Solid line: DNS. Dotted line: mBHR-3 model. Dashed line: mBHR-3 model, using the acoustic closure (5.23) instead of the entropy closure (5.24). 92

5.12 Density profiles in converging shock-turbulence interaction. The shock has an initial $M_{s0} = 1.4$ and the turbulence is initialized with a uniform M_{t0}. Density profiles are shown at times $t/t_s = 0.3$ (blue), $t/t_s = 0.6$ (black), and $t/t_s = 0.9$ (red). Solid lines: numerical Euler equations. Dashed lines: mBHR-3, $M_{t0} = 0.4$. Dotted lines: mBHR-3, $M_{t0} = 0.8$. 93

A.1 Domain of Vorticial/Entropic Wave - Shock Interaction 100

B.1 Two-shock Riemann problem at a cell boundary between cells located at x_i and x_{i+1}. Regions (1) and (4) correspond to unshocked fluid. (2) is fluid initially from cell x_i that has been shocked by the left facing wave, and (3) is from cell x_{i+1} shocked by the right facing wave. . . . 106

B.2 Amplification in the SGS kinetic energy through a shock. LES results are averaged in time and in the periodic directions. The LES flow conditions are $M_s = 1.5$, $M_t = 0.18$, and $Re_\lambda = 500$ on a $1024 \times 256 \times 256$ base grid, with a factor of 4 refinement at the shock. The LIA results are calculated from (2.10) with $k_{c,LIA} = 1024$. Solid line: LIA kinetic energy amplification. Dashed line: LIA kinetic energy amplification at wavenumbers $k > 128$. Dotted line: convective SGS kinetic energy model $\tilde{k}'_{cm}$. Dash-dotted line: SGS kinetic energy $\tilde{k}'$ calculated from (2.10). 109

C.1 Fluctuations in the velocity field as given by (C.9), which result from the motion of the shock. The fluctuations are normalized by $\Delta\overline{u}_1$. . . 111

LIST OF TABLES

Number *Page*

4.1 Summary of simulations. The conditions of the upstream turbulence, M_t and Re_λ, contain contributions from the model of the subgrid flows and are thus approximations. L_x is the length of the domain in the streamwise direction, x_s is the shock position, and k_0 is the wavenumber corresponding to the maximum in the energy spectrum of the upstream turbulence. N_x and N_y are the resolution of the coarsest mesh level in the streamwise and transverse directions, respectively. AMR gives the factor of refinement applied to the mesh near the shock. 44

5.1 Maximum amplifications in density and pressure achieved in converging shock simulations. The simulations are initialized with a shock of strength $M_{s0} = 1.4$. The DNS was conducted by Bhagatwala and Lele [8]. 94

NOMENCLATURE

Accents/Brackets

$\check{f}$ f normalized by A_v, $\check{f} = f/A_v$.

$\ddot{f}'$ Part of f' associated with the entropy and/or vorticity field.

$\dot{f}'$ Part of f' associated with the acoustic field.

$\hat{f}$ Fourier transform of f.

$\langle \rho f \rangle / \langle \rho \rangle$ Favre Average.

$\langle f \rangle$ Average value of f.

$\overline{f}$ Resolved part of f. In LES (Chapters 2-3) this is a filtered f, and in RANS (Chapter 4) it is an averaged f.

$\tilde{f}$ Resolved part of f, under Favre averaging or filtering. In LES (Chapters 2-3) this is a Favre-filtered f, and in RANS (Chapter 4) it is a Favre-averaged f.

f' Fluctuation in f, $f' = f - \langle f \rangle$.

f'' Fluctuation in f relative to the Favre average, $f'' = f - \langle \rho f \rangle / \langle \rho \rangle$.

f^* Complex conjugate of f.

Constants/Scalars

χ Anisotropy parameter.

Δx Grid spacing at the coarsest level of AMR.

η Kolmogorov microscale.

η_l Invariant of b_{ij} tensor, $6\eta_l^2 = b_{ij}b_{ji}$.

Γ Incomplete Gamma function.

γ Ratio of specific heats.

λ Streamwise Taylor lengthscale.

λ_m Mean-free-path.

$\mathcal{F}_2$ Second order velocity structure function.

$\mathcal{K}_0$ Kolmogorov prefactor.

μ Dynamic viscosity.

ν Kinematic viscosity.

ψ Incidence angle between the mean shock normal and an upstream plane wave.

ρ Density.

τ Large eddy turnover time.

τ_{ij} Subgrid stress tensor.

$\tilde{k'}$ Subgrid turbulent kinetic energy.

ε Dissipation rate of turbulent kinetic energy.

ξ Shock surface.

ξ_l Anisotropy parameter.

ξ_l Invariant of b_{ij} tensor, $6\xi_l^3 = b_{ij}b_{jk}b_{ki}$.

A_v Nondimensional vorticity wave amplitude.

b Density-specific volume correlation, $-\langle\rho'v'\rangle$.

c Speed of sound.

c_p Specific heat at constant pressure.

c_v Specific heat at constant volume.

E Total energy.

$E(k)$ Shell-summed energy spectrum.

K Turbulent kinetic energy.

k Wavenumber magnitude, $k^2 = k_x^2 + k_y^2 + k_z^2$.

k_0 Peak or most energetic wavenumber in a reference energy spectrum.

k_c Cutoff wavenumber of the computational mesh, $k_c = \pi/Deltax$.

l Sine of incidence angle between the mean shock normal and an upstream plane wave.

L_I Integral lengthscale.

m Cosine of incidence angle between the mean shock normal and an upstream plane wave.

M_t Turbulent Mach number, $\sqrt{\langle R_{ii}\rangle}/\langle c\rangle$.

p Pressure.

R Specific gas constant.

Re_λ Taylor Reynolds number.

S_D Dissipation lengthscale.

S_T Lagrangian transport lengthscale from BHR-3 RANS model.

v Specific volume.

V_s Mean shock velocity relative to the upstream flow.

Vectors/Tensors

δ_{ij} Kronecker delta function.

Ω_{ij} Squared vorticity tensor, $\Omega_{ij} = \omega_i \omega_j$.

ω_i Vorticity.

σ_{ij} Stress tensor.

τ_{ij} Subgrid stress tensor.

a_i Turbulent mass flux, $\langle \rho' u' \rangle / \langle \rho \rangle$.

b_{ij} Reynolds stress anisotropy tensor.

q_i^T Subgrid heat flux.

R_{ij} Reynolds stress.

S_{ij} Rate of strain tensor.

u_i Velocity.

Chapter 1

INTRODUCTION

The interaction of a shockwave with a turbulent upstream flow results in a rapid compression and amplification of the turbulence along with distortion of the shock front. The behavior of this phenomenon is of importance to a wide range of problems involving compressible turbulence, particularly those concerned with shock driven mixing in areas such as inertial confinement fusion or supersonic combustion engines. Practical engineering applications leading to these flows display a wide range of complex physics, but the fundamental hydrodynamics of the interaction are accessible in the comparably simple canonical problem of a normal shock with a stationary mean position interacting with homogeneous isotropic upstream turbulence in a single component gas.

The canonical shock-turbulence problem is illustrated in Figure 1.1. An advantage of addressing this flow over more complex problems is that the simple geometry involved makes it well suited for application of computationally inexpensive analytical models. Under the assumption that the timescales associated with the turbulence are slow relative to those of the shock compression, Lele [51] applied Rapid Distortion Theory (RDT) to investigate the modified mean flow Rankine-Hugoniot jump conditions and shock velocity of a shock in turbulent flow. Zank et al. [91] performed a similar analysis, but incorporated non-linear effects in the interaction. RDT has also been applied to investigate the turbulent kinetic energy amplification over a shock, but for this use RDT shows limited agreement with other methods [39].

Linear Interaction Theory (LIA) is conceptually similar to RDT but builds in a wider range of physics, including perturbations to the shock front and the downstream evolution of pressure modes. In LIA, the upstream turbulence is decomposed into its component planar modes [44], and a solution to the linearized Euler equations for an incident wave passing through a shock is determined for each wave type — vorticity [71], acoustic [66], and entropy [12, 64]. Integrating the downstream solutions over the energy spectrum of the upstream turbulence provides the amplifications and near-shock fluctuations of turbulent statistics such as the Reynolds stresses and vorticity [72]. Ryu and Livescu [76] showed that the LIA-predicted amplifications agree with DNS at low turbulent Mach numbers, and proposed that the assumptions

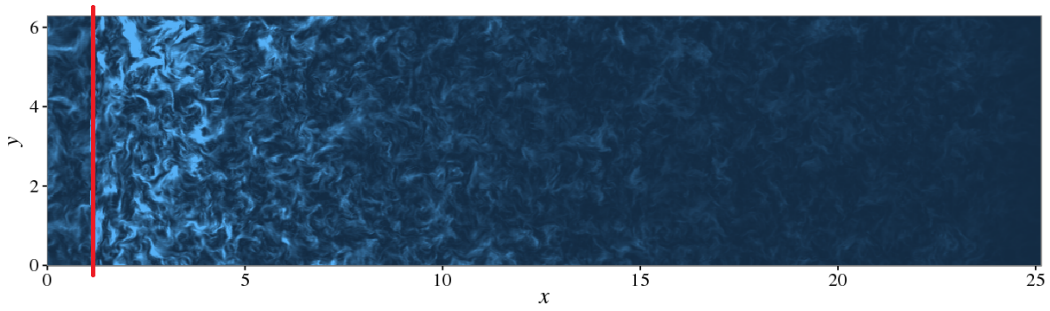

Figure 1.1: Large eddy simulation of the canonical shock-turbulence problem. Flow is from left to right. Isotropic turbulence is introduced at the left boundary and passes through a Mach 1.5 shock with a stationary mean position located at the red line. The contours show turbulent kinetic energy, with lighter colors corresponding to greater turbulence intensity.

underlying LIA are valid if the shock thickness is small relative to the viscous scales of the upstream turbulence. Wouchuk et al. [90] derived exact analytical expressions for the linearized amplifications of key turbulent statistics, and applied the analysis to the passage of a shock from quiescent fluid into a turbulent half-space. A more detailed description of LIA, as used in this study, is provided in Appendix A.

A number of Direct Numerical Simulations (DNS) have considered the canonical shock-turbulence problem. Early works investigated the impact of numerical shock-capturing schemes and varying turbulent and shock Mach numbers [48, 49], but were limited to low Reynolds numbers. Mahesh et al. [64] investigated the effects of an upstream turbulent flow containing entropy fluctuations and anisotropy arising from correlations in the entropy and vorticity fields, and this was further expanded on by Jamme et al. [40]. More recent simulations [45, 46, 76] have considered a wider range of Reynolds numbers, $Re_\lambda \approx 10-75$, but even these moderate Reynolds number flows require meshes as fine as 2366×1024^2 [46]. Inertial range turbulence ($Re_\lambda > 100$) remains difficult to address in DNS because the computational cost of simulations that resolve the wide range of lengthscales in turbulence scales as Re_λ^6 [69]. The cost to implement shock-capturing methods in an accurate manner is also expected to increase in simulations of higher Re_λ flows because the numerical shock should remain smaller than the smallest turbulent scales of the flow [85].

Experiments allow for substantially larger Reynolds numbers, $Re_\lambda \approx 100-1000$ [2], but face other difficulties. Barre et al. [4] investigated the turbulent flow downstream of a grid of nozzles as it passed through a stationary normal shock held in place

by a pair of wedges. This yielded an accelerating mean velocity field downstream of the shock, but the longitudinal velocity fluctuations still showed agreement with LIA in the far field downstream of the shock. Agui et al. [2] considered the subject problem in a shock tube by passing a shock through a grid. The shock reflects off of a semi-porous wall at the end of the tube and travels back into the turbulence produced downstream of the grid. Tailoring the grid, shock strength, and end wall porosity allowed Agui et al. [2] to consider a range of flow parameters, but the resulting amplifications in the turbulent Reynolds stresses had limited agreement with LIA, particularly at larger shock Mach numbers. Kitamura et al. [42] studied a weak spherical expanding blast wave in incompressible turbulence, and showed Re_λ had a limited effect on the interaction for $Re_\lambda > 100$. The Reynolds number and turbulent intensity in front of the shock were coupled in this study, but the turbulent Mach number, $M_t < 0.003$, was small for all test cases.

Large Eddy Simulation (LES) resolves the dynamics of the large scale motions that contain most of the kinetic energy, but employs a Subgrid-Scale (SGS) model to approximate the action of small scale eddies that drive viscous dissipation and mixing. This approach greatly reduces the computational cost of a simulation relative to DNS, and allows for high Reynolds number conditions to be addressed even on very coarse meshes. As the shock Mach number is increased the cost to resolve the shockwave thickness becomes prohibitive, and so in practice these advantages in the computational cost of LES become achievable only if the shock is captured numerically. Early work addressing the canonical shock-turbulence problem with LES found that shock capturing schemes produce excessive dissipation in the turbulence, suggesting that these schemes should be applied only in the direct vicinity of the shock and only in the direction of the shock normal [47]. Ducros et al. [22] introduced a shock sensor that allows localized shock capturing to be applied to problems where a priori knowledge of the shock location and orientation is not available. Comparisons of explicit [6, 26] and implicit [35] LES approaches have further explored the relative effectiveness of different SGS models downstream of a shock.

LES reduces computational cost relative to DNS, but remains expensive and is often difficult to implement. Reynolds-Averaged Navier-Stokes (RANS) methods thus remain in widespread use, particularly in practical engineering applications. These models average the governing equations, relaxing resolution requirements and often reducing the dimensionality of problems, but introduce unclosed correlations

that must be modeled, typically by empirical calibration to experiments or high fidelity simulations. Recent efforts have been made to develop RANS models for compressible and variable density flows [7, 32, 80], applicable to fundamental flows such as Richtmyer-Meshkov instabilities in which a shock perturbs a material interface, which then develops into a turbulent layer upon reshock.

The work contained in this thesis aims to improve the ability of LES and RANS to address the canonical shock-turbulence problem, and leverage LES to investigate the behavior of this flow within regimes that preclude the use of DNS. Previous LES studies of the canonical shock-turbulence problem have generally focused on methodology and ability to reproduce DNS [e.g. 6], whereas the LES in this study aims to resolve a larger range of flow scales in order investigate the physical behavior of the interaction within high Re_λ regimes.

1.1 Governing equations

The subject canonical shock-turbulence problem satisfies the equations of motion for a single species fluid,

$$\frac{\partial \rho}{\partial t} + \frac{\partial \rho u_j}{\partial x_j} = 0, \tag{1.1a}$$

$$\frac{\partial \rho u_i}{\partial t} + \frac{\partial \rho u_i u_j + p\delta_{ij}}{\partial x_j} = \frac{\partial \sigma_{ij}}{\partial x_j}, \tag{1.1b}$$

$$\frac{\partial E}{\partial t} + \frac{\partial (E+p) u_j}{\partial x_j} = \frac{\partial}{\partial x_j}\left(\kappa \frac{\partial T}{\partial x_j}\right) + \frac{\partial \sigma_{ij} u_i}{\partial x_j}, \tag{1.1c}$$

where ρ is the density, u_i is the velocity, p is the pressure, and E is the total energy. Repetition of indices implies summation and δ_{ij} is the Kronecker delta function. The fluid is taken to be a calorically perfect gas with a ratio of specific heats $\gamma = c_p/c_v = 1.4$ and sound speed $c = \sqrt{\gamma p/\rho}$. The viscous stress is Newtonian,

$$\sigma_{ij} = \mu\left(\frac{\partial u_i}{\partial x_j} + \frac{\partial u_j}{\partial x_i} - \frac{2}{3}\frac{\partial u_k}{\partial x_k}\delta_{ij}\right), \tag{1.2}$$

with temperature dependent dynamic viscosity $\mu = \mu_0 (T/T_0)^{0.76}$. The heat conductivity $\kappa = \mu c_p / P_r$ follows the same relation as the viscosity, with Prandtl number $P_r = 0.7$. The total energy is

$$E = \frac{p}{\gamma - 1} + \frac{1}{2}\rho u_i u_i. \tag{1.3}$$

Solving system (1.1) directly is referred to as DNS, but DNS is impractical in many scenarios where the separation between the energetic and viscous scales of the

turbulence is large. The subsequent LES and RANS approaches solve simplified systems representing the dynamics of (1.1), without directly resolving all motions of the flow.

1.2 Flow characterization

The turbulent flow upstream of the shock is isotropic and homogeneous, with statistics that are the same in all directions and uniform in space. The turbulence is decomposed as $f = \langle f \rangle + f'$, where $\langle f \rangle$ is the average of f over the homogeneous directions in the flow and f' is the remaining fluctuation about that mean. In variable density flow, it is also convenient to define Favre-averaged fluctuations,

$$f'' = f - \frac{\langle \rho f \rangle}{\langle \rho \rangle} = f' - \frac{\langle \rho' f' \rangle}{\langle \rho \rangle}. \tag{1.4}$$

The strength of turbulent velocity fluctuations in the flow are described by the Reynolds stress tensor,

$$R_{ij} = \frac{\langle \rho u_i'' u_j'' \rangle}{\langle \rho \rangle}, \tag{1.5}$$

and density fluctuations are measured by the density-specific volume correlation $b = -\langle \rho' v' \rangle$ where $v = 1/\rho$ is the specific volume. The density-specific volume correlation b is favored over $\langle \rho' \rho' \rangle$ because of its applications in incompressible mixing of variable density fluids [54, 79], but for small density fluctuations, $b \approx \langle \rho' \rho' \rangle / \langle \rho \rangle^2$. The velocity-density correlation $a_i = \langle \rho' u' \rangle / \langle \rho \rangle$, which represents the turbulent mass flux, is also of interest and is an important variable tracked in some RANS models [80].

The shock Mach number is $M_s = V_s/c$, where V_s is the mean shock velocity relative to the upstream flow. The non-dimensional parameters characterizing isotropic turbulent flow are a turbulent Mach number M_t and Taylor Reynolds number Re_λ. These are defined as functions of the root-mean-square velocity, u_{rms}, and streamwise Taylor microscale, λ_1, by

$$M_t = \frac{\sqrt{\langle R_{ii} \rangle}}{\langle c \rangle}, \tag{1.6a}$$

$$u_{rms} = \sqrt{\frac{\langle R_{ii} \rangle}{3}}, \tag{1.6b}$$

$$Re_\lambda = \frac{\langle \rho \rangle \lambda_1 u_{rms}}{\langle \mu \rangle}, \tag{1.6c}$$

$$\lambda_1 = \sqrt{\frac{u_{rms}^2}{\langle (\partial u_1 / \partial x_1)^2 \rangle}}. \tag{1.6d}$$

The flow downstream of the shock is anisotropic, but (1.6) is sufficient for describing the isotropic flow upstream of the shock. The large eddy turnover time of isotropic turbulence is $\tau = L_I / u_{rms}$, with integral length scale L_I,

$$L_I = \frac{3\pi}{4} \frac{\int_0^\infty E(k)/k dk}{\int_0^\infty E(k) dk}. \tag{1.7}$$

The shell-summed energy spectrum $E(k)$, as a function of wavenumber magnitude k, is defined as the integral of $(1/2)\hat{u}_i \hat{u}_i^*$ over a surface of a sphere of radius k, where $\hat{f}$ denotes the Fourier transform of f and f^* denotes the complex conjugate. The dissipation rate, ε, and Kolmogorov microscale, η, are

$$\varepsilon = \frac{\partial \langle u_i u_i / 2 \rangle}{\partial t}, \tag{1.8}$$

$$\eta = \left(\frac{\langle \nu \rangle^3}{\varepsilon} \right)^{1/4}, \tag{1.9}$$

where $\nu = \mu / \rho$ is the kinematic viscosity.

Previous simulations of the canonical shock-turbulence interaction have considered a parameter space of M_t, Re_λ, and M_s [e.g. 45, 46, 76], but experimental studies have observed that turbulence amplification across a shock depends also on the lengthscales of the upstream turbulence [3]. If turbulent lengthscales affect the shock-turbulence interaction directly, rather than through another non-dimensional parameter such as Re_λ, a relevant non-dimensional ratio of that turbulent lengthscale with some other lengthscale of the problem must exist. The only other lengthscales available in the canonical shock-turbulence problem are the instantaneous shock thickness and a reference lengthscale associated with unsteady shock motion, such

as the root-mean-square of the perturbation in the shock position relative to its mean streamwise location, denoted ξ_{rms}.

The shock thickness, which will be on the order of the mean free path for strong shocks, is often assumed to be much smaller than all other lengthscales in the flow. Increasing the Reynolds number of the flow would be expected to reduce the smallest scales of the turbulence and for high-Re_λ flows one might be concerned that an overlap of turbulent and shock-thickness scales could be possible even for strong shocks. Scaling arguments suggest that the thickness of the shock decreases faster than the smallest turbulent scales as the Reynolds number is increased, leading to a ratio of the Kolmogorov lengthscale, η, to mean-free-path, λ_m, that scales with [67]

$$\frac{\eta}{\lambda_m} = C\frac{Re_q^{1/4}}{M_t}, \tag{1.10}$$

where $Re_q = R_{ii}^2/(\varepsilon\nu)$ is the turbulence Reynolds number and C is an order one constant that depends on γ and the model used for molecular collisions in the gas. Re_λ scales with $\sqrt{Re_q}$ [69] and, in high Re_λ flows, (1.10) suggests that the shock thickness is much smaller than the smallest turbulent scales except under exceptionally large M_t conditions that are not addressed in this study. Likewise, because the shock thickness is much smaller than other lengthscales in the flow it is reasonable to treat the shock as a discontinuity, which justifies the use of a numerical shock capturing scheme, and (1.10) suggests that the ratio of shock thickness and turbulent lengthscales is not an independent quantity that could affect the subject canonical shock-turbulence problem.

An alternative measure that might affect the subject problem is the non-dimensional ratio of the amplitude of perturbations in the shock position, ξ_{rms}, with some upstream turbulent lengthscale. For the statistically steady canonical shock-turbulence problem, ξ_{rms} must be a function of quantities describing the state of the upstream turbulence and the shock. Given the previous argument that the shock may be treated as a discontinuity with no finite lengthscale describing its thickness, dimensional analysis would suggest that ξ_{rms}, which as units of length, must be proportional to some upstream turbulent lengthscale. LIA has predicts that perturbations in the shock position as a shock passes through a plane wave vorticity mode are proportional to the wavelength of that mode, which would suggest that ξ_{rms} is driven predominately by the larger energetic scales of the turbulence. Regardless, the proportionality of ξ_{rms} to upstream turbulent lengthscales implies that the ratio of turbulent lengthscales to ξ_{rms} is not an independent parameter that could be changed

to influence the behavior of shock-turbulence interactions, at least within simple problem geometry considered here.

1.3 Dissertation outline

Directly solving (1.1) at high Re_λ is impractical, and application of modeling approaches capable of reaching large Re_λ regimes to the canonical shock-turbulence problem remains difficult. The work contained in this dissertation aims to offer improvements to RANS and LES modeling of shock-turbulence interactions, and leverage these improvements in LES to investigate the dynamics of inertial range turbulent flows interacting with shocks, within regimes that are inaccessible by contemporary DNS.

The layout of the subsequent work is as follows. Chapter 2 introduces the fundamental LES approach to the canonical shock-turbulence problem used in this study. Preliminary simulations found that aliasing errors in the upstream turbulence had a substantial influence on the interaction of the turbulence with the shock, and Chapter 3 proposes a method for alleviating these errors in a low cost, localized manner. Chapter 4 utilizes the developments of the previous chapter and considers the results of high resolution LES of the canonical shock-turbulence problem, focusing on the dynamics of the inertial range scales which have not been investigated in previous, lower Reynolds number DNS. Chapter 5 approaches the canonical-shock turbulence problem in RANS, and a model for the corrugations in the shock is developed that improves the numerical behavior of the underlying RANS model.

Chapter 2

LES OF THE CANONICAL SHOCK-TURBULENCE PROBLEM: BACKGROUND

2.1 Introduction

LES only resolves the large energetic scales of the flow, while relying on modeling to represent the effects of small scale eddies, but it is otherwise fundamentally similar to performing DNS. As a result, there is a breadth of literature regarding the basic problem construction, such as methods for producing isotropic turbulence upstream of the shock [68] and boundary conditions that will avoid a mean drift in the shock as it passes through the turbulent flow [45]. Some numerical results from DNS, such as scale separation requirements for effective shock capturing [85], also have useful analogues in LES. Furthermore, DNS provides insights into what physics the Subgrid Scale (SGS) model used in the LES will need capture, and the choice of SGS model is also supported by previous studies comparing the relative effectiveness of different models in LES of shock-turbulence interactions [6, 35].

Despite some similarities with DNS, LES faces a number of difficulties when simulating the interaction of turbulence with a shock. Previous studies have addressed the numerical application of LES to the canonical shock-turbulence problem, and have often focused on the effective discontinuity in the flow field at the shockwave. In LES, shockwaves that are unresolved at the mean free path scale are often numerically stabilized by application of additional dissipation, and care must be taken to avoid associated excessive dissipation being applied to the turbulence. The unresolved flows accompanying shocks and turbulence are fundamentally different, and one solution has been to combine an explicit SGS model for the turbulence with a numerical shock capturing scheme applied only in the direct vicinity of the shock [6, 21, 22, 47]. Deconvolution methods [1, 35] provide a more unified approach to shock capturing and turbulence modeling, although a sensor to modify model parameters near the shock may be still required [35].

This chapter provides a brief overview of the modeling approaches used in LES of the canonical shock-turbulence interaction. Section 2.2 describes the computational domain of the LES and the method for producing pre-shock turbulence. Section 2.3 develops the equations governing the LES, which contain unclosed terms that are

modeled in section 2.4. Methods used for computing turbulent statistics in the LES are addressed in section 2.4.1. Subsequent chapters, 3 and 4, discuss modifications to the existing modeling techniques and the results of the LES, respectively.

2.2 Flow description

The canonical shock-turbulence LES considers a transversely periodic $L_x \times 2\pi \times 2\pi$ channel, as shown in Figure 2.1, containing a nearly stationary normal shock located shortly downstream of the inflow boundary at x_s. Isotropic, homogeneous turbulence is introduced at the inlet upstream of the shock, and passes through the shock as it travels down the channel. A sponge zone is located at the outflow boundary to prevent acoustic reflections [24]. The flow is initialized with the laminar Rankine-Hugoniot jump conditions, and because of the perturbations on the shock from the upstream turbulence this yields a small drift in the mean shock position [45]. This drift velocity was found to be negligibly small in the LES, which is consistent with DNS at similar shock Mach numbers and turbulence intensities [76].

The inlet turbulence is produced from a separate simulation of forced isotropic turbulence in a periodic box with a mean background velocity equal to the shock speed. These simulations are henceforth referred to as box-turbulence simulations. The solenoidal part of the filtered velocity field is forced at wavenumbers $k_0 - 1/2 < k < k_0 + 1/2$ [68] until it becomes statistically steady with peak energetic wavenumber k_0, and then planar samples from a fixed location in the domain are introduced as ghost cells in the shock-turbulence LES.

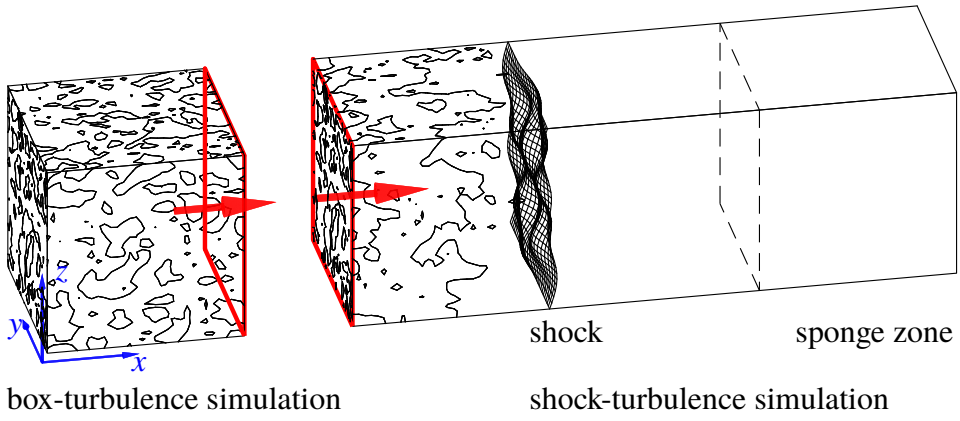

Figure 2.1: Layout of the LES. Isotropic turbulence with the same mean velocity as the flow upstream of the shock is forced at a statistical steady state in a periodic box LES (left). A plane of the flow in the periodic box (red) is copied into the inlet of a transversely periodic channel (right) containing a nearly stationary shock.

2.3 LES Governing Equations

LES is motivated as a solution to the formally filtered Navier-Stokes equations, which are found by applying a convolution filter of the form

$$\bar{f}(\underline{x}) = \int G(\underline{x} - \underline{x}')\, f(\underline{x}')d\underline{x}' \tag{2.1}$$

to the governing equations. The kernel of the filter is not explicitly defined but is assumed to be implicitly related to the mesh spacing, and fulfills the normalization condition [69]

$$\int_{-\infty}^{\infty} G(\underline{r})\, d\underline{r} = 1. \tag{2.2}$$

Details on this filtering procedure are discussed in Rogallo and Moin [75]. The cutoff wavenumber is defined to be the largest wavenumber resolved in the filtered solution, and here it is taken to be solely a function of the mesh. Generally, the mesh spacing upstream and downstream of the shock are the same, with any refinement localized to only the direct vicinity of the shock, and so it is further assumed that the cutoff wavenumber is left unchanged by a shock.

Given a conceptual convolution filter of the form of (2.2), and applying a Favre-filter defined as

$$\tilde{\phi} = \frac{\overline{\rho\phi}}{\bar{\rho}}, \tag{2.3}$$

to the governing equations, (1.1), the Favre-filtered Navier-Stokes equations for a single component fluid are [37]

$$\frac{\partial \overline{\rho}}{\partial t} + \frac{\partial \overline{\rho}\tilde{u}_j}{\partial x_j} = 0, \tag{2.4a}$$

$$\frac{\partial \overline{\rho}\tilde{u}_i}{\partial t} + \frac{\partial \overline{\rho}\tilde{u}_i\tilde{u}_j + \overline{p}\delta_{ij}}{\partial x_j} = \frac{\partial \tilde{\sigma}_{ij}}{\partial x_j} - \frac{\partial \tau_{ij}}{\partial x_j}, \tag{2.4b}$$

$$\frac{\partial \overline{E}}{\partial t} + \frac{\partial (\overline{E} + \overline{p})\tilde{u}_j}{\partial x_j} = \frac{\partial}{\partial x_j}\left(\kappa \frac{\partial \overline{T}}{\partial x_j}\right) + \frac{\partial \tilde{\sigma}_{ij}\tilde{u}_i}{\partial x_j} - \frac{\partial q_j^T}{\partial x_j}. \tag{2.4c}$$

Equation (2.4) represents the governing equations for LES, where the filtering is assumed to be implicitly related to the computational mesh, and closely resembles the original governing equations for DNS (1.1) with the addition of terms representing the interaction with the subgrid flow. The subgrid stress tensor, τ_{ij}, and subgrid heat flux, q_j^T, must generally be modeled in LES but are given formally as

$$\tau_{ij} = \overline{\rho}\left(\widetilde{u_i u_j} - \tilde{u}_i\tilde{u}_j\right), \tag{2.5a}$$

$$q_j^T = c_p\overline{\rho}\left(\widetilde{Tu_j} - \tilde{T}\tilde{u}_j\right). \tag{2.5b}$$

The subgrid kinetic energy is included in the total energy by

$$\overline{E} = \frac{\overline{p}}{\gamma - 1} + \frac{1}{2}\overline{\rho}\tilde{u}_i\tilde{u}_i + \frac{1}{2}\tau_{ii}. \tag{2.6}$$

2.4 Stretched-Vortex Model (SVM)

The subgrid-scale (SGS) terms, (2.5), cannot be computed directly in LES and must be modeled. A large number of models exist for approximating these SGS terms, and the choice of SGS model may have a significant impact on the results of the LES, as can be observed in comparisons of LES of the canonical shock-turbulence problem using different SGS models [6].

The SGS model used in the LES in this study is the Stretched-Vortex Model (SVM), with minor modifications to address aliasing errors as discussed in Chapter 3. The SVM models (2.5) by representing the flow within each computational cell as a single, nearly axisymmetric vortex aligned with the principal extensional axis of the local resolved strain rate [89]. The SVM has been shown to give reasonable results in comparisons to DNS in this problem [6], and is capable of modeling many of the physical phenomena that are expected to be important in this problem. The shock induces anisotropy in all scales of the flow, and the stretched-vortex model is capable of modeling anisotropy in SGS flows, unlike many models. The effectiveness of the SVM to capture this SGS anisotropy downstream of the shock is considered in Chapter 3. Furthermore, the SVM can model the contribution of SGS flows to turbulent statistics of interest, which is particularly useful in this problem because of the change in turbulent lengthscales across the shock. The formulation of the SVM used here does not admit a transfer of energy from the SGS flows to the resolved flows [43], called backscatter, which may be substantial downstream of a shock [57], but variants of the SVM that allow backscatter have not performed well in this problem [6]. The SVM has been previously applied successfully to similar flows such as compressible homogeneous turbulence, [43], re-shocked Richtmyer-Meshkov instabilities [37, 59], and buoyancy-driven turbulence [13].

The SGS contributions (2.5) computed from the stretched-vortex model are [43, 65]

$$\tau_{ij} = \bar{\rho}\tilde{k}' \left(\delta_{ij} - e_i^v e_j^v\right), \tag{2.7a}$$

$$q_i^T = -c_p\overline{\rho}\frac{\Delta x}{2}\sqrt{\tilde{k}'} \left(\delta_{ij} - e_i^v e_j^v\right)\left(\frac{\partial \tilde{T}}{\partial x_j}\right), \tag{2.7b}$$

where $\underline{e}^v$ is the unit vector aligned with the subgrid vortex axis. The energy spectrum associated with the stretched-vortex in each cell is [62]

$$E(k) = \mathcal{K}_0 \varepsilon^{2/3} k^{-5/3} e^{\left(-2k^2\overline{\nu}/(3|\tilde{a}|)\right)}, \tag{2.8}$$

where $\mathcal{K}_0$ is the Kolmogorov prefactor, ε is the dissipation rate, $\tilde{a} = \tilde{S}_{ij} e_i^v e_j^v$ is the strain rate along the vortex axis, and $\tilde{S}_{ij}$ is the resolved rate of strain tensor

$$\tilde{S}_{ij} = \frac{1}{2}\left(\frac{\partial \tilde{u}_i}{\partial x_j} + \frac{\partial \tilde{u}_j}{\partial x_i}\right). \tag{2.9}$$

Integrating (2.8) above the cutoff wavenumber, $k_c = \pi/\Delta x$, yields [13]

$$\tilde{k}' = \frac{1}{2}\overline{\rho}\mathcal{K}_0 \varepsilon^{2/3} \left(\frac{2\overline{\nu}}{3|\tilde{a}|}\right)^{1/3} \Gamma\left[-1/3, \frac{2\overline{\nu}k_c^2}{3|\tilde{a}|}\right], \tag{2.10}$$

where Γ is the incomplete gamma function. The factor of $\mathcal{K}_0\varepsilon^{2/3}$ is approximated by matching the second order velocity structure function of the local resolved flow, $\langle \overline{\mathcal{F}}_2(\underline{x}, \underline{r})\rangle = \left\langle (\tilde{\underline{u}}(\underline{x} + \underline{r}) - \tilde{\underline{u}}(\underline{x}))^2 \right\rangle$, to the subgrid energy spectrum (2.8). Performing the averaging in $\overline{\mathcal{F}}_2$ over a sphere of radius Δx about the center of the computational cell, the matching process returns [36, 89]

$$\mathcal{K}_0 \varepsilon^{2/3} = \frac{\langle \overline{\mathcal{F}}_2(\underline{x}, \Delta x)\rangle}{A \Delta x^{2/3}}, \tag{2.11a}$$

$$\langle \overline{\mathcal{F}}_2(\underline{x}_0, \Delta)\rangle = \frac{1}{6}\sum_{j=1}^{3}\left(\delta\widetilde{u_1^+}^2 + \delta\widetilde{u_2^+}^2 + \delta\widetilde{u_3^+}^2 + \delta\widetilde{u_1^-}^2 + \delta\widetilde{u_2^-}^2 + \delta\widetilde{u_3^-}^2\right)_j, \tag{2.11b}$$

$$A = 4\int_0^\pi s^{-5/3}(1 - \sin(s)/s)ds \approx 1.90695, \tag{2.11c}$$

where $(\delta\widetilde{u_i^\pm}^2)_j = (\tilde{u}_i(\underline{x}_0 \pm \underline{e}_j\Delta) - \tilde{u}_i(\underline{x}_0))^2$ is the squared velocity difference in component i over a distance Δ in Cartesian direction $\pm j$, relative to the cell center $\underline{x}_0$. It is noted that (2.11) assumes the subgrid flows are approximately incompressible and performing the structure function averaging over a shock is not recommended. In the presence of a shock, averaging should be performed in a manner that avoids crossing the shock [59] or the subgrid model should be disabled and the shock capturing scheme relied on for dissipation directly near the shock [6]. Preliminary simulations found that aliasing errors in the LES using the stretched-vortex model resulted in an overestimation of high-wavenumber turbulent kinetic energy in the forced turbulence upstream of the shock, and the interaction of these high-wavenumber modes

with the shock resulted in spurious behavior such as a drop in the dissipation rate across the shock. A hyperviscous filtering procedure will be developed for the LES in Chapter 3 to address this issue.

2.4.1 Turbulent statistics in LES

Turbulent statistics in LES are the same as discussed in section 1.2, except that, in LES, statistical quantities can only be directly calculated at the resolved scale. It is assumed here that the unresolved scales are incompressible and so $\rho = \bar{\rho}$ and $\mu = \bar{\mu}$. The dissipation rate is assumed to be constant with wavenumber and is taken to be equal to the dissipation of the resolved kinetic energy that arises from the sum of the stresses in (1.2) and (2.5).

An advantage of the stretched-vortex SGS model is that the subgrid flow used to construct the SGS stresses can be accounted for during post-processing of the LES. Inclusion of the SGS flows alleviates the need to artificially filter DNS or experimental results when validating the LES, and allows the LES to capture effects that may be obscured at the resolved scale. For instance, the SGS statistics are useful when addressing energy amplifications because turbulent fluctuations transferred to small scales by the shock compression may appear to be dissipated if they are mapped to wavenumbers that are not resolved on the computational mesh of the LES.

The SGS Reynolds stresses follow directly from τ_{ij} (2.7), and (2.10) allows reconstruction of the SGS kinetic energy in (2.6). A correction is added to u_{rms} and M_t using

$$u_i u_i \approx \tilde{u}_i \tilde{u}_i + 2\tilde{k}', \tag{2.12}$$

to account for the SGS kinetic energy, $\tilde{k}'$. An approximation for the Taylor microscale is obtained using the result for isotropic, incompressible turbulence,

$$\lambda \approx \sqrt{\frac{15\langle \bar{\nu} \rangle}{\varepsilon}} u_{rms}. \tag{2.13}$$

Hill and Pullin [36] derived expressions for radial energy spectra of the SGS flows in transverse planes. The vorticity of the subgrid flow is oriented along the spiral vortex axis, and so the SGS enstrophy may be written

$$\Omega_{ij}^{SGS} = \Omega_{kk}^{SGS} e_i^v e_j^v, \tag{2.14a}$$

$$\Omega_{ii}^{SGS} = 2 \int_{k_c}^{\infty} k^2 E(k) dk, \tag{2.14b}$$

where $\Omega_{ij} = \omega_i \omega_j$. Inserting the subgrid spectrum (2.8) into (2.14) and integrating provides an approximation to the enstrophy associated with the local subgrid flow

$$\Omega_{ij}^{SGS} = \mathcal{K}_0 \varepsilon^{2/3} \left(\frac{2\overline{\nu}}{3|\tilde{a}|} \right)^{-2/3} \Gamma \left(\frac{2}{3}, \frac{2\overline{\nu}}{3|\tilde{a}|} k_c^2 \right) e_i^v e_j^v. \tag{2.15}$$

Chapter 3

LES OF THE CANONICAL SHOCK-TURBULENCE PROBLEM: REGULARIZATION METHOD

3.1 Introduction

Preliminary LES of the canonical shock-turbulence problem performed for this study using the stretched-vortex model yielded unusual results, such as observing a spurious decrease in the dissipation rate of turbulent kinetic energy across the shock in some cases. This behavior was found to be largely independent of the mesh refinement and the base mesh resolution so long as the Re_λ of the flow was large, suggesting that some modification to the LES approach discussed in Chapter 2 was required.

The purpose of the work in this chapter is to address the challenges presented by the mean compression ratio over the shock in LES, and the resulting expectation that the turbulent flow scales would decrease in size as the flow passes through a shock. Experiments have confirmed that a decrease in the integral length scale occurs [2, 4], and the DNS of Larsson and Lele [45] found a decrease in both the streamwise and transverse Taylor microscales, although Agui et al. [2] did not observe a change in this scale in the transverse directions. The length scales grow downstream of the shock, but it can be seen from DNS [45, 46] that even the small scales take a substantial amount of time relative to the dissipation time scales to return to their upstream size.

The decrease in flow scales over a shockwave at a constant cutoff wavenumber results in an abrupt transfer of energy towards smaller scale turbulent modes, passing from the scales that are resolved on the computation grid of the LES into the unresolved scales. This effect is dissipative at the resolved scales, and obfuscates some of the results that can be drawn from the resolved scale amplifications over a shockwave in LES. Thus, SGS models that utilize an approximation for the subgrid flow, such as the Stretched-Vortex Model (SVM) [43, 65], may be well suited for addressing shock-turbulence interaction problems.

In practice, the rapid transfer of modes into the subgrid scales has potential to cause broader difficulties for LES. The energy spectrum of fully developed turbulence in a physical space compressible LES rarely follows a perfectly scale-similar k^{-n}

spectrum, and may exhibit a pile up of kinetic energy near the cutoff wavenumber that is often interpreted as effective aliasing errors that are not easily corrected in physical space codes. Models that produce this pileup may perform well in validation tests of smoothly decaying turbulence, but these deviations result in a strong shock impulsively changing the shape of the spectrum at high wavenumbers.

It will be shown that this phenomenon has the potential to induce undesirable behavior in the stretched-vortex model, and other models may face the same problem. Bermejo-Moreno et al. [6] compared the performance of a number of SGS models, including the stretched-vortex model, applied to the canonical shock-turbulence problem. The spectra that developed as the turbulence decayed downstream of the shock in the LES show that many of the tested SGS models produce similar high wavenumber deviations comparable to that seen in the stretched-vortex model case. These deviations did not exist upstream of the shock in [6] because the inlet turbulence was produced from DNS, but it is reasonable to conclude high wavenumber errors and the resulting rapid change in the structure of the resolved spectrum over a shock are not phenomena limited to LES with the stretched-vortex model.

A simple correction to this issue would be to apply an explicit filtering operation that dissipates the kinetic energy pileup upstream of the shockwave, but spectral filtering is impractical in the inhomogeneous directions that are present in shock turbulence problems. Cook and Cabot [17] apply a spectral filter to the periodic directions and a high order compact finite difference filter to the inhomogeneous directions of several simplified test problems representative of shock-turbulence interactions. Likewise, Tritschler et al. [87] employ a high order compact finite difference filter to remove aliasing errors in LES of Richtmyer-Meshkov instabilities. This explicit filtering approach is problematic because it effectively decreases the highest resolved wavenumber at a given mesh resolution, and the filtering operation contributes additional dissipation that complicates the application of a dynamic LES model.

In this chapter we propose a physical space dynamic regularization method capable of applying additional dissipation in a manner that forces the spectrum towards $k^{-5/3}$ behavior in the vicinity of the cutoff wavenumber. In conjunction with a primary LES model, the regularization adds a relatively small amount of additional dissipation that is intended to remove any pileup of kinetic energy in the high wavenumbers. Validation tests are performed on forced and decaying isotropic

turbulence, and linearized models of post shock turbulence are employed to evaluate the performance of the model across a shockwave and in the anisotropic downstream flow. Tests are also conducted to show the influence of the regularization on LES with an explicitly simulated shock.

3.2 Numerical Method

The governing LES equations (2.4) are solved using the parallel Adaptive Mesh Refinement in Object Oriented C++ (AMROC) framework [19], but mesh refinement is not implemented in this chapter except for the simulations discussed in section 3.7, where shocks are explicitly simulated. Previous LES of shock-turbulence interactions have shown that local mesh refinement is necessary to resolve corrugations in the shock [26], and adaptive refinement also serves to reduce the dissipation applied to the turbulence by a localized shock capturing scheme.

The conservative, skew-symmetric formulation of the nonlinear convective terms [9, 38] are integrated spatially with a 4th order tuned centered difference scheme [36] that minimizes the truncation errors proposed by Ghosal [28]. A 3rd order strong stability preserving Runge-Kutta scheme is used for time integration [31]. The numerical approach used here has previously been applied successfully in studies of Richtmyer-Meshkov instabilities [60]. The subsequent sections consider both DNS and LES. Here, DNS is considered to be the limit of the LES equations as the viscous scales become well resolved. The same numerical approach is applied to both DNS and LES, but in the DNS cases the SGS terms (2.5) are set to zero.

The computational domain for all simulations in this chapter, except those discussed in section 3.7, is a periodic $2\pi \times 2\pi \times 2\pi$ cube, and flow is initialized as a solenoidal velocity field with constant density and pressure as per Samtaney et al. [77]. Forced turbulence is generated using a linear forcing term on the solenoidal part of the $\sqrt{\bar{\rho}}\tilde{u}$ field, band-pass filtered to $(k_0 - 0.5) < k < (k_0 + 0.5)$ [68], and this produces turbulent fields with a prescribed dissipation rate and peak energetic wavenumber $k_0 = 4$.

3.3 Dynamic Regularization Technique

3.3.1 Background

One approximation for the SGS kinetic energy dissipation in (2.5) is to use a $n \geq 2$ order Laplacian of the form

$$\frac{\partial \tau_{ij}}{\partial x_j} = C_\mu \overline{\rho}(-1)^n (\nabla^2)^n \tilde{u}_i. \tag{3.1}$$

This form is referred to as a hyperviscosity model, and is motivated by the assertion that interactions with the subgrid scales should take place predominantly at the highest resolved wavenumbers. The Fourier representation of a hyperviscous operator grows rapidly with wavenumber, allowing C_μ to be selected in such a way that the operator is only substantially dissipative near and above the highest resolved wavenumber. Hyperviscous approximations have seen a broad set of uses ranging from numerical shock capturing [16] to decaying turbulent flows (e.g., [10, 18]). The high order derivatives used in a hyperviscosity model often result in the numerical implementation of these models being quite similar to an explicit filter such as that of Lele [50], but the hypervisocity formulation allows for greater control over how the dissipation is applied.

Localization to high wavenumbers makes hyperviscous operators appealing as a regularization, but C_μ must be determined, with the possibility that an empirically derived constant value for the turbulence upstream of a shock may not be valid downstream of the shock. Dantinne et al. [18] calculates C_μ dynamically from the Germano identity [27], but this represents a different use case than the desired purpose of damping out aliasing errors in a separate SGS model.

3.3.2 Dynamic Hyperviscosity

The present proposed approximation for C_μ is based on the scaling of the velocity structure function in inertial range turbulence [5]

$$\mathcal{F}_2(\underline{x}, \Delta) \propto (\varepsilon \Delta)^{2/3}. \tag{3.2}$$

The ratio of $\mathcal{F}_2(\underline{x}, \Delta)$ calculated at separation scales Δ_1 and Δ_2, under the assumption that ε is constant in the inertial range, motivates the definition of a local smoothness parameter

$$\alpha(\underline{x}) = \frac{\langle \overline{\mathcal{F}}_2(\underline{x}, \Delta_1) \rangle}{\langle \overline{\mathcal{F}}_2(\underline{x}, \Delta_2) \rangle} \left(\frac{\Delta_2}{\Delta_1} \right)^{2/3} - 1, \tag{3.3}$$

which one expects to approach zero in inertial range turbulence in an average sense. This has similarities with the automatic flagging criteria proposed by Tantikul and Domaradzki [84]. The averaging on the structure functions is again computed over the surface of a sphere of the same radius as the separation scale, as in (2.11). In the

presence of anisotropic computational meshes or significant mean flow gradients, such as shocks, it may be preferable to replace spherical averaging with averaging along a circle or a line of points oriented in a homogeneous direction [59].

Motivated by previous hyperviscosity approaches, we propose a regularization scheme based on the diagonal part of the n^{th} Laplacian of u weighted by α. The proposed model is given by

$$\frac{\partial \tau_{ij}}{\partial x_j} = C_\mu \max(\alpha, 0)\, \bar{\rho} L_n[\tilde{u}_i], \tag{3.4}$$

$$L_n[\tilde{u}_i] = (-1)^n \sum_{j=1}^{3} \frac{\partial^{2n} \tilde{u}_i}{\partial x_j^{2n}}, \tag{3.5}$$

where the off diagonal terms in the Laplacian have been dropped in order to produce a operator whose Fourier representation grows with $k_x^{2n} + k_y^{2n} + k_z^{2n}$. This is approximately a cube when n is large, and so produces a better match to the boundary of the subject simulations in Fourier space. As n is increased, the dissipation from the operator becomes more focused at the boundary of the resolved wavenumbers in Fourier space, but the operator also becomes more expensive to compute. Negative values of α cause the model to become anti-dissipative, implying a local transfer of energy from the subgrid scales back into the resolved scales. This can be physical, but the ad hoc nature of the proposed model suggests that it cannot be expected to reliably predict the occurrence this phenomena. Thus, α is truncated at zero to reduce the influence of the regularization.

The factor C_μ is selected based on the numerical stability of the operator, noting that as C_μ becomes large one expects α to be driven to zero, enforcing a ceiling on the maximum amount of dissipation that may be applied by the model. Selecting $n = 3$, von Neumann stability analysis [52] is applied to a test problem

$$\frac{\partial \phi}{\partial t} = -C_{\mu,n=3} \alpha_{max} L_3[\phi], \tag{3.6}$$

with 2nd order centered finite differences in space and 1st order forward time-stepping. The numerical discretization of (3.6) applied to a mode of the form $\phi = \exp(i\underline{k} \cdot \underline{x} + \beta t)$ should enforce $|\exp(\beta \Delta t)| \leq 1$ for all wavenumbers to avoid exponential growth in the solution, and this suggests a choice of

$$C_{\mu,n=3} = \frac{\Delta x^5 \bar{c}}{96 \alpha_{\max}}, \tag{3.7}$$

where $\bar{c}$ is the local sound speed, α_{max} is a constant upper bound on α, and $\bar{c}\Delta t/\Delta x = 1$ is assumed. The resulting model used in this study is then given by

$$\frac{\partial \tau_{ij}}{\partial x_j} = \frac{\Delta x^5 \bar{c}}{96\alpha_{\max}} \min\left(\max\left(\alpha, 0\right), \alpha_{\max}\right) \bar{\rho} L_3[\tilde{u}_i], \tag{3.8a}$$

$$q_i^T = 0. \tag{3.8b}$$

The bound on α is artificially enforced, but in practice $\alpha_{\max}$ is taken to be larger than the values that α achieves in flows started with smooth initial conditions. Unless otherwise noted, $\alpha_{max} = 10$ is selected in this work, and the separation scales in (3.3) are taken to be factors of the mesh resolution $\Delta_1 = \Delta x$ and $\Delta_2 = 2\Delta x$.

It should be noted that care must be taken to calculate the structure functions in (3.3) in a consistent manner, as they are physically local but global with respect to wavenumber. This results in an inconsistency where the structure functions calculated at separation scales wider than the mesh cutoff, e.g., $\langle \overline{\mathcal{F}}_2(\underline{x}, 2\Delta x)\rangle$, are influenced by wavenumbers above those associated with the separation scale, while $\langle \overline{\mathcal{F}}_2(\underline{x}, \Delta x)\rangle$ contains limited higher wavenumber information. To reduce this effect, $\langle \overline{\mathcal{F}}_2(\underline{x}, 2\Delta x)\rangle$ is calculated on a mesh restricted to a cell size of $2\Delta x$, and then the resulting values are prolonged back onto the cell size Δx mesh.

3.3.3 Hybrid Stretched-Vortex Model (HSVM)

A regularized version of the stretched-vortex model is introduced by combining the terms from (2.7) and (3.8). The resulting subgrid model is given by

$$\frac{\partial \tau_{ij}}{\partial x_j} = \frac{\partial}{\partial x_j}\left(\bar{\rho}\tilde{k}'\left(\delta_{ij} - e_i^v e_j^v\right)\right) + \frac{\Delta x^5 \bar{c}}{96\alpha_{\max}} \min\left(\max\left(\alpha, 0\right), \alpha_{\max}\right) \bar{\rho} L_3[u_i], \tag{3.9a}$$

$$q_i^T = -c_p \overline{\rho} \frac{\Delta x}{2} \sqrt{\tilde{k}'}\left(\delta_{ij} - e_i^v e_j^v\right)\left(\frac{\partial \tilde{T}}{\partial x_j}\right). \tag{3.9b}$$

This Hybrid Stretched-Vortex Model (HSVM) will be shown to attenuate the high wavenumber deviation produced by the stretched-vortex model through the application of a comparably small amount of additional dissipation from the hyperviscous regularization.

3.4 Forced Isotropic Turbulence

The hyperviscous regularization (3.8) contains no tuned parameters except for some selected bound on α, suggesting that it should be applicable to a broad range of flow

conditions. Simulations of forced isotropic turbulence are conducted to evaluate the effectiveness of the dynamic hyperviscous model without tailored empirical tuning on the constant α_{max}. In order to isolate the effect of the regularization, the resolved viscosity is set to zero and there is no other SGS model used in these simulations. Compensated spectra after the turbulence has relaxed to a statistical steady state are shown in Figure 3.1 for simulations at different resolutions, turbulent Mach numbers, and values of α_{max}. Halving the value of $\alpha_{\max}$ from 10 to 5 in the 32^3, $M_t = 0.18$ test is shown to have a discernible, but small effect on the shape of the spectrum. The hyperviscous regularization consistently produces an approximate $k^{-5/3}$ spectrum without requiring tuning α_{max} or global averaging on α.

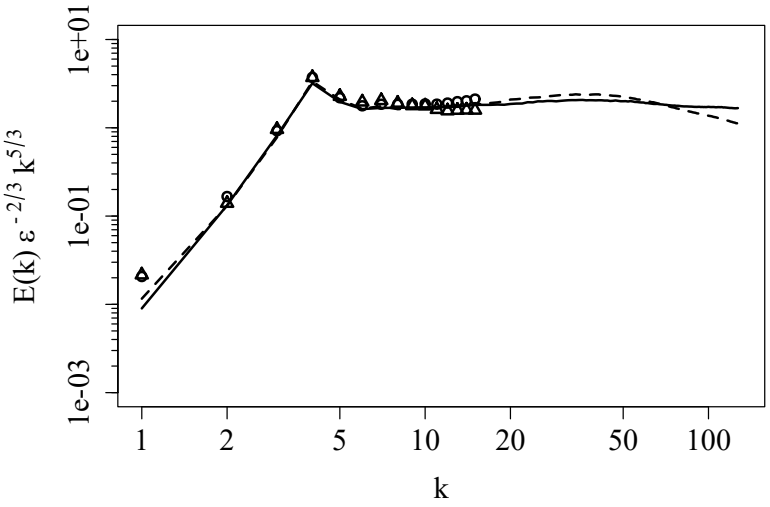

Figure 3.1: Compensated energy spectra from forced periodic isotropic turbulence with the dynamic hyperviscous model and no resolved viscosity. Solid line: 256^3 resolution, $M_t = 0.18$, $\alpha_{max} = 10$. Dashed line: 256^3 resolution, $M_t = 0.06$, $\alpha_{max} = 10$. Circles: 32^3 resolution, $M_t = 0.18$, $\alpha_{max} = 10$. Triangles: 32^3 resolution, $M_t = 0.18$, $\alpha_{max} = 5$.

The behavior of forced turbulence in LES using the stretched-vortex model, hyperviscous regularization, or hybrid stretched-vortex model is considered in Figure 3.2. The spectra shown are generated from statistically steady, forced isotropic turbulence simulations in a 64^3 periodic box. A 512^3 DNS with $k_{max}\eta > 1.5$ is provided for comparison. The forcing is tailored to produce $M_t = 0.18$ and $Re_\lambda = 100$ in the DNS, and the energy injection rate from the forcing and the resolved viscosity are the same in the LES and DNS simulations.

All three LES equilibrate to spectra that agree well with the DNS at low wavenumbers. The forced DNS appears to be slightly shallower than a $k^{-5/3}$ spectrum, which can also be observed in comparable DNS considered by Petersen and Livescu [68]. The SGS models assume a $k^{-5/3}$ inertial range exists, and as a result the LES spectra are steeper than the DNS at high wavenumbers for all of the tested models. The HSVM-LES produces an improved approximation to a $k^{-5/3}$ spectrum relative to the SVM-LES even at wavenumbers that are not immediately near the cutoff wavenumber.

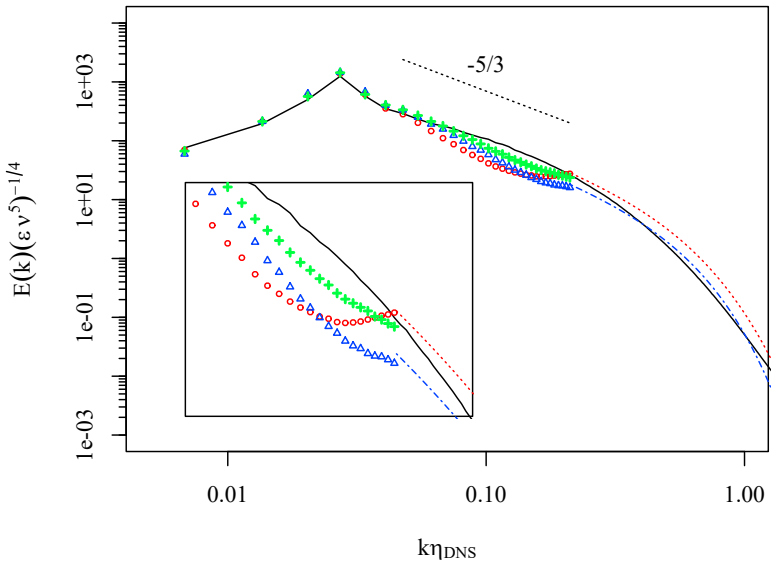

Figure 3.2: Energy spectra from forced, periodic, isotropic turbulence. DNS results are for $M_t = 0.18$ and $Re_\lambda = 100$, and the wavenumbers are normalized by the value of η calculated from DNS. The viscosity and the energy injection rate of the forcing are the same for all simulations. The inset shows the behavior of the spectra in the vicinity of the LES cutoff wavenumber. Solid line: DNS. Pluses: hyperviscosity-LES. Circles: SVM-LES. Triangles: HSVM-LES. Dotted line: SVM-LES subgrid spectrum. Dash-dot line: HSVM-LES subgrid spectrum

Figure 3.3 shows the relative magnitude of each dissipative term in HSVM-LES of statistically steady forced turbulence at a number of different flow conditions. The high resolution of the runs ensures that the dissipation associated with each term is effectively constant in time. These LES demonstrate that the hyperviscous regularization represents a secondary contribution to the dissipation rate in HSVM-

LES of inertial range isotropic turbulence. It is considered ideal to minimize the influence of the hyperviscosity because the stretched-vortex model accounts for a broader range of physics, such as Reynolds number effects and SGS heat conduction, and it has been suggested that high order hyperviscous operators may generate spurious behavior in LES [41].

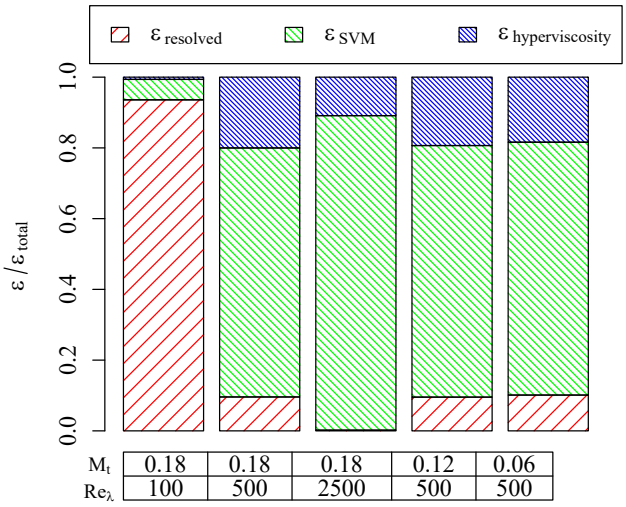

Figure 3.3: Fraction of the dissipation that arises from each dissipative term in HSVM-LES of forced, isotropic turbulence at a resolution of 256^3. Each bar represents a different simulation with parameters given in the table on the bottom of the plot.

3.5 Decaying Isotropic Turbulence

Once the DNS and HSVM-LES shown in Figure 3.2 reach a steady state, the forcing is turned off and the turbulence is allowed to decay. Figure 3.4 shows the decay of the turbulent kinetic energy, normalized by its value in the DNS at the time, $t = 0$, at which the forcing is disabled. The time is nondimensionalized by the large eddy turnover time calculated from the DNS at $t = 0$. The symbols show the DNS results restricted to a 64^3 box in physical space, which is analogous to the resolved scale LES. The total kinetic energy in the LES is found by adding the subgrid kinetic energy (2.10) to the resolved kinetic energy, and this provides a comparison to the unfiltered DNS. The HSVM-LES agrees well with DNS with regards to both the initial kinetic energy produced by the forcing and its subsequent decay after the forcing has been disabled. The agreement is particularly good at early times when

the Reynolds number remains large.

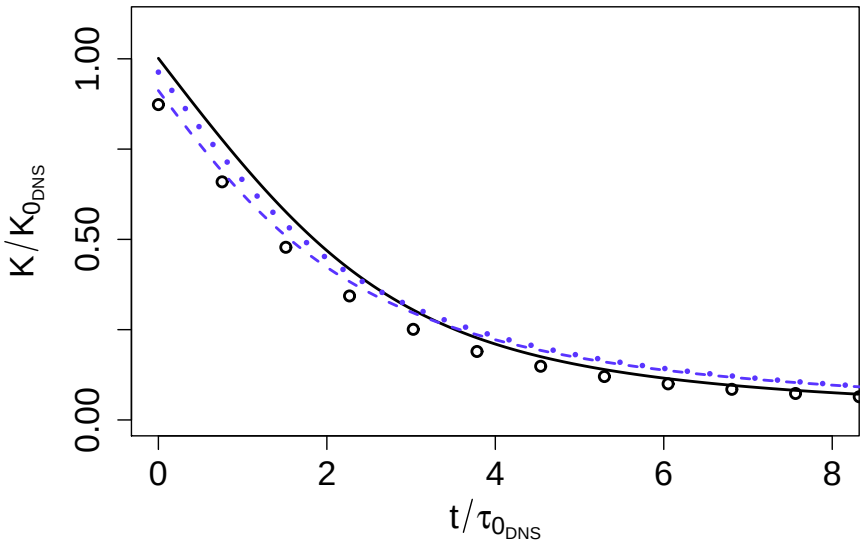

Figure 3.4: Turbulent kinetic energy decay. At $t = 0$ the DNS has $M_t = 0.18$ and $Re_\lambda = 100$. Solid line: DNS. Circles: DNS restricted to 64^3 in physical space. Dash-dotted line: resolved scale HSVM-LES. Dashed line: combined resolved and subgrid scale HSVM-LES.

Figure 3.5 compares the LES with and without the hyperviscosity to existing DNS [77]. The flow is initialized with $M_t = 0.5$ and $Re_\lambda = 72$ on a 64^3 mesh and immediately allowed to decay. The stretched-vortex model has been shown to agree well with DNS in this test problem [36, 43], and the inclusion of the hyperviscosity only slightly increases the overall dissipation.

3.6 Modeled Post Shock Turbulence

3.6.1 SGS Model Response to LIA

The abrupt compression of turbulence as it passes through a shockwave and the resulting downstream anisotropy present a complex flow that is of interest in LES. Effective numerical stabilization of a shock in turbulent flow remains a difficult problem, and this motivates the use of test problems that capture the general character of the flow downstream of a shock without the risk of introducing errors from the explicit simulation of a shockwave.

One such test problem is to use Linear Interaction Analysis (LIA) to model the

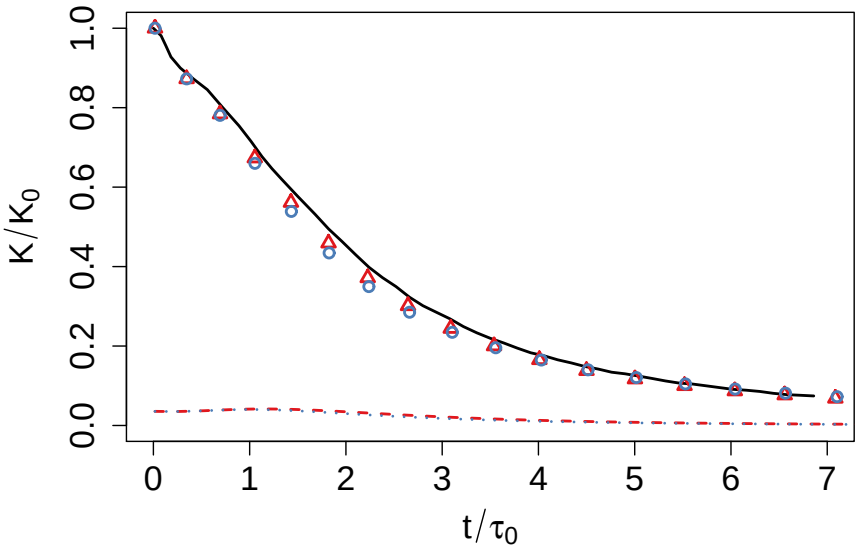

Figure 3.5: Turbulent kinetic energy decay in flow initialized with $M_t = 0.50$ and $Re_\lambda = 72$. Solid line: DNS of Samtaney et al. [77]. Circles: combined resolved and subgrid scale HSVM-LES. Triangles: combined resolved and subgrid scale SVM-LES. Dotted line: subgrid scale HSVM-LES. Dashed line: subgrid scale SVM-LES.

flow downstream of a shock. LIA models the interaction of a turbulent flow with a shock as described in detail in Appendix A, and the application of LIA to statistically steady SVM-LES highlights the problems that may be caused by a buildup of kinetic energy near the cutoff wavenumber. Figure 3.6 shows the energy spectrum for forced isotropic turbulence in SVM-LES and the spectrum that results from application of LIA to that flow field for a $M_s = 1.2$ shock. The solid and dashed lines shows spatially averaged SGS spectra for the pre-LIA and post-LIA fields, respectively, and these are extended into the resolved wavenumbers to show how the SGS model matches with the resolved spectra.

LIA acts to compress and amplify the turbulence, shifting the spectrum to higher wavenumbers and truncating off energy in the highest wavenumbers if those turbulent modes are mapped to wavenumbers above the cutoff wavenumber. A pileup of kinetic energy existing in the pre-LIA turbulence at k_c is thus partially dissipated by the shock and replaced by the energy contents of the lower wavenumbers. The modeled SGS spectra are strongly influenced by the high wavenumber behavior

of the turbulence and, as a result of the loss in high wavenumber energy, the amplification of the SGS spectra is effectively negligible. This is in conflict with the LIA prediction that the amplification should be independent of wavenumber, suggesting that the stretched-vortex SGS model would under predict dissipation in the post-LIA flow.

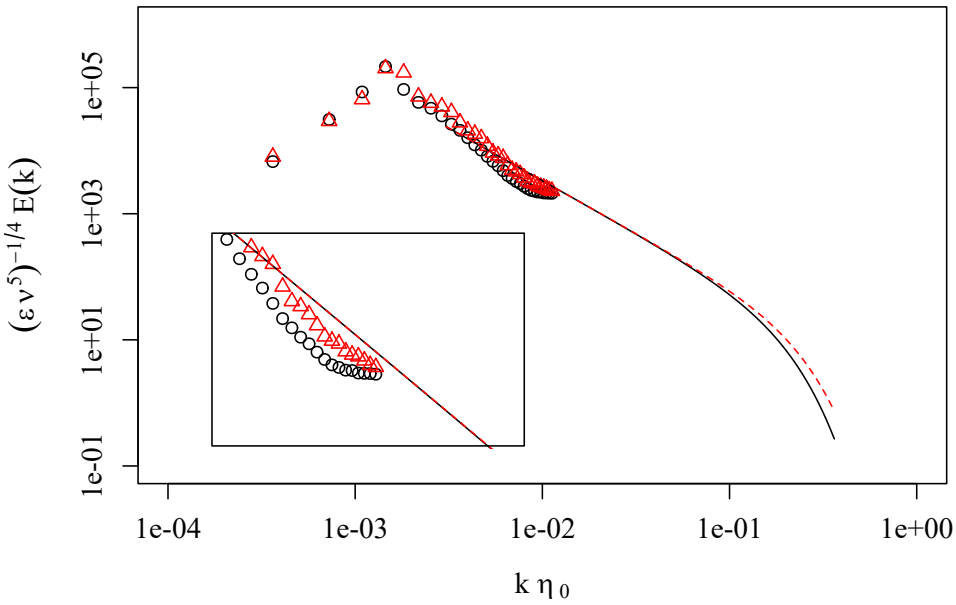

Figure 3.6: LIA predicted amplification of the energy spectrum over a $M_s = 1.2$ shock applied to turbulence produced with the stretched-vortex model. The pre-LIA flow field is statistically steady turbulence from a 64^3 SVM-LES with $Re_\lambda \approx 500$ and $M_t \approx 0.18$. The inset shows the behavior of the spectra in the vicinity of the LES cutoff wavenumber. Circles: pre-LIA resolved spectrum. Triangles: post-LIA resolved spectrum. Solid line: pre-LIA averaged SGS spectrum. Dashed line: post-LIA averaged SGS spectrum.

To further motivate the usefulness of regularizing the upstream turbulence, Figure 3.7 shows the amplification in the SGS kinetic energy that results from the application of LIA to isotropic turbulence in SVM-LES and HSVM-LES. Isotropic, forced turbulence from each LES is subjected to LIA at various shock Mach numbers, and the SGS kinetic energy is computed on the post-LIA flow field using (2.10). The results are normalized with respect to the values in the pre-LIA LES. A reference analytical result for the SGS kinetic energy amplification is found by performing

LIA with the model shell-summed energy spectrum,

$$E(k) = \begin{cases} k^2 & 0 \le k < k_0 \\ k_0^2 (k/k_0)^{-5/3} & k_0 \le k \le 256 \\ 0 & k > 256 \end{cases} \tag{3.10}$$

under the assumption of isotropy, and computing the amplification in the kinetic energy at wavenumbers above the cutoff wavenumber from the LES, $k_c = 32$. All LIA results discussed in this chapter are taken at a distance $k_0 x = 400$ from the shock, at which exponentially decaying pressure modes have fully decayed and the solution has sufficiently approached its far-field asymptote. The amplification in the SGS kinetic energy is substantially larger than the amplification in the total kinetic energy because of the transfer of energy towards higher wavenumbers. The HSVM-LES captures the LIA amplification in the SGS kinetic energy reasonably well while the SVM-LES tends to predict lower amplifications, in some cases even seeing a decrease in SGS kinetic energy.

The post-LIA SGS streamwise and transverse Reynolds stresses from the HSVM-LES are plotted in Figure 3.8, and compared with the results from LIA applied to the isotropic shell-summed energy spectrum in (3.10). The hybrid stretched-vortex model captures the amplification of the transverse Reynolds stress but predicts a SGS flow that is considerably closer to isotropy than that produced by LIA of the shell-summed spectrum. However, DNS have not consistently observed the strong Reynolds stress anisotropy predicted by LIA at high shock Mach numbers [46], and so it may not be critical for the SGS model to be capable of reproducing this phenomena.

Even using upstream turbulence from DNS, certain models tested by Bermejo-Moreno et al. [6] in shock-turbulence LES appear to exhibit behavior consistent with the result that shock compression may artificially reduce the dissipation of the SGS model. In these cases, the SGS dissipation is initially weakly amplified, but grows significantly in the region immediately downstream of the shock rather than decreasing monotonically as has been observed in DNS [46]. The referenced LES used a dissipative shock capturing scheme that could introduce similar effects, but the LIA analysis presented here suggests that the shock capturing scheme may not be solely responsible for this behavior.

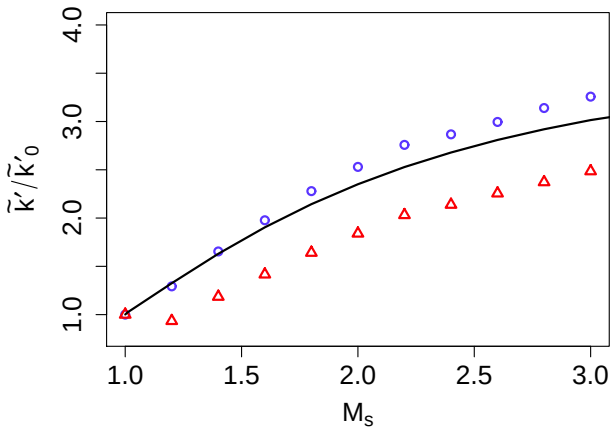

Figure 3.7: Amplification of the SGS kinetic energy under application of LIA. The LES are on a 64^3 grid with pre-LIA conditions of $Re_\lambda \approx 500$ and $M_t \approx 0.18$. Circles: HSVM-LES. Triangles: SVM-LES. Solid line: LIA kinetic energy amplification above $k = 32$ for isotropic turbulence with a model shell-summed energy spectrum.

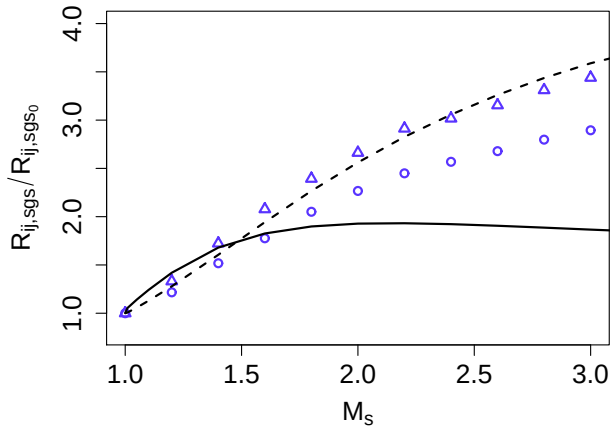

Figure 3.8: Amplification of the SGS components of the streamwise and transverse Reynolds stresses under application of LIA. The LES are on a 64^3 grid with pre-LIA conditions of $Re_\lambda \approx 500$ and $M_t \approx 0.18$. The streamwise direction is defined as the direction parallel to the mean shock normal direction in LIA. Circles: HSVM-LES streamwise Reynolds stress. Triangles: HSVM-LES transverse Reynolds stress. Solid and dashed line: streamwise and transverse Reynolds stress amplification, respectively, above $k = 32$ from LIA applied to a model shell-summed energy spectrum.

3.6.2 Decay of LIA Turbulence

Post-LIA fields are used as initial conditions in decaying turbulence simulations to evaluate the performance of the SGS models in the compressed flow. DNS of forced turbulence is conducted at a resolution of 256^3, with $Re_\lambda = 60$ and $M_t = 0.18$, and forced HSVM-LES with the same energy input and viscosity is performed at a resolution of 64^3. Once statistically steady, the domain of the DNS is extended to 512^3 in Fourier space and LIA is applied to the LES and DNS to generate post shock fields. The estimated change in the Kolmogorov length scale over a shockwave [45]

$$\frac{\eta_2}{\eta_1} \approx \left(\frac{T_2}{T_1}\right)^{3/8} \left(\frac{\rho_2}{\rho_1}\right)^{-1} \tag{3.11}$$

suggests that $k_{max}\eta > 1.5$ remains satisfied in the DNS after LIA has been applied for a $M_s = 1.5$ shock.

The decay of the streamwise and transverse Reynolds stress, normalized by their unfiltered pre-LIA values, is shown in Figure 3.9 for DNS and HSVM-LES initialized with the post-LIA fields. Time is nondimensionalized by the large eddy turnover time from the pre-LIA DNS. The resolved Reynolds stress amplification and decay predicted by the HSVM-LES agrees well with the filtered DNS, although the dissipation of the transverse Reynolds stress appears to be slightly over predicted in the HSVM-LES. The post-LIA total Reynolds stresses, which include contributions from the SGS flows, initially agree with the unfiltered DNS, but the SGS components of the LES appears to quickly decay. The subgrid continuation (2.8) that is used to compute the SGS Reynolds stresses assumes an inertial range, and so the SGS statistics are less reliable at the subject Reynolds numbers.

The Reynolds stress anisotropy in the decaying post-LIA fields is provided in Figure 3.10. LIA does not impart the same anisotropy to both simulations at the initial time, but one would not necessarily expect the anisotropy to be instantaneously equal because the pre-LIA DNS and HSVM-LES are only related by their mean statistics. Regardless, both the DNS and HSVM-LES decay to similar levels of anisotropy, and neither returns to isotropy within the duration of the simulations. The post-LIA fields decay to an anisotropy that lies close to the far field value from LIA applied to the isotropic shell-summed spectrum (3.10).

The decay of the post-LIA turbulence faces different boundary conditions than spatially decaying turbulence downstream of a shock, and so it is not guaranteed that these tests are directly representative of physically occurring flow fields even if

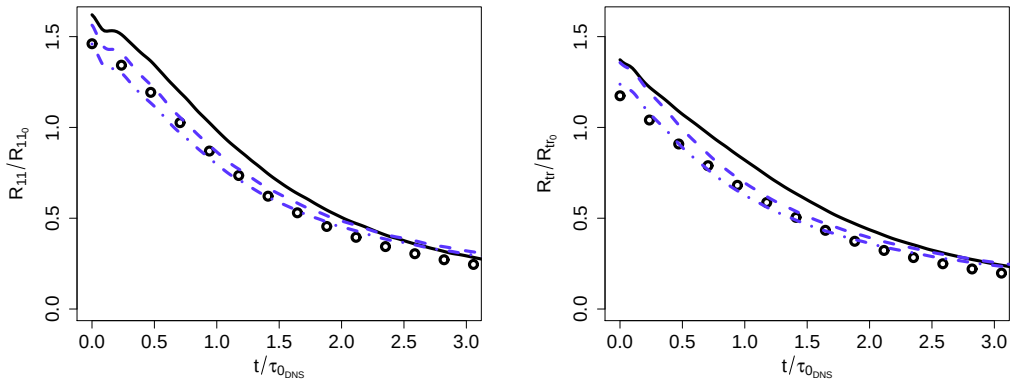

(a) Streamwise Reynolds Stress (b) Transverse Reynolds Stress

Figure 3.9: Decay of the streamwise and transverse Reynolds stresses in post-LIA periodic, anisotropic turbulence. The flow upstream of the $M_s = 1.5$ shock has $Re_\lambda = 60$ and $M_t = 0.18$. Solid line: DNS. Circles: DNS restricted to 64^3 in physical space. Dashed line: resolved scale HSVM-LES. Dotted line: combined resolved and subgrid scale HSVM-LES.

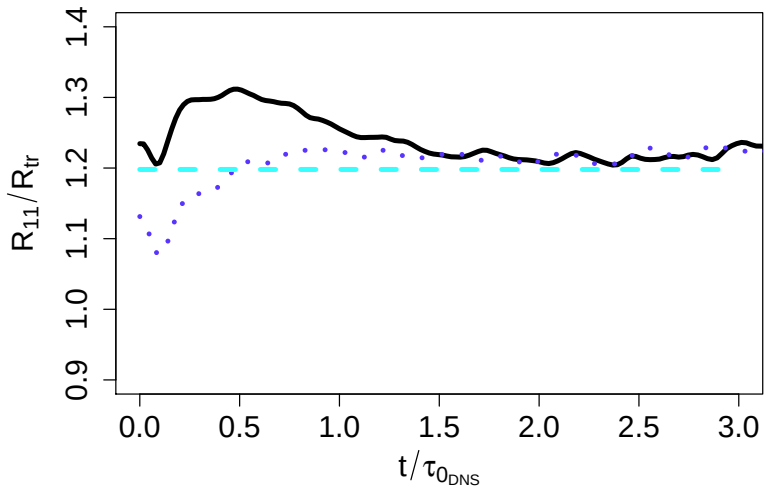

Figure 3.10: Reynolds stress anisotropy in post-LIA decaying turbulence. The flow upstream of the modeled $M_s = 1.5$ shock has $Re_\lambda = 60$ and $M_t = 0.18$. Solid Line: DNS. Dotted Line: combined resolved and SGS HSVM-LES. Dashed lined: LIA far field result for shell-summed isotropic spectrum.

LIA accurately captures the behavior near the shock. Despite this, there is reasonable qualitative agreement between the post-LIA simulations and the $Re_\lambda = 20$ shock

turbulence DNS of Ryu and Livescu [76], as shown in Figure 3.11. The upstream, pre-LIA fields have a peak wavenumber of $k_0 = 8$ to improve the statistical sample and avoid box-size effects from the boundary conditions in the downstream flow. The homogeneous post-LIA results are converted to spatial coordinates by multiplying the time by the downstream convection velocity in the shock-stationary frame. The post shock Reynolds stress decay in the post-LIA simulations is slower than that seen in Ryu and Livescu [76], but appears to converge towards the full DNS as the turbulent Mach number is reduced. The post-LIA decaying turbulence is initialized with the far field LIA results which do not include the exponentially decaying pressure modes produced by the shock, and these modes are responsible for the rapid fluctuations in the streamwise Reynolds stress immediately downstream of the shock seen in the DNS.

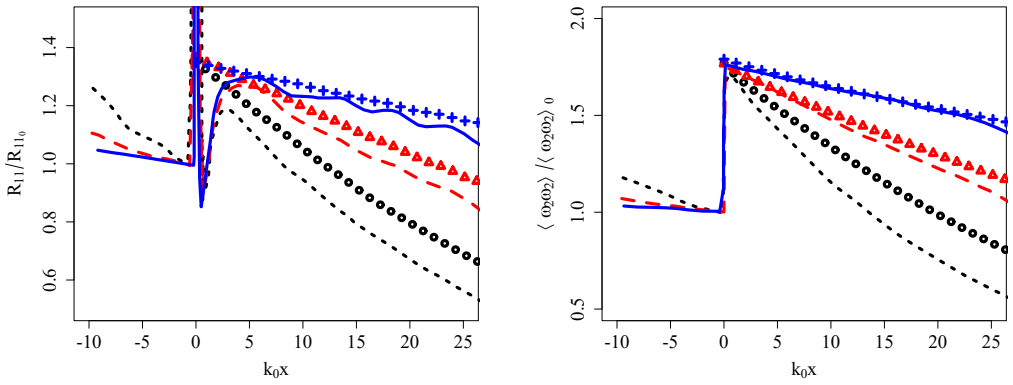

Figure 3.11: Decay of the streamwise Reynolds stress and transverse vorticity in spatial coordinates over a $M_s = 1.2$ shock, with a $Re_\lambda = 20$ upstream. The lines show the DNS of Ryu and Livescu [76] at various upstream turbulent Mach numbers: solid ($M_t = 0.04$), dashed ($M_t = 0.08$), dotted ($M_t = 0.15$). The post-LIA DNS is given by the symbols: pluses ($M_t = 0.04$), triangles ($M_t = 0.08$), circles ($M_t = 0.15$).

3.7 Shock-Turbulence Interaction

3.7.1 Flow Description

The impact of the hyperviscous regularization in full shock turbulence LES is illustrated by conducting LES of a nearly stationary shock in a transversely periodic $4\pi \times 2\pi \times 2\pi$ channel. The shock is located at approximately $x_s = \pi/2$ downstream of the inflow boundary. The shock exhibits a slow drift in its mean position [45], but the drift speed is considered negligibly small at the M_s and M_t considered

here, consistent with DNS at similar conditions [76]. A sponge zone, starting at a distance π upstream of the outflow boundary, is used to prevent acoustic reflections [24]. The inflow turbulence is produced from a separate LES of periodic turbulence forced at a statistical steady state using the same SGS model, per section 3.4. High resolution LES of the canonical shock-turbulence problem using the HSVM method are discussed in detail in Chapter 4, but this section focuses specifically on the influence of the hyperviscosity on this problem.

3.7.2 Numerical Approach

The numerical method used in the shock-turbulence simulations is the same as discussed in section 3.2, except a 5th order, shock capturing WENO scheme [36] is used in a thin band of cells near the shock. The shock location is flagged using the approximate Riemann-solver method of Lombardini [58]. Shock-capturing schemes introduce additional numerical dissipation, and so to avoid excessive dissipation the SGS terms are set to zero in regions where WENO is active, as suggested by Bermejo-Moreno et al. [6].

All LES considered in this section are performed on a $256 \times 128 \times 128$ base mesh, with a factor of $4\times$ adaptive mesh refinement (AMR) near the shock. The AMR is isotropic, so $\Delta x = \Delta y = \Delta z$ on all levels of the mesh, and AMR only refines the mesh in the immediate vicinity of the shock.

3.7.3 Results and Discussion

The behavior of the SGS model when modeling the shock with LIA, shown in Figure 3.7, would suggest that the impact of the hyperviscosity would be most noticeable in simulations with moderately low shock Mach numbers. Figure 3.12 shows turbulence statistics averaged over the homogeneous directions and time in LES with $M_t = 0.22$ and $Re_\lambda = 300$ immediately upstream of a $M_s = 1.28$ shock. The Reynolds stresses and dissipation rate include the contributions from the SGS model. A $Re_\lambda = 39$ DNS of Larsson and Lele [45] is plotted for comparison, but the DNS is only shown over a short region $k_0 x < 5$ downstream of the shock because Reynolds number effects in the downstream dissipation rate are expected to be significant at that Reynolds number. DNS considering $Re_\lambda = 40 - 75$ has observed no significant Reynolds number effects in the downstream behavior close to the shock, such as in the peak downstream streamwise Reynolds stress [46], and so it is considered comparable to the LES to the $Re_\lambda = 39$ DNS at streamwise locations close to the shock. LIA does not directly consider viscosity, but the amplification

in $\langle T^{0.76}\rangle\langle\omega_i\omega_i\rangle/\langle\rho\rangle$ predicted by LIA is plotted as an approximation to the amplification in dissipation rate. The statistics are normalized by linearly extrapolating their upstream values to the position of the shock, except in the case of the density-specific volume correlation, $b = -\langle\rho' v'\rangle$ where $v = 1/\rho$, because production of b by the shock at low M_t is driven by upstream velocity fluctuations rather than upstream density fluctuations. For small density fluctuations $b \approx \langle\rho'\rho'\rangle/\langle\rho\rangle^2$, and b is normalized by M_t^2 as suggested by the scaling in LIA.

The HSVM-LES shows larger amplifications in the Reynolds stresses across the shock, and predicts amplifications that agree with those observed in the DNS. DNS has found the vorticity amplification predicted by LIA is reasonably accurate under flow conditions comparable to those considered here [76], and the amplification in the dissipation rate, which is closely related to the vorticity, in the HSVM-LES agrees with that approximated from LIA. The density-specific volume correlation behaves similarly in the SVM-LES and HSVM-LES, which is expected since SGS heat transfer is addressed in the same manner in both models. The SVM-LES predicts lower amplifications in both the Reynolds stress components and, as predicted by the analysis in section 3.6.1, for this M_s the SVM-LES sees no amplification in the dissipation rate. In this case, the lower dissipation rate appears to roughly cancel the effect of the lower Reynolds stress amplifications, and the Reynolds stresses further downstream of the shock are similar to those seen in the HSVM-LES.

Figure 3.13 compares $Re_\lambda = 300$, $M_t = 0.15$ LES with $Re_\lambda = 73$, $M_t = 0.14$ DNS [46] across a $M_s = 1.5$ shock. The Reynolds numbers of these simulations remain different because the subject SGS models make assumptions that are only valid in inertial range turbulence, but it is possible that $Re_\lambda = 73$ is sufficiently large to approach the mixing transition to fully developed turbulence, after which Reynolds number effects are insignificant in many turbulent flows [20]. The HSVM-LES again sees a larger downstream dissipation rate than the SVM-LES, and shows better agreement with the DNS. The SVM-LES observes Reynolds stress amplifications over the shock that are similar to those seen in the HSVM-LES, and differences from the DNS in the downstream dissipation rate could be explained by the different Re_λ.

This study has focused on the behavior of the velocity field, but full LES of shock-turbulence interactions requires other fields, such as the density field, to also be captured accurately. Figure 3.14 plots the radial power spectrum of the density field upstream and downstream of the shock in the SVM-LES and HSVM-LES. The radial spectrum of a variable $f(y, z)$ with Fourier transform $\hat{f}(k_r, \theta_k)$ is given in

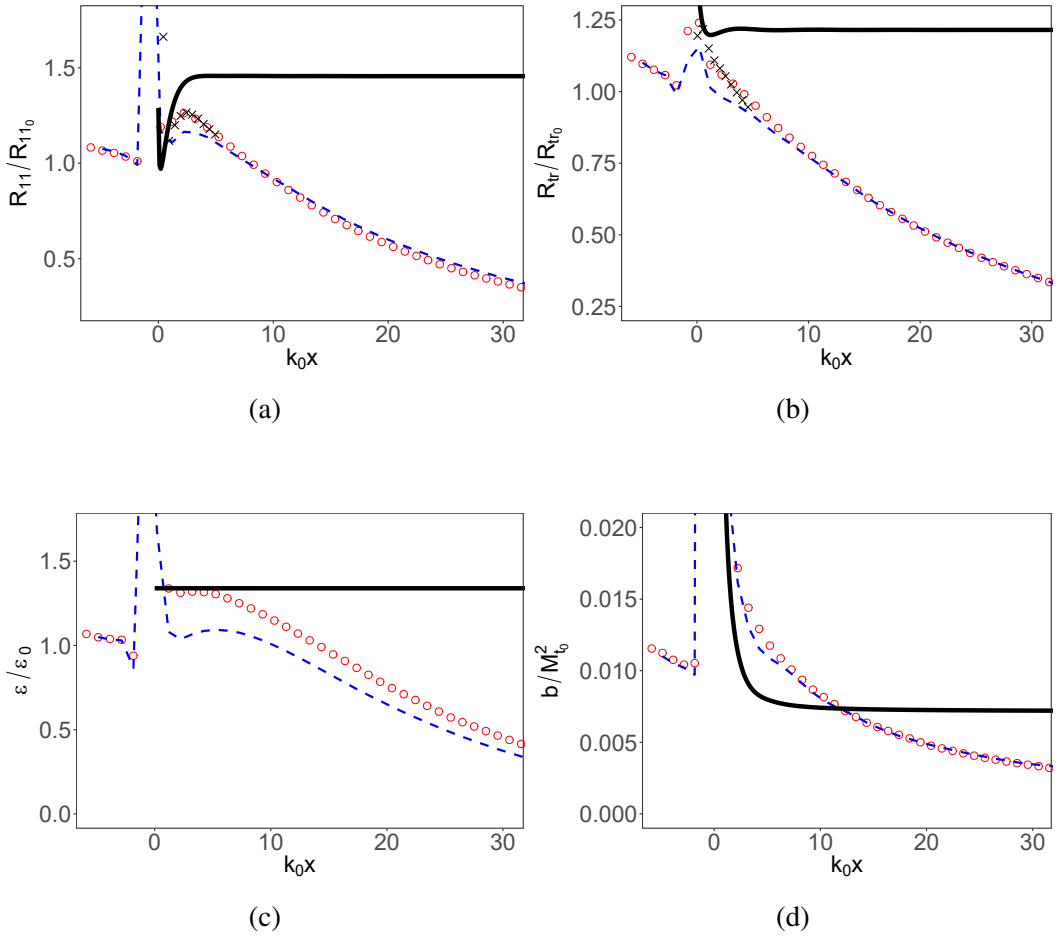

Figure 3.12: Plane-averaged statistics in flow over a $M_s = 1.28$ shock, with upstream $M_t = 0.22$. The figures show streamwise Reynolds stress (a), transverse Reynolds stress (b), dissipation rate (c), and density-specific volume correlation (d). The dissipation rate amplification from LIA is approximated by the predicted amplification in $\langle T \rangle^{0.76} \langle \omega_i \omega_i \rangle / \langle \rho \rangle$. The LES has $Re_\lambda = 300$ upstream of the shock, and the near-shock behavior of DNS with $Re_\lambda = 39$ [45] is plotted for comparison. Solid line: LIA. Dashed line: SVM-LES. Circles: HSVM-LES. Crosses: DNS [45].

terms of the radial wavenumber, k_r, and azimuthal wavenumber, θ_k, by

$$E_f^{2D}(k_r) = \frac{1}{2} k_r \int_0^{2\pi} \left| \hat{f}(k_r, \theta_k) \right|^2 d\theta_k. \tag{3.12}$$

The density spectra from the HSVM-LES and SVM-LES behave in a similar manner, illustrating that the hyperviscosity model does not significantly affect the behavior of the density field.

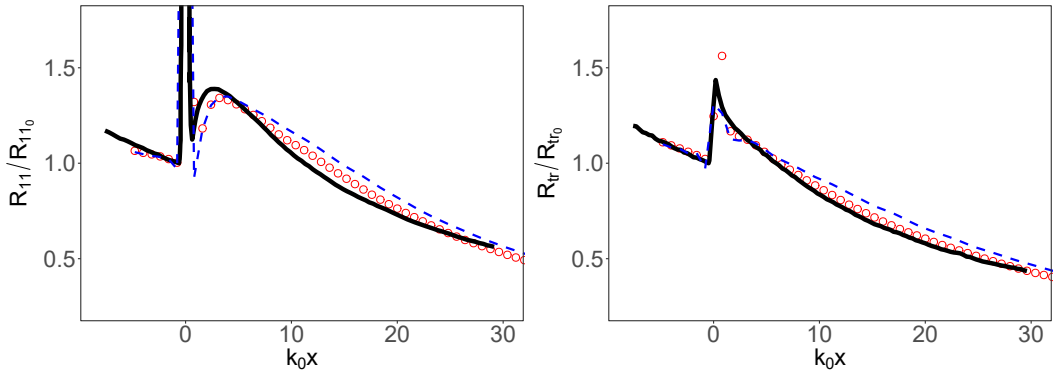

Figure 3.13: Plane-averaged Reynolds stresses in flow over a $M_s = 1.5$ shock. The LES has upstream conditions of $Re_\lambda = 300$, $M_t = 0.15$, and the DNS [46] has $Re_\lambda = 73$, $M_t = 0.14$. Solid line: DNS [46]. Dashed line: SVM-LES. Circles: HSVM-LES.

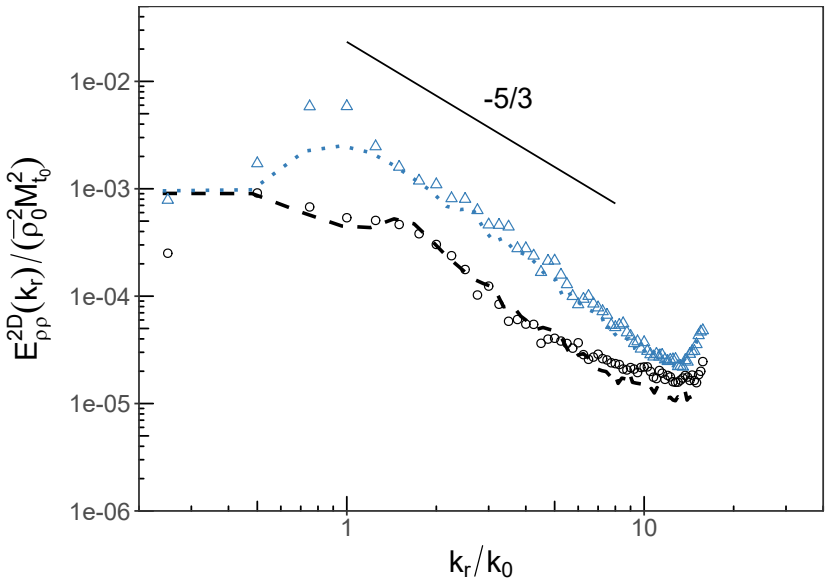

Figure 3.14: Radial spectra of density fluctuations in planes upstream and downstream of a $M_s = 1.5$ shock. The LES has $M_t = 0.15$ and $Re_\lambda = 300$ upstream of the shock. The upstream and downstream results are taken in planes located at $k_0x = -2$ and $k_0x = 7$, respectively. Circles: pre-shock SVM-LES. Triangles: post-shock SVM-LES. Dashed line: pre-shock HSVM-LES. Dotted line: post-shock HSVM-LES.

3.8 Discussion

We proposed a method for enforcing regularized LES solutions that fall off as $k^{-5/3}$ near the highest resolved wavenumbers, based on dynamic tuning of a modified

hyperviscous operator. The regularization is not directly physically motivated, but it is computationally inexpensive to perform and localized in both time and space. A constant is required for numerical stability, but the construction of the method suggests it should be insensitive to its selection. LES of forced isotropic turbulence at varying turbulent Mach number, mesh resolution, and values of the constant further indicate that refined empirical tuning of this constant is not necessary.

The regularization can function by itself, or as a correction to more complex SGS models. The stretched-vortex model has been applied successfully to previous LES of compressible turbulence and produces useful SGS statistics, but physical space implementations of this model often suffer from an erroneous high wavenumber pileup of kinetic energy. The compression of a shockwave results in this pileup being impulsively shifted out of the resolved wavenumbers, reducing the amplification in the subgrid kinetic energy predicted by the SGS model.

A Hybrid Stretched-Vortex Model (HSVM) is introduced that applies the dynamic regularization as an additional dissipative term to the stretched-vortex model. It is shown that the addition of the regularization substantially reduces the deviation from $k^{-5/3}$ scaling at high wavenumbers in forced turbulence, despite being a minor contribution to the total dissipation. The prediction of a $k^{-5/3}$ spectrum is specific to high-Re_λ homogeneous isotropic turbulence, but the hybrid model still shows reasonable agreement in comparisons with DNS of isotropic decaying turbulence even under lower Re_λ conditions where an inertial range is not expected.

Linear Interaction Analysis (LIA) is employed to provide a simplified representation of the flow downstream of a shockwave as it passes through an isotropic, turbulent upstream field. Application of LIA to 3D flow fields from HSVM-LES results in the SGS model predicting an increase in the kinetic energy at the unresolved scales that agrees well with the amplifications seen by simplified LIA of isotropic shell-summed spectra.

The periodic, anisotropic fields produced by application of LIA to DNS and LES of isotropic turbulence are allowed to decay in order to evaluate the performance of the hybrid stretched-vortex model in post shock fields. The HSVM-LES shows reasonable agreement with DNS with respect to both the initial post shock conditions and in the subsequent decay of the Reynolds stresses. Qualitative agreement is shown between these simulations and the DNS of isotropic turbulence passing through a shockwave performed by Larsson and Lele [45].

A limited number of LES with the shock explicitly simulated are presented to illustrate the effects of the regularization in a practical simulation. Even at a fine mesh resolution and using AMR, the standard stretched-vortex model observes no increase in the dissipation rate across the shock at low shock Mach numbers. The inclusion of the regularization improves the agreement of Reynolds stress amplifications when compared with DNS, and produces dissipation rates that more closely agree with the predictions of linear theory. Chapter 4 considers a more thorough analysis of the flow downstream of a shock in HSVM-LES, including a wider range of flow parameters.

Chapter 4

LES OF THE CANONICAL SHOCK-TURBULENCE PROBLEM: RESULTS

4.1 Introduction

The previous chapter, Chapter 3, builds off of the basic LES framework described in Chapter 2 and develops a procedure for HSVM-LES that is shown to improve the ability of the LES to capture the behavior of the flow in several test problems representing shock-turbulence interaction. This chapter considers the results of HSVM-LES of the canonical shock-turbulence problem, with a focus on analysis of the hydrodynamics of this problem at large Reynolds numbers which are beyond the reach of contemporary DNS. The LES leverages high mesh resolutions and extensive comparisons to DNS and LIA to ensure that the hydrodynamic behavior of these simulations is representative of physical flows.

Chapter 2 provides an overview of the filtered Navier-Stokes equations and the SGS model used in this study, and in this chapter these equations are solved numerically using the methodology discussed in sections 4.2 and 4.3. Section 4.5 summarizes the conducted LES, and evaluates the mesh sensitivity of the LES with comparisons to relevant DNS and LIA. Finally, section 4.6 discusses the physical results of the LES.

4.2 Governing equations and subgrid model

The governing equations of the LES are same as discussed in section 2.3. Likewise, in regions of the flow sufficiently far from the shock where the mesh is not refined the subgrid terms of the LES governing equations, (2.4), are modeled by the HSVM model (3.9).

4.2.1 SGS model near the shock

Subgrid-scale flow in a computational cell containing a shock is significantly different from the type of smooth turbulence that SGS models are typically constructed to represent. The SGS turbulence model becomes excessively dissipative near a shock, and so the SGS interaction model (3.9) is set to zero where WENO is active. Previous studies have found WENO alone to be sufficiently dissipative in this region [6].

The application of the SGS model in meshes refined by adaptive mesh refinement (AMR) near to but not directly on the shock remains a problem, because the cutoff wavenumber k_c in (2.10) is not clearly defined in regions of AMR. A convection model is introduced that assumes the unresolved kinetic energy is unchanged by the prolongation of the flow from the coarse mesh to the fine mesh in front of the shock, and tracks the motion of the SGS kinetic energy as the flow passes through the narrow band of AMR cells. The model is detailed in Appendix B, as the methodology is specific to this SGS model and flow geometry.

4.3 Numerical method

The box-turbulence simulations and shock-turbulence channel simulations are both run using the same fundamental numerical approach. The governing equations are implemented in the Adaptive Mesh Refinement in Object Oriented C++ (AMROC) framework [19] to provide mesh refinement and parallelization. Mesh refinement is flagged based on density contours, and is only active in the direct vicinity of the shock. The computational mesh spacing is uniform in all directions at all refinement levels, with equal refinement applied at the shock in the streamwise and transverse directions.

The non-linear convection terms of (2.4) are computed according to a conservative skew-symmetric formulation [9, 38] that provides implicit dealiasing. The flux solver is based on the scheme of Hill and Pullin [36], and switches between a 5th order, shock capturing, Weighted Essentially Non-Oscillatory (WENO) [53] method near the shock and a standard low cost, low dissipation 6th order accurate centered difference scheme away from the shock. The shock location is flagged using the approximate Riemann solver method of Lombardini [58]. The flagging threshold is set as the simulation runs by calculating the threshold that would flag 40% of the turbulent domain, and then that threshold is divided by a factor of 5 to capture only the sharpest features such as shocks. This approach limits the application of WENO to only a few cells in either direction of the shock without requiring case by case tuning, but at the shock WENO is typically applied in all three directions, rather than only the shock normal direction. WENO is also applied at the boundary between meshes at different AMR levels.

Despite employing a skew-symmetric formulation of the non-linear terms that reduces spurious contributions to the entropy field [38], it was found that over time the forced box-turbulence LES used for inlet conditions developed small but significant

entropic modes. The interaction of a shock is dependent not only on the amplitude of these modes but also on their orientation with respect to the vortical modes in the turbulence [64], and this complicates comparison to DNS and linear theory. Thus, a weak linear forcing on (2.4c) of the form $f = C_e(\overline{T} - \overline{T}_0)$ is introduced in the box-turbulence simulations , where C_e is tuned to control the entropic modes. This forcing is not included in the shock-turbulence simulations.

As a validation of the underlying forcing and numerical method, DNS simulations of Ryu and Livescu [76] are repeated in the numerical framework employed here. Figure 4.1 compares DNS to an equivalent simulation performed by Ryu and Livescu [76]. Both the DNS performed here and that performed by Ryu and Livescu [76] fully resolve turbulent scales in the upstream and downstream flow, with $k_{max}\eta > 1.5$, but the DNS of Ryu and Livescu [76] was shock-resolving, whereas the method used in this study uses a shock-capturing WENO scheme to stabilize the shock at a thickness on the order of the local mesh resolution. The shock-captured DNS closes agrees with the shock-resolved DNS regarding both the initial amplification of the Reynolds stress and the evolution of the Reynolds stress in the downstream flow, suggesting that the AMR employed is sufficient to separate the scales of the turbulence from the shock scales. The drop in the streamwise Reynolds stress in the shock-resolved DNS of Ryu and Livescu [76] near $k_0 x \approx 30$ is likely a result of boundary conditions associated with the outflow sponge zone, and the simulations in this study are performed in a longer domain to place this sponge zone further away from the region of interest downstream of the shock. The fluctuations in the streamwise Reynolds stress downstream of the shock are not from a lack of statistical convergence, and are observed in long-time averages of the flow.

4.4 Turbulence statistics

The supersonic background convection velocity in the box-turbulence simulations results in a small amount of spurious high wavenumber anisotropy in the upstream turbulence, produced from differing numerical errors in the streamwise and transverse directions. For analysis purposes, during post-processing we instead opt to calculate mean statistics, such as the Reynolds stresses, on a mesh restricted to half of the resolution of the coarsest mesh in the LES, and the SGS statistics discussed in section 2.4.1 are recomputed for this new coarser mesh. Reported dissipation rates are the exception to this, and are calculated on the computational mesh because they are considered representative of the numerical behavior of the LES.

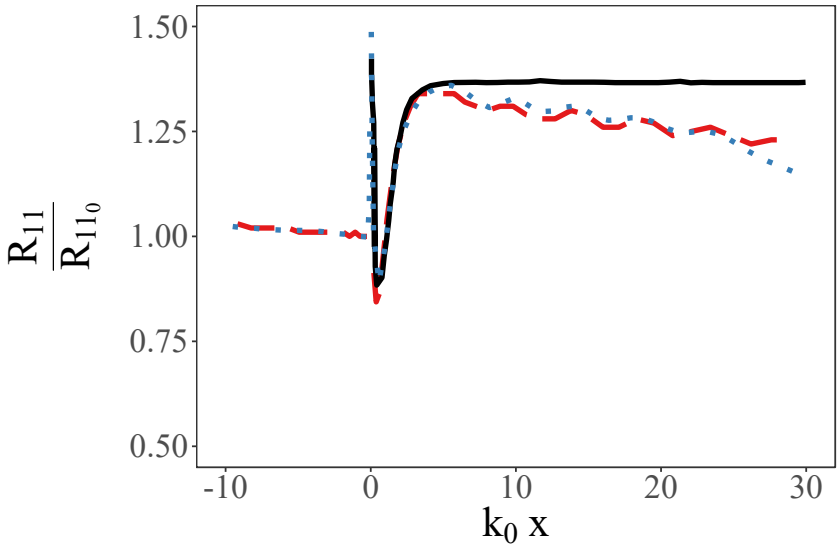

Figure 4.1: Evolution of the streamwise Reynolds stress downstream of a $M_s = 1.2$ shock, for upstream conditions of $M_t = 0.02$ and $Re_\lambda = 20$. Solid line: LIA. Dashed line: shock-captured DNS. Dotted line: shock-resolved DNS of Ryu and Livescu [76].

4.5 LES performed

4.5.1 Summary of simulations

Table 4.1 summarizes the LES simulations discussed in this study. Upstream quantities such as M_t and Re_λ contain contributions from the SGS model and thus are approximations. The computational grids are isotropic such that $\Delta x = \Delta y = \Delta z$, including within regions of AMR. The given meshes are on the coarsest level, such that the simulations with $N_x = 1024$, $N_y = 256$ and an AMR factor of 4× have an equivalent resolution of 4096×1024^2 in the direct vicinity of the shock where AMR is active. All simulations are run for a particle passage time across the length of the computational domain, and then statistics are recorded over a subsequent particle passage time or three large eddy turnover times in the upstream turbulence, whichever is longer. This is not sufficient to achieve full temporal convergence of large scale quantities, and some statistics such as the ratio of the streamwise to the transverse Reynolds stress, R_{11}/R_{tr}, are slightly perturbed from the value upstream of the shock that would occur with an infinite time average. Given finite computational resources, fine mesh resolutions and a broad parametric study are considered here to be more useful than long simulation times.

Resources are focused on simulations ranging between $M_s = 1.5$ and $M_s = 2.2$ because previous DNS observes interesting behavior in the post-shock Reynolds stress anisotropy within this regime. DNS has found that, for shocks weaker than $M_s \approx 1.5$, LIA predicts the post-shock Reynolds stress anisotropy reasonably well even at modest M_t, but for $M_s > 1.5$ DNS finds $R_{11}/R_{tr} > 1$ in the far-field post-shock flow and this ratio is approximately constant as M_s is further increased [46]. Conversely, for $M_s > 1.5$ LIA predicts that an increasingly large fraction of the turbulent kinetic energy is in the transverse Reynolds stress and by $M_s = 2.2$ predicts $R_{11}/R_{tr} < 1$ in the far-field of the post-shock flow. The discrepancy between LIA and DNS grows at larger M_s, but it is this transition that is of particular interest.

4.5.2 Mesh sensitivity

The two primary mesh parameters in the subject LES are the coarse mesh spacing and the local refinement level at the shock. Global refinement of the coarse mesh increases the fraction of the turbulent kinetic energy that is captured at the resolved scale and is expected to improve the LES results in smooth turbulent regions away from the shock. The local mesh refinement at the shock acts to reduce artificial dissipation from the shock capturing scheme, reduces spurious behavior in the entropy field generated by the shock-capturing scheme [49], and allows the shock curvature to be resolved [26, 49].

Test cases are performed to investigate the level of local refinement needed about the shock. The low-M_t case considered here is conservative with respect to mesh refinement requirements because as M_t is reduced for a given M_s, the shock corrugations become smaller and more difficult to resolve. Figure 4.2 shows the amplification of various statistics of interest through a $M_s = 1.5$ shock, plotted in the shock normal direction. The statistics are time averaged and spatially averaged in the transverse directions, and contain the contribution from the SGS stretched-vortex flow. The Reynolds stress and vorticity are normalized by linearly interpolating their upstream values to the mean shock position. The density-specific volume correlation $b = -\langle \rho' v' \rangle$, where $v = 1/\rho$, is normalized by the upstream turbulent Mach number as suggested by scaling in LIA. The density-specific volume correlation b is favored over $\langle \rho' \rho' \rangle$ because of its applications in incompressible mixing of variable density fluids [54, 79], but for the subject low M_t, single component flows $b \approx \langle \rho' \rho' \rangle / \langle \rho \rangle^2$. The SGS model does not provide an estimate for b at the subgrid scales, and this explains why b tends to be smaller in the LES than predicted by linear analysis. The contribution of the resolved scale flows to the vorticity is negligible at this mesh

M_s	M_t	Re_λ	L_x	x_s	k_0	N_x	$N_y \times N_z$	AMR
1.2	0.06	500	8π	$\pi/2$	4	512	128^2	4×
1.4	0.06	500	8π	$\pi/2$	4	512	128^2	4×
1.5	0.18	100	8π	$\pi/2$	4	1024	256^2	4×
1.5	0.18	500	8π	$\pi/2$	4	1024	256^2	4×
1.5	0.18	2500	8π	$\pi/2$	4	1024	256^2	4×
1.5	0.06	500	8π	$\pi/2$	4	1024	256^2	4×
1.5	0.06	20	8π	$\pi/2$	4	512	128^2	4×
1.5	0.06	70	8π	$\pi/2$	4	512	128^2	4×
1.5	0.06	95	8π	$\pi/2$	4	512	128^2	4×
1.5	0.06	130	8π	$\pi/2$	4	512	128^2	4×
1.5	0.06	180	8π	$\pi/2$	4	512	128^2	4×
1.5	0.06	500	8π	$\pi/2$	4	512	128^2	4×
1.5	0.14	75	3π	1.28	6	192	128^2	4×
1.5	0.06	500	3π	$\pi/2$	4	96	64^2	1×
1.5	0.06	500	3π	$\pi/2$	4	96	64^2	2×
1.5	0.06	500	3π	$\pi/2$	4	96	64^2	4×
1.5	0.06	500	3π	$\pi/2$	4	96	64^2	8×
1.5	0.14	75	3π	1.28	6	96	64^2	4×
1.6	0.06	500	8π	$\pi/2$	4	512	128^2	4×
1.8	0.06	500	8π	$\pi/2$	4	512	128^2	4×
2.0	0.12	500	8π	$\pi/2$	4	512	128^2	4×
2.0	0.06	500	8π	$\pi/2$	4	512	128^2	4×
2.0	0.03	500	8π	$\pi/2$	4	512	128^2	4×
2.0	0.03	500	8π	$\pi/2$	4	512	128^2	8×
2.2	0.18	100	8π	$\pi/2$	4	1024	256^2	4×
2.2	0.18	500	8π	$\pi/2$	4	1024	256^2	4×
2.2	0.06	500	8π	$\pi/2$	4	512	128^2	4×
2.2	0.06	500	3π	$\pi/2$	4	96	64^2	1×
2.2	0.06	500	3π	$\pi/2$	4	96	64^2	2×
2.2	0.06	500	3π	$\pi/2$	4	96	64^2	4×
2.2	0.06	500	3π	$\pi/2$	4	96	64^2	8×
2.6	0.06	500	8π	$\pi/2$	4	512	128^2	4×
3.0	0.06	500	8π	$\pi/2$	4	512	128^2	4×

Table 4.1: Summary of simulations. The conditions of the upstream turbulence, M_t and Re_λ, contain contributions from the model of the subgrid flows and are thus approximations. L_x is the length of the domain in the streamwise direction, x_s is the shock position, and k_0 is the wavenumber corresponding to the maximum in the energy spectrum of the upstream turbulence. N_x and N_y are the resolution of the coarsest mesh level in the streamwise and transverse directions, respectively. AMR gives the factor of refinement applied to the mesh near the shock.

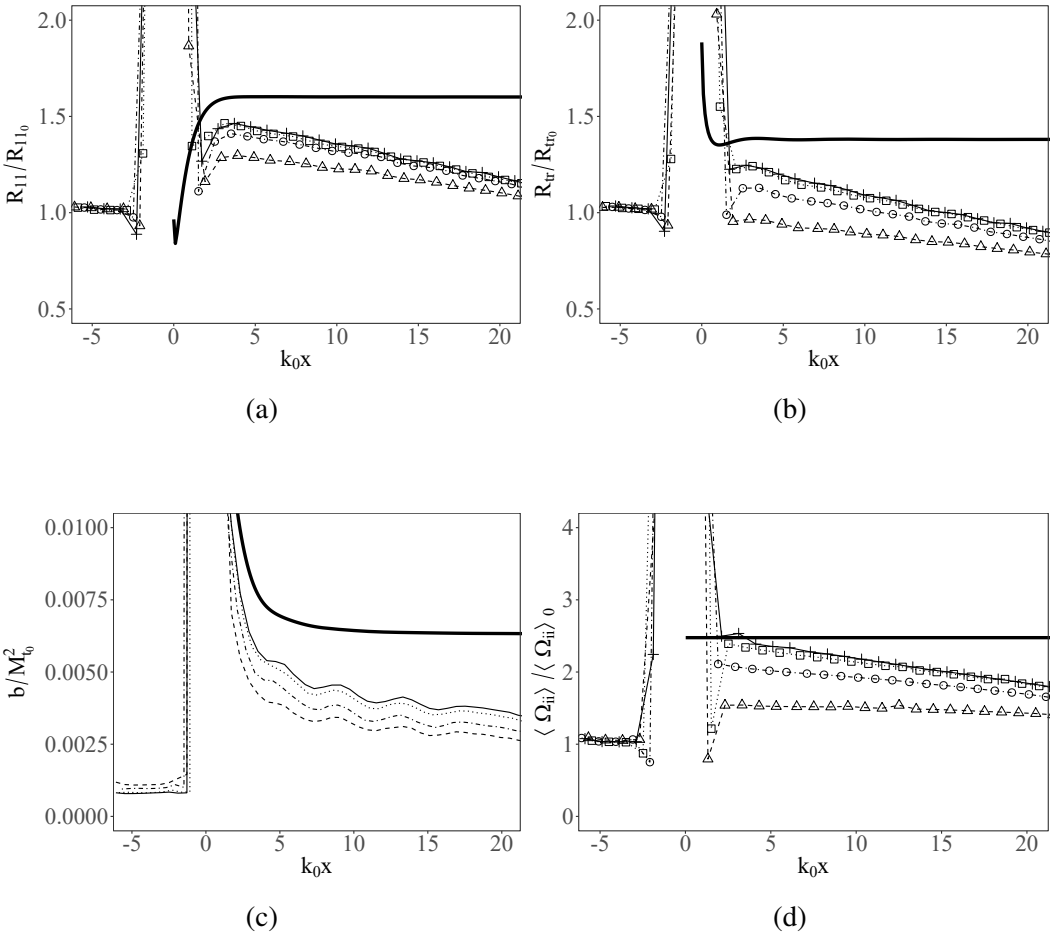

Figure 4.2: LES behavior for $M_s = 1.5, M_t = 0.06, Re_\lambda = 500$ on a $96 \times 64 \times 64$ base mesh with increasing local mesh refinement at the shock. Lines with symbols show the total statistics, including the contribution from the SGS model. (a) Streamwise Reynolds stress, (b) transverse Reynolds stress, (c) density-specific volume correlation $b = -\langle \rho' v' \rangle$, and (d) squared vorticity trace, $\Omega_{ii} = \omega_i \omega_i$. Dashed line ($\triangle$): uniform grid. Dot-dashed line ($\circ$): $2\times$ refinement. Dotted line ($\square$): $4\times$ refinement. Solid line ($+$): $8\times$ refinement. Thick solid line: LIA of (3.10).

resolution and Re_λ. The downstream oscillations in b, and to a lesser extent in the Reynolds stresses, are not an artifact of poor statistical convergence, and previous DNS have seen similar oscillatory behavior downstream of shocks at low M_t [76]. The SGS statistics behave in a nonphysical manner when calculated at the shock, resulting in the large spikes near the shock in Figure 4.2, but as discussed in section 4.2.1 these statistics are not used to calculated SGS terms in the governing equations in the direct vicinity of the shock. These LES are also performed for a $M_s = 2.2$ shock with similar results.

The streamwise Reynolds stress converges quickly, but the LES requires a factor of

4× AMR at the shock for the rest of the quantities to converge to an acceptable level. Garnier et al. [26] assert that numerical convergence requires the shock corrugation to be resolved, and this is evaluated in the LES by extracting a triangular mesh of the shock surface from the LES using the shock detection algorithm of Samtaney et al. [77]. The shock does not develop holes at the subject M_t and M_s, and thus the displacement of the triangularized shock mesh from its mean location can be converted into a continuous, periodic function on a rectangular 64×64 grid. The radial power spectrum of a 2D function $\psi(y, z)$ with Fourier transform $\hat{\psi}$ is defined as

$$E_{\psi}^{2D}(k_r) = \frac{1}{2} k_r \int_0^{2\pi} \left|\hat{\psi}(k_r, \theta_k)\right|^2 d\theta_k, \tag{4.1}$$

where k_r and θ_k are the radial and azimuthal wavenumbers. The time averaged, radial power spectra of the shock displacement is given in Figure 4.3, plotted against the prediction of LIA applied to (3.10) with $k_{c,LIA} = 1024$. LIA predicts that the shock displacements scale as a function of the energy spectrum as $E(k)/k^2$ [63], yielding an initially flat spectrum that transitions into a $k^{-11/3}$ slope. It may be of interest that $E(k)/k^2$ scaling behavior also appears in the spectrum of the velocity vector potential used in incompressible flows, but to the author's knowledge this is coincidental. The factor of $1/k^2$ that appears in the spectrum of shock corrugations is a result of scaling with the lengthscale of the upstream turbulence, as briefly discussed in section 1.2. The uniform-grid simulation significantly underestimates the curvature of the shock, but the LES exhibits a trend towards $k^{-11/3}$ behavior as AMR refines the mesh at the shock. The shock displacement and evolution of streamwise statistics both exhibit an acceptable degree of invariance with AMR level for refinement factors of at least 4×.

The LES approaches the results of LIA as the upstream M_t is reduced, as shown in Figure 4.4 for an $M_s = 2$ shock. The degree of agreement with LIA at $M_t = 0.03$ is comparable to that observed in shock-captured DNS under the similar flow conditions at $Re_\lambda \approx 30$ [85] , although the ability of the DNS to match LIA was limited by the low Re_λ simulated. Comparison to LIA requires low M_t and shock corrugations become smaller and harder to resolve as M_t is reduced. This would suggest that additional AMR should be required as M_t is reduced to a small value such as $M_t = 0.03$, but as shown in Figure 4.4 there is no substantial change in the LES when AMR refinement about the shock is increased in that case. Tian et al. [85] show that shock capturing in DNS is accurate when the ratio of the Kolmogorov scale to the numerical shock thickness is large, and the corresponding

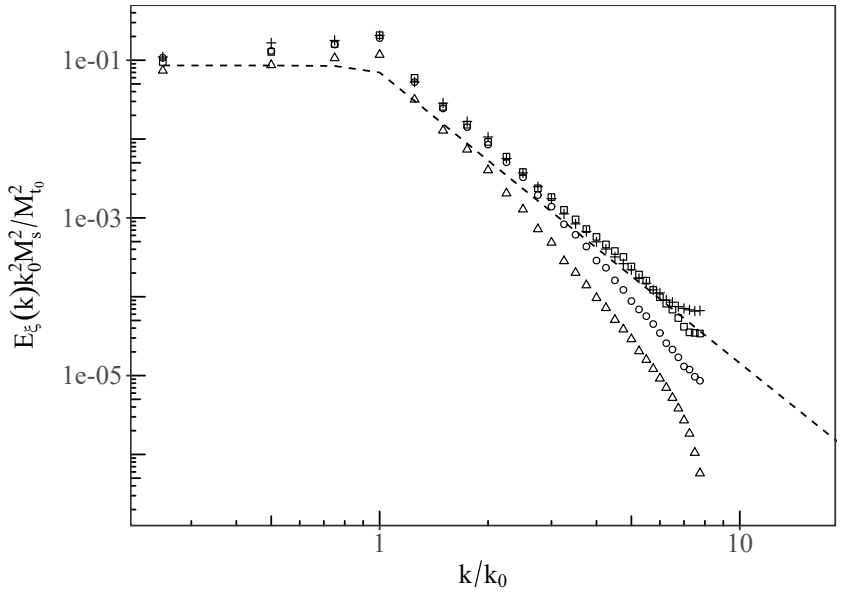

Figure 4.3: Time-averaged radial spectrum of shock displacement, for $M_s = 1.5$, $Re_\lambda \approx 500$, and $M_t \approx 0.06$ on a $96 \times 64 \times 64$ base mesh. The symbols show the results from LES with varying levels of AMR at the shock. (△): uniform grid. (○): 2× refinement. (□): 4× refinement. (+): 8× refinement. Dashed line: LIA of (3.10), which follows a $k^{-11/3}$ slope in the inertial range.

measure in LES would be a ratio of the lengthscale associated with the smallest resolved upstream eddies to the numerical shock thickness, δ_s. Assuming that the smallest upstream eddies are on the scale of the coarse mesh resolution, Δx_c, and the numerical shock is a few cells wide on the refined mesh, this will be a fixed ratio that is only dependent on the shock capturing scheme and the mesh. This ratio is approximately $\Delta x_c/\delta_s \approx 1.8$ in the LES with 4× AMR, where δ_s is taken as the mean velocity difference across the shock divided by the maximum of $|\partial\tilde{u}_1/\partial x|$, and is similar to the requirement $\eta/\delta_s > 1.4$ found by Tian et al. [85] . The tendency of low M_t cases to not depend heavily on AMR suggests that the ratio of $\Delta x_c/\delta_s$ may be a more practical requirement on mesh refinement but, except at extremely low M_t, this requirement appears to be met under conditions similar to those required to resolve shock corrugations.

4.5.3 Comparison to DNS

DNS is available for validation of the LES at moderate Re_λ. Figure 4.5 shows the subject LES compared against the $M_s = 1.5$ shock-captured DNS of Larsson et al. [46] for upstream inlet conditions of $M_t = 0.16$, $Re_\lambda = 75$, and $k_0 = 6$. The method used to construct turbulence at the inflow boundary upstream of the shock

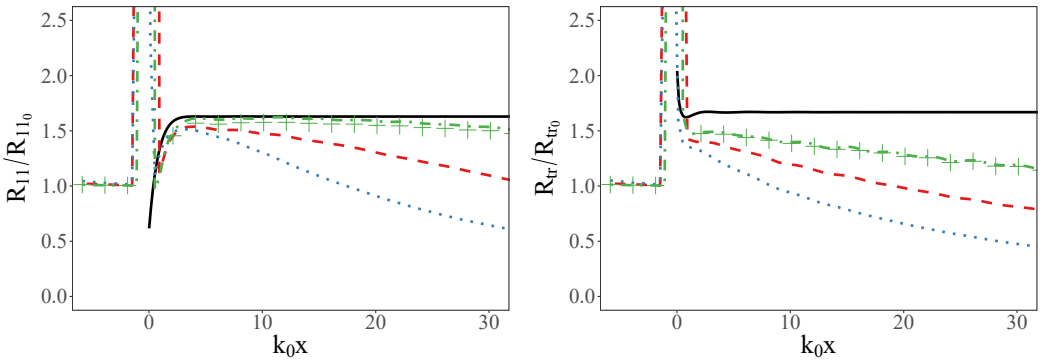

(a) (b)

Figure 4.4: Streamwise (a) and transverse (b) Reynolds stresses averaged over time and cross sectional planes for a $M_s = 2.0$ shock and upstream $Re_\lambda \approx 500$ on a $512 \times 128 \times 128$ base mesh. Solid line: LIA. Dotted line: $M_t = 0.12$ and $\times 4$ AMR. Dashed line: $M_t = 0.06$ and $\times 4$ AMR. Dot-dashed line: $M_t = 0.03$ and $\times 4$ AMR. Pluses: $M_t = 0.03$ and $\times 8$ AMR.

was different in the DNS and the peak wavenumber is not as well defined as it is in the LES, yielding some difference in the spatial nondimensionalization of the simulations. The LES of primary interest in this study are performed at higher $Re_\lambda \geq 100$, but those LES still resolve a comparable fraction of the turbulent kinetic energy relative to this case. The higher resolution LES appears to underestimate kinetic energy dissipation upstream of the shock relative to the DNS when including the contribution from the subgrid continuation, but the behavior of the resolved scales in the LES at both mesh resolutions are consistent. The subgrid continuation assumes an inertial range, and thus becomes less reliable when the mesh cutoff in the LES is in the viscous scales of the turbulence, particularly at low Reynolds numbers. The agreement of the LES with the DNS is considered reasonable at both mesh resolutions and changes with mesh resolution at the coarsest level are found to be minimal under the resolutions and flow conditions of primary interest in this study, as shown in Figure 4.6.

A number of additional comparisons of the HSVM-LES to DNS in the canonical shock-turbulence problem and several simplified test problems may also be found in Braun et al. [11].

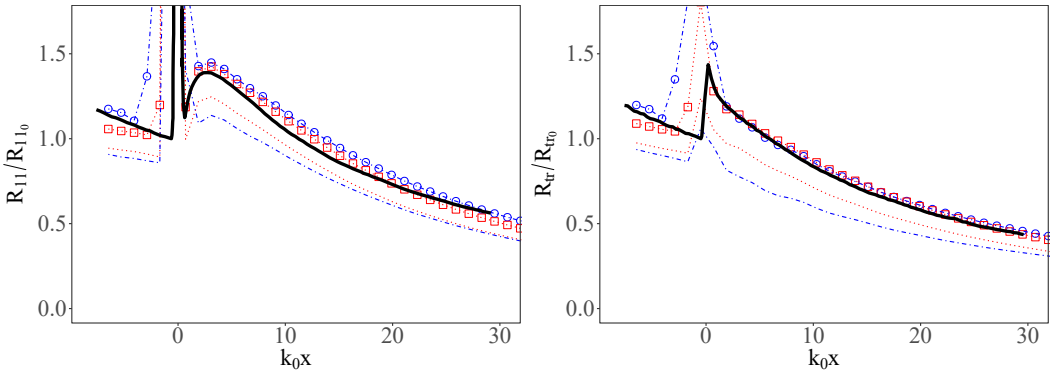

(a) (b)

Figure 4.5: Streamwise (a) and transverse (b) Reynolds stresses averaged over time and cross sectional planes for a $M_s = 1.5$ shock. Inlet conditions are $M_t = 0.16$, $Re_\lambda = 75$, and $k_0 = 6$. The lines show the resolved scale statistics and the symbols show the total statistics, including the contribution from the SGS model. The LES have a factor of 4× AMR at the shock, and are normalized by their total upstream value interpolated to the mean shock position. Dotted line (□): LES with a $192 \times 128 \times 128$ base grid. Dash-dotted line (○): LES with a $96 \times 64 \times 64$ base grid. Thick solid line: shock-captured DNS of Larsson et al. [46] [data from 35].

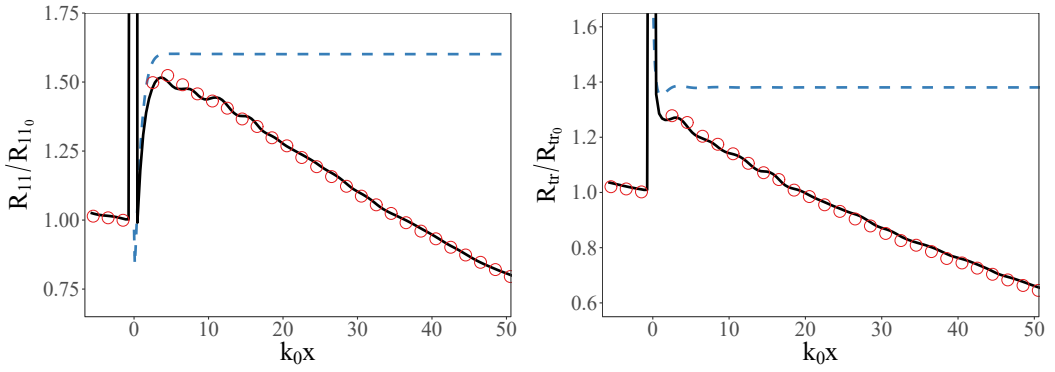

(a) (b)

Figure 4.6: Streamwise (a) and transverse (b) Reynolds stresses averaged over time and cross sectional planes for a $M_s = 1.5$ shock, with upstream conditions of $M_t = 0.06$ and $Re_\lambda = 500$. LES are conducted with a factor of 4× AMR at the shock, and results include the contribution from the SGS model. Solid line: LES with $1024 \times 256 \times 256$ coarse mesh. Circles: LES with $512 \times 128 \times 128$ coarse mesh. Dashed line: LIA of (3.10).

4.6 Results and discussion

4.6.1 Shock Mach number effects

The shock's effect on the turbulent statistics is strongly Mach number dependent. Previous DNS has seen only limited Reynolds number dependency on the Reynolds stress amplification over the shock [46], suggesting that the LES should still agree reasonably well with low Reynolds number DNS regarding this phenomena. Figure 4.7 compares the Reynolds stress amplifications from the LES with those seen in $Re_\lambda = 20$ DNS [76] and LIA. The LIA results show the ratio of the Reynolds stresses far downstream of the shock to their pre-shock state. The post-shock values from the DNS and LES are taken at the position of the maximum streamwise Reynolds stress which occurs in the LES at $k_0 x \approx 3$. The upstream turbulent Mach number in the DNS varies between 0.05 and 0.12, and this variation is likely responsible for the lower transverse Reynolds stress amplification in the $M_s = 2.2$ DNS. Ryu and Livescu [76] observed that DNS trended towards the results of LIA as M_t was reduced, but the lowest M_t DNS run still does not identically reproduce the predictions of LIA. The scatter in the Reynolds stress amplifications results from a lack of complete statistical convergence due to the limited number of large eddy turnover times completed over the duration of the LES. The LES agrees well with the streamwise Reynolds stress amplifications predicted by LIA. The transverse Reynolds stress amplifications are lower in LES than in LIA, but the LES still agree reasonably well with the DNS, with Reynolds stress amplifications within 8% of those from the DNS despite differences in flow conditions.

The LES dissipation rate and the vorticity are compared to LIA in Figure 4.8. The dissipation rate amplification in LIA is approximated by the predicted amplification in $\langle T \rangle^{0.76} \langle \Omega_{ii} \rangle / \langle \rho \rangle$, as the LIA analysis does not explicitly consider viscosity. The LES results are sampled immediately downstream of the shock, and small differences in the position where data are taken, as well as minor differences in the application of AMR and WENO between runs, introduce a small amount of scattering in the LES results. LIA predicts that only the transverse components of the vorticity are amplified, whereas the vorticity in the SGS flows in the LES remains nearly isotropic. At the subject Reynolds numbers the downstream vorticity field is expected to return to isotropy very quickly [46], and so this is not considered an important discrepancy.

DNS has observed vorticity amplifications that converge towards LIA more quickly than the Reynolds stresses as M_t is reduced [76]. The LES and LIA amplifications in the vorticity and dissipation agree reasonably well for $M_s \leq 2.2$, with differences

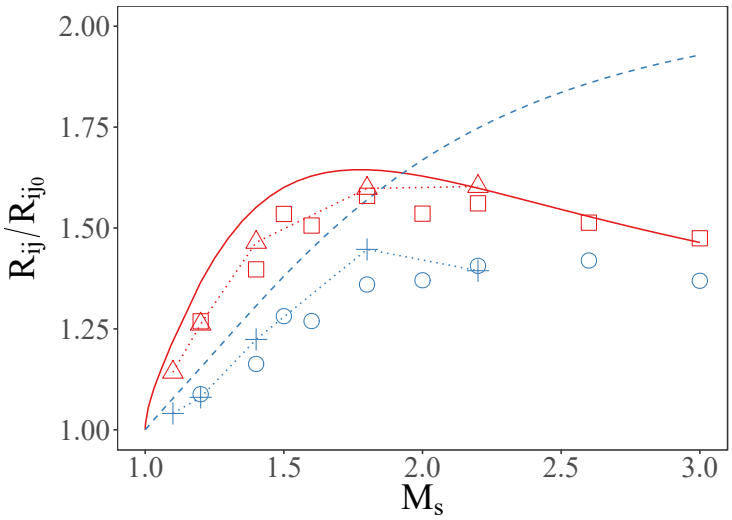

Figure 4.7: Streamwise and transverse Reynolds stress amplifications over a shock. LES has upstream flow conditions of $M_t \approx 0.06$ and $Re_\lambda \approx 500$, and is on a $512 \times 128 \times 128$ coarse mesh with $4\times$ AMR. The DNS was performed by Ryu and Livescu [76] at $Re_\lambda = 20$ with M_t ranging between $0.05 - 0.12$ immediately upstream of the shock. Post shock values are taken at the position of the maximum post-shock streamwise Reynolds stress and include contributions from the SGS model. Streamwise Reynolds stress amplifications are given by the squares (LES), triangles (DNS), and solid line (LIA). Transverse Reynolds stress amplifications are the circles (LES), pluses (DNS), and dashed line (LIA).

between the methods being less than 15%, but at higher shock Mach numbers the post shock dissipation rate appears to be consistently lower than LIA. The amplification in these quantities is expected to be difficult to capture in LES, because they are inherently high-wavenumber phenomena which are almost entirely modeled by the SGS model for the subject flow conditions. The rapid change in lengthscales across the shock, subject to a fixed cutoff wavenumber in the LES, suggests that LES may have difficulty modeling these small scale phenomena at large M_s. Comparisons between LES and LIA are comparisons of two different models, neither of which represents an exact solution, but subsequent LES are primarily focused on conditions with $M_s \leq 2.2$ where the LES shows better agreement with LIA.

4.6.2 Reynolds number effects

The peak streamwise Reynolds stress downstream of the shock has been observed to decrease when computed in DNS with Reynolds number increasing from $Re_\lambda = 40$ to $Re_\lambda = 70$, although the change was very small [46]. Higher peak Reynolds stresses are observed at higher Reynolds numbers over the range of $Re_\lambda = 10 - 45$

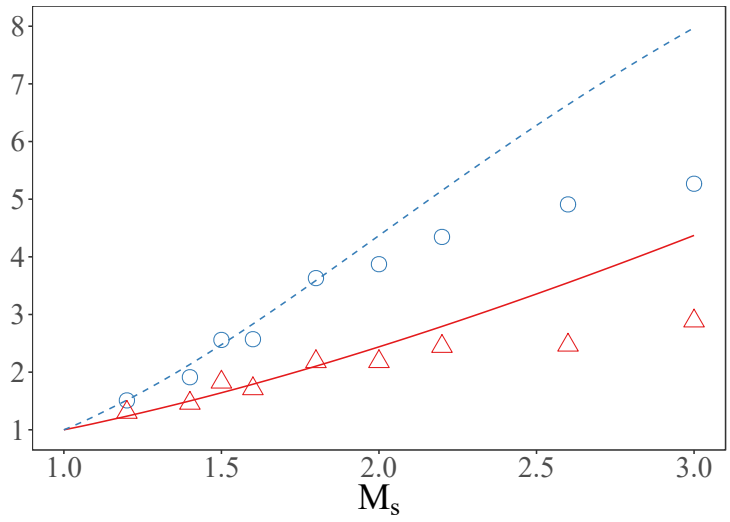

Figure 4.8: Squared vorticity trace $\Omega_{ii} = \omega_i\omega_i$ and kinetic energy dissipation rate immediately downstream of the shock, normalized by their upstream value. The LES conditions are the same as in figure 4.7. The LIA amplification in dissipation rate is approximated by the amplification in $\langle\mu\rangle\langle\Omega_{ii}\rangle/\langle\rho\rangle$. Vorticity amplifications $\langle\Omega_{ii}\rangle/\langle\Omega_{ii}\rangle_0$ are the circles (LES) and dashed line (LIA). Dissipation rate amplifications are given by the triangles (LES) and solid line (LIA).

[76], but, likewise, the magnitude of the Reynolds number effects was limited.

The streamwise Reynolds stress amplifications from the LES at $M_s = 1.5$ are plotted in Figure 4.9a over the range of $Re_\lambda = 20 - 2500$. The results agree with the DNS in that there is initially a small increase in the amplification of R_{11} with increasing Re_λ over the range $Re_\lambda = 20 - 40$, and there is a minor decrease between the $Re_\lambda = 40$ and $Re_\lambda = 70$ cases. At $Re_\lambda > 100$ there is no discernible effect of Reynolds number, consistent with the transition to fully developed turbulence observed in many flow geometries near that Reynolds number [20]. The decrease in the amplification of R_{11} over the range of $Re_\lambda = 40 - 100$, followed by a leveling off with no further Reynolds number effects, agrees qualitatively with the $M_s = 1.05$ experiments of Kitamura et al. [42], although the amplitude of the observed changes was much larger in that study.

The simulations in Figure 4.9a are conducted under conditions that range from DNS, at $Re_\lambda = 20$, to LES with almost no resolved viscosity at $Re_\lambda = 2500$. Figure 4.9b shows the fraction of the streamwise Reynolds stress that is contained at the subgrid level in the simulations, measured at the location of the peak in the downstream R_{11}. The downstream values are used instead of the upstream conditions because a greater fraction of the kinetic energy is held in the subgrid scales downstream of the

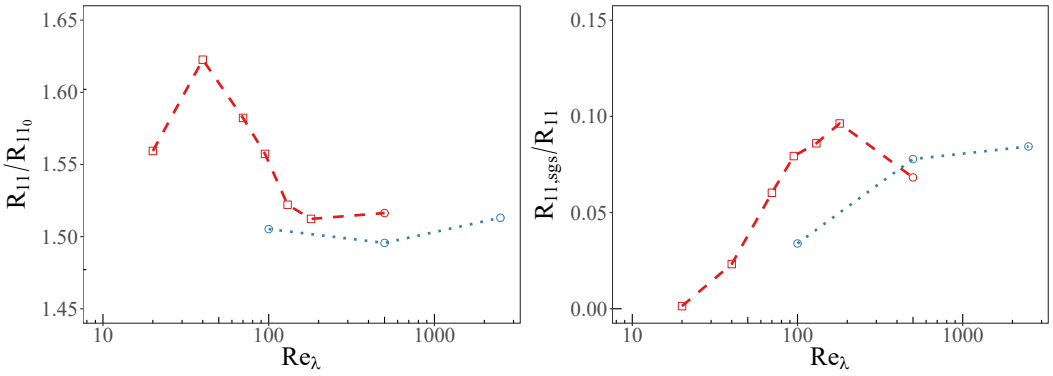

(a) Streamwise Reynolds stress

(b) Subgrid scale energy

Figure 4.9: Amplification in the streamwise Reynolds stress over a $M_s = 1.5$ shock, and the fraction of that Reynolds stress held in the subgrid scales downstream of the shock. Downstream quantities are sampled at the position of the peak streamwise Reynolds stress. The dashed line has an upstream $M_t \approx 0.06$ and the dotted line has $M_t \approx 0.18$. The squares are LES done on a $512 \times 128 \times 128$ coarse mesh and the circles are done on a $1024 \times 256 \times 256$ coarse mesh. Both meshes use 4× AMR.

shock. The changes in the LES at various Re_λ do not appear to be directly correlated with the fraction of the kinetic energy that is resolved on the computational mesh, suggesting that these trends are not merely a result of numerical resolution.

4.6.3 Density fluctuations

Figure 4.10 shows radial spectra of density fluctuations and co-spectra of velocity-density fluctuations in the LES. Density fluctuations upstream of the shock are driven by the low turbulent Mach number and are considerably smaller than the fluctuations generated by the shock. There is an increase in the spectra near the mesh cutoff wavenumber resulting from aliasing errors, but both spectra display a $k^{-5/3}$ slope in the inertial range.

The downstream density fluctuations arise from a mix of acoustic and entropy modes generated by the shock. LIA predicts that at low M_s acoustic modes account for most density fluctuations, but for $M_s > 1.65$ the entropy modes become dominant [49], at which time the entropy modes grow rapidly with M_s. This behavior may be observed in the LES, as shown in Figure 4.11. The density fluctuations initially remain approximately constant with M_s and contain a region of rapid, smooth decay near the shock resulting from the relaxation of exponentially decaying pressure modes. At higher $M_s \geq 2.2$, the density amplification begins to grow significantly and the LES reproduces the transition from a smoothly decaying profile to a sharp jump,

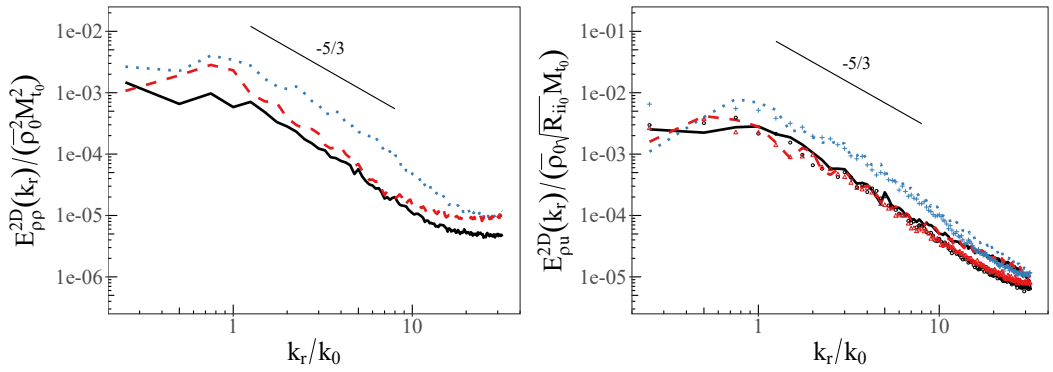

(a) (b)

Figure 4.10: Radial power spectra of density fluctuations (a) and co-spectra of density-velocity fluctuations (b) for a $M_s = 1.5$ shock, with upstream conditions of $M_t \approx 0.18$ and $Re_\lambda \approx 500$ on a $1024 \times 256 \times 256$ base grid with 4× AMR. In (b), the lines show the co-spectrum of $\overline{\rho}\tilde{u}_1$, and the symbols show the co-spectrum of $\overline{\rho}\tilde{u}_2$. Solid line (∘): $k_0 x = -1.34$. Dotted line (+): $k_0 x = 5.57$. Dashed line (△): $k_0 x = 28.3$.

consistent with the transition to a regime where exponentially decaying pressure modes are comparatively small relative to entropy fluctuations. Velocity dilatation appears in the transport equations for a_i and b [56], and drives behavior such as the dissipation of b, $\varepsilon_b = \overline{v' \partial u_k'/\partial x_k}$, [79]. In incompressible variable-density turbulence these correlations are the result of dilatation produced by molecular mixing of different densities of fluid and, despite weak compressibility effects at the subject M_t, this appears to still be the case in the LES. The correlation $\overline{v' \partial u_k'/\partial x_k}$ calculated at scales that are well resolved in the LES is small compared to the observed ε_b, which is the result of subgrid mixing modeled by (3.9).

Figure 4.12 shows the mass-weighted velocity fluctuations $a_i = \langle \rho' u_i' \rangle / \langle \overline{\rho} \rangle$ downstream of the shock. This term represents the turbulent mass flux and, along with $b = -\langle \rho' v' \rangle$, is a correlation that is tracked in some Reynolds-Averaged Navier Stokes (RANS) models [e.g. 80]. Unlike the Reynolds stresses, which have not consistently displayed a return to isotropy within the limited domains possible in numerical studies [45, 46], a_i appears to return to the isotropic state $a_i = 0$ downstream of the shock, although it does so slowly in the low M_t cases. Capturing the behavior of measures such as a_1 and b is important in simulations of shock-turbulence interactions, and the production of these statistics by the shock in the LES agrees reasonably well with the predictions of LIA.

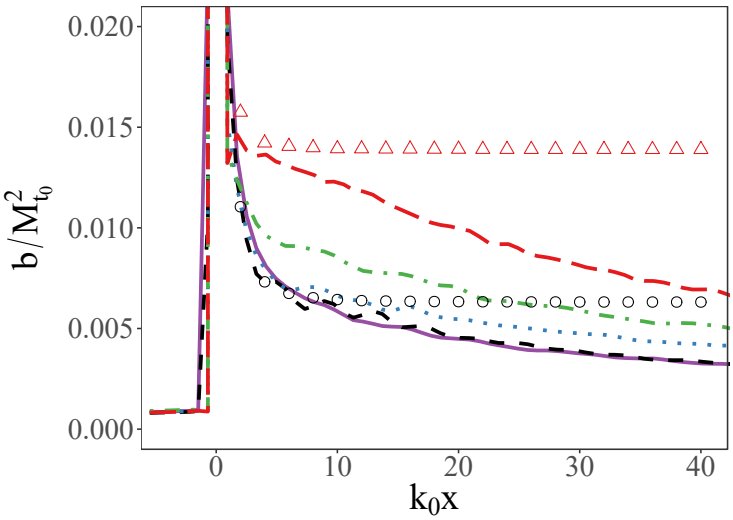

Figure 4.11: Averaged density-specific volume correlation $b = -\langle \rho' v' \rangle$ in LES with upstream $M_t \approx 0.06$ and $Re_\lambda \approx 500$ on a $512 \times 128 \times 128$ base grid with 4× AMR. Solid line: $M_s = 1.2$. Dashed line: $M_s = 1.5$. Dotted line: $M_s = 2$. Dash-dotted line: $M_s = 2.2$. Long-dashed line: $M_s = 2.6$. The circle and triangle symbols show LIA of (3.10) at $M_s = 1.5$ and $M_s = 2.6$, respectively

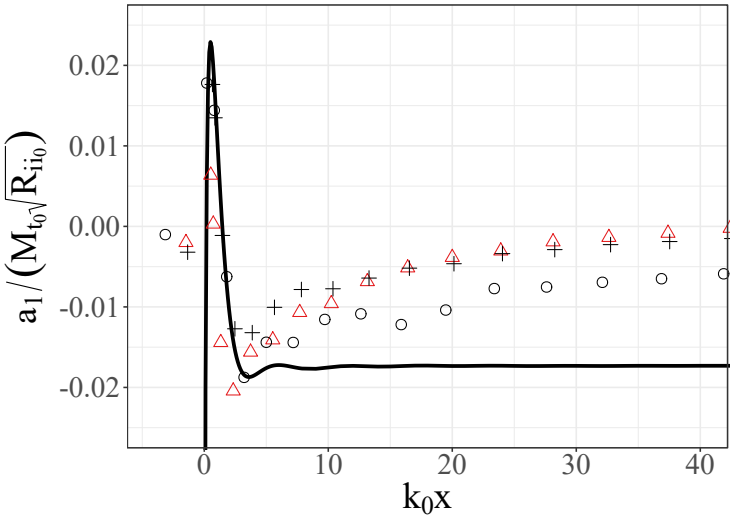

Figure 4.12: Averaged mass-weighted velocity fluctuations $a_i = \langle \rho' u_i' \rangle / \langle \overline{\rho} \rangle$. The LES is shown by the symbols and has upstream $Re_\lambda \approx 500$ on a $1024 \times 256 \times 256$ base grid with 4× AMR. Solid line: $M_s = 1.5$ LIA of (3.10). Circles : $M_s = 1.5$, $M_t = 0.06$. Pluses: $M_s = 1.5$, $M_t = 0.18$. Triangles: $M_s = 2.2$, $M_t = 0.18$.

4.6.4 Post shock anisotropy

DNS have found that the Reynolds stresses do not quickly return to isotropy, whereas the vorticity field rapidly relaxes to an isotropic state [45, 46]. The LES agrees with this, and even at high Reynolds number there is no apparent trend in the Reynolds stresses in the LES that would indicate a return to isotropy. All components of the SGS vorticity in the LES are amplified by the shock, whereas LIA predicts that only the transverse components of vorticity are amplified, but this not considered to be a significant shortcoming of the model because of the quick post-shock return to isotropy of vorticity in DNS. The SGS Reynolds stresses, which numerically govern the interaction of the SGS and resolved scales of the flow in (3.9), take longer to return to isotropy, and the HSVM-LES is capable of capturing the initial post-shock anisotropy of the Reynolds stresses at the SGS scales relatively well relative to the predictions of LIA [11].

An alternative method for considering the anisotropy of the Reynolds stress is to consider the invariants of the Reynolds stress anisotropy tensor,

$$b_{ij} = \frac{R_{ij}}{R_{ii}} - \frac{\delta_{ij}}{3}, \tag{4.2}$$

which are defined here as [69]

$$\eta_l^2 = \frac{b_{ij}b_{ji}}{6}, \tag{4.3a}$$

$$\xi_l^3 = \frac{b_{ij}b_{jk}b_{ki}}{6}. \tag{4.3b}$$

Any anisotropy in the Reynolds stresses can be represented as a single point on the $\eta_l - \xi_l$ plane. This approach is often used to simplify the description of Reynolds stress anisotropy in problems where R_{ij} has six independent components, although in the present case only the diagonal components of R_{ij} are non-zero. The realizable limits of η_l and ξ_l that correspond to real-valued velocities are roughly triangular, and this boundary is referred to as the Lumley triangle [61]. Figures 4.13 and 4.14 show the evolution of the Reynolds stress anisotropy downstream of a shock in the $\xi_l - \eta_l$ space for representative cases. At higher M_s, the flow initially has $R_{11} < R_{tr}$ shortly downstream of the shock, leading to $\xi_l < 0$, but quickly relaxes to $\xi_l > 0$ with $R_{11} > R_{tr}$ as the flow progresses downstream. The growth and decay of the downstream anisotropy occurs mostly near the $\xi_l > 0$ limit of the Lumley triangle,

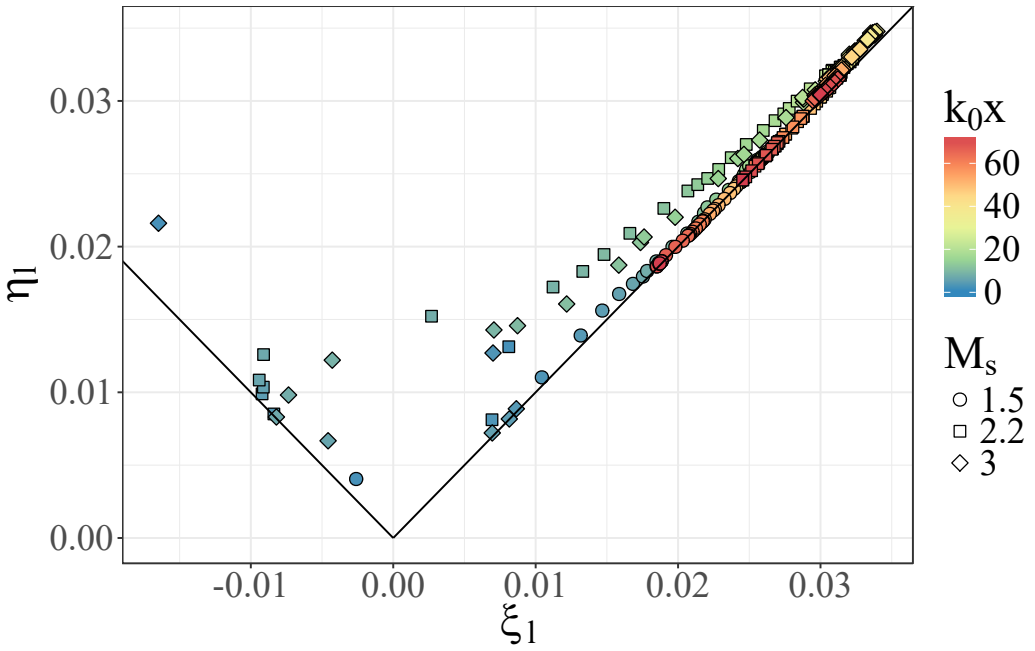

Figure 4.13: Evolution of post-shock Reynolds stress anisotropy in the plane of the b_{ij} tensor invariants ξ_l and η_l. The upstream flow has $M_t = 0.06$ and $Re_\lambda \approx 500$, and are performed in LES on a $512 \times 128 \times 128$ mesh with 4× AMR. The symbols show the LES results, and are colored by their streamwise position downstream of the shock. The lines show the boundaries of the Lumley triangle, corresponding to the domain of realizable flow conditions.

particularly at higher M_t, which is expected because the left and right boundaries of the Lumley triangle correspond to axisymmetric flow. The tendency of the flow to relax towards isotropy along the $\xi_l > 0$ boundary of the Lumley triangle is also observed in return-to-isotropy models and experimental data for homogeneous turbulence [15, 78]. The flow progresses towards the $\xi_l = \eta_l = 0$ isotropic state for a limited duration downstream of the shock, but it does not relax to isotropy within the domains available in the computations.

Transverse spectra

The averaged Reynolds stresses and vorticity are aggregate quantities that only provide information on the largest and smallest scales in the flow, and say little about the behavior of the intermediate scales within the inertial range of the turbulence. The radial spectra of the streamwise and transverse velocities upstream and downstream of a $M_s = 2.2$ shock are shown in Figure 4.15, and these spectra provide insight into how kinetic energy is distributed at all scales in the flow. The modest drop-off in

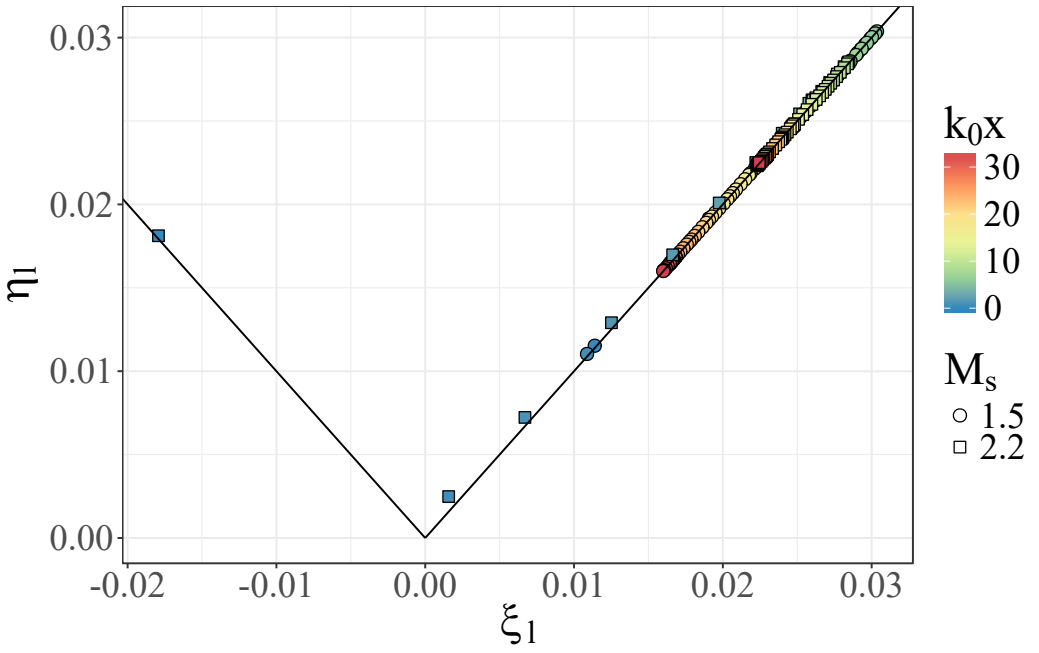

Figure 4.14: Evolution of post-shock Reynolds stress anisotropy in the plane of the b_{ij} tensor invariants ξ_l and η_l. The upstream flow has $M_t = 0.18$ and $Re_\lambda \approx 500$, and are performed in LES on a $1024 \times 256 \times 256$ mesh with 4× AMR. The symbols show the LES results, and are colored by their streamwise position downstream of the shock. The lines show the boundaries of the Lumley triangle, corresponding to the domain of realizable flow conditions.

the spectra near the coarse mesh cutoff wavenumber is, in part, a physical artifact of using 2D spectra, as will be subsequently discussed.

Taking ratios of these radial spectra, one can define an anisotropy parameter as a function of wavenumber [14, 56],

$$\chi^{2D} = \frac{E_{11}^{2D}}{E_{11}^{2D} + E_{22}^{2D} + E_{33}^{2D}} - \frac{1}{3}. \tag{4.4}$$

If the spectra in (4.4) were taken in 3D, then clearly $\chi = 0$ for all wavenumbers in an isotropic field. Computing χ with radial spectra, as done here, will generally return $\chi^{2D} \neq 0$ even if the flow is isotropic. A given wavenumber in a one-dimensional spectrum contains contributions from larger magnitude three-dimensional wavenumbers [69], and the same phenomena occurs in radial spectra. Taking the definition of the radial power spectrum tensor, with $k_2 = k_r \cos(\theta)$ and $k_3 = k_r \sin(\theta)$,

$$E_{ij}^{2D}(k_r) = \frac{k_r}{2} \int_0^\infty \int_0^{2\pi} \phi_{ij} d\theta dk_1, \tag{4.5}$$

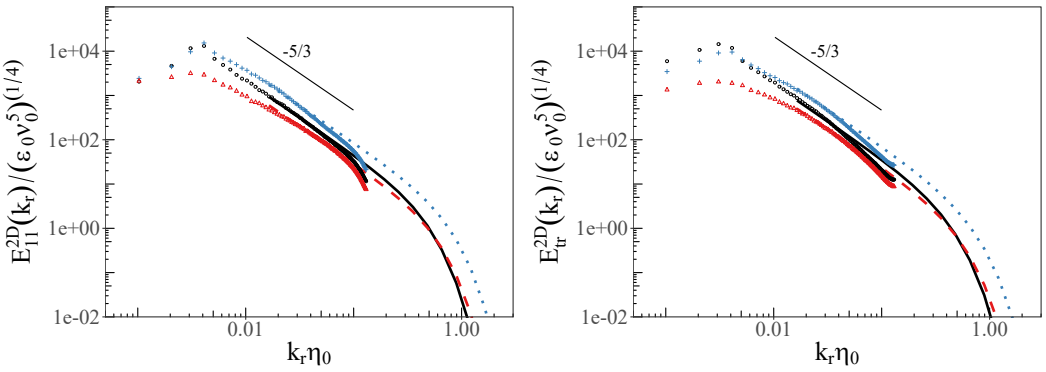

(a) Streamwise velocity spectra (b) Transverse velocity spectra

Figure 4.15: Time averaged radial velocity spectra about a $M_s = 2.2$ shock, for upstream conditions of $M_t \approx 0.18$ and $Re_\lambda \approx 500$ on a $1024 \times 256 \times 256$ base grid with 4× AMR. The symbols show the resolved spectra in planes located at $k_0x = -1.47(\circ)$, $k_0x = 5.52(+)$, $k_0x = 28.1(\triangle)$. The averaged spectra of the modeled subgrid flows at each plane are given by the solid, dotted, and dashed lines, respectively, and these are extended into the resolved scales to show agreement with the resolved spectra.

and the isotropic velocity spectrum tensor for $k = \sqrt{k_1^2 + k_2^2 + k_3^2}$,

$$\phi_{ij}(k) = \frac{E(k)}{4\pi k^2}\left(\delta_{ij} - \frac{k_i k_j}{k^2}\right), \tag{4.6}$$

one obtains expressions for the radial spectra of streamwise and transverse velocities components,

$$E_{11}^{2D}(k_r) = \frac{k_r}{4}\int_0^\infty \frac{E(k)}{\left(k_1^2 + k_r^2\right)}\left(1 - \frac{k_1^2}{k_1^2 + k_r^2}\right)dk_1, \tag{4.7a}$$

$$\frac{E_{22}^{2D}(k_r) + E_{33}^{2D}(k_r)}{2} = \frac{k_r}{8}\int_0^\infty \frac{E(k)}{\left(k_1^2 + k_r^2\right)}\left(2 - \frac{k_r^2}{k_1^2 + k_r^2}\right)dk_1. \tag{4.7b}$$

Evaluating (4.7) with $E(k) = k^{-5/3}$ yields a constant value of $\chi^{2D} = 1/33$, illustrating that the 2D anisotropy parameter will be slightly perturbed from zero in isotropic turbulence. In the case of a finite spectrum, such as (3.10), the effects are more pronounced. Figure 4.16 shows the anisotropy parameter calculated in the isotropic turbulence in front of the shock. An analytical result for the model isotropic spectra (3.10) with $k_{c,LIA} = 128$ is constructed by performing the same decomposition into vorticity modes used in LIA, and binning the resulting modes by radial wavenumber.

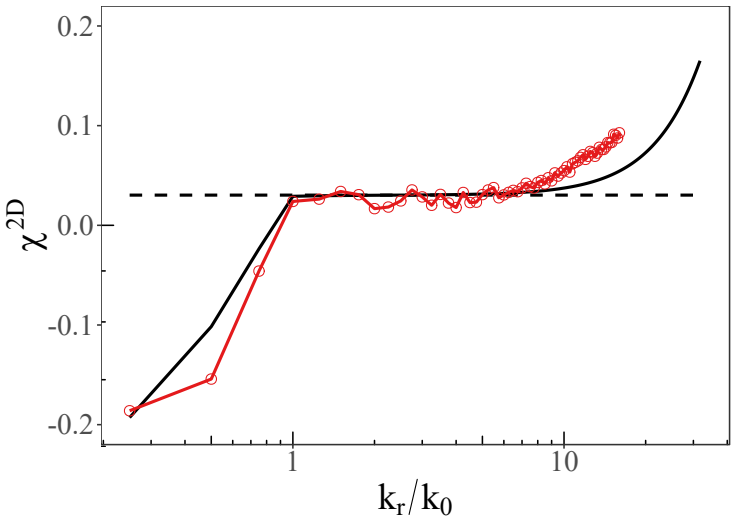

Figure 4.16: Time averaged anisotropy parameter in isotropic upstream turbulence upstream of a $M_s = 1.5$ shock, with $M_t \approx 0.18$ and $Re_\lambda \approx 500$ on a $1024\times256\times256$ base grid. The solid line shows χ^{2D} calculated under the assumption of isotropy using the model spectrum (3.10), and the dashed line is the result for an infinite $k^{-5/3}$ spectrum. The circles are the LES, given at a plane located at $k_0 x = -2$, just upstream of the mean shock position shock.

The cutoff in the model spectrum results in an abrupt rise in χ^{2D} at high wavenumbers, which is an artifact of high 3D-wavenumber transverse modes being aliased onto low 2D-wavenumbers in the radial spectra when the modes are sampled in a 2D plane. The LES results are thus truncated at $k \leq k_{max}/2$ to focus on the inertial range, as χ^{2D} is not considered a useful analysis tool at the largest wavenumbers.

Figure 4.17 plots χ^{2D} computed in cross sectional planes at various streamwise locations downstream of a $M_s = 1.5$ and a $M_s = 2.2$ shock. After some transience close to the shock, the LES shows nearly uniform value in the anisotropy parameter with radial wavenumber over the inertial range. χ^{2D} appears to return to isotropy over the extent of the inertial range as the flow evolves downstream, with higher radial wavenumber becoming isotropic more quickly. The exception to this is a small number of modes near and below k_0 which do not return to a profile similar to the isotropic upstream flow, and the $M_s = 2.2$ case initially sees an increase in χ^{2D} at these low radial wavenumbers as the flow decays. The very largest scales, $k \approx 1$, show continuously increasing anisotropy because these motions are on the scale of the domain size and may interact with themselves through the periodic boundary conditions of the domain. This is physically unrealistic but these scales of the flow contain only a small amount of energy. The contribution of 3D effects to the 2D

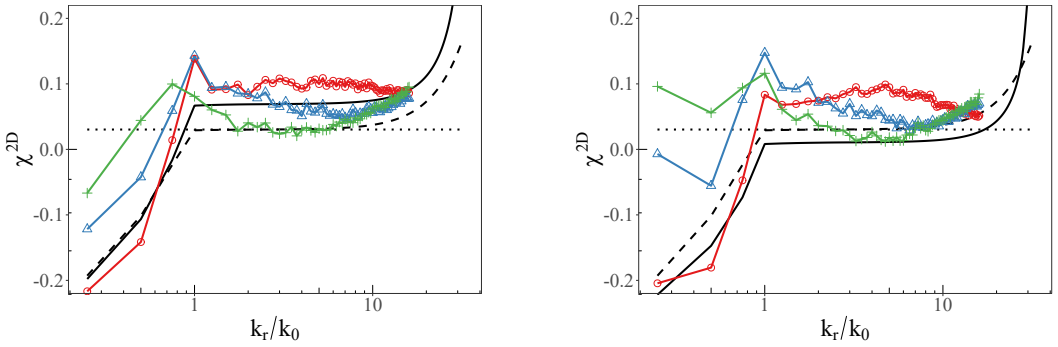

(a) $M_s = 1.5$. The LES spectra are taken at (○): $k_0x = 2.5$; (△): $k_0x = 7.8$; (+): $k_0x = 24.0$.

(b) $M_s = 2.2$. The LES spectra are taken at (○): $k_0x = 2.3$; (△): $k_0x = 7.7$; (+): $k_0x = 23.9$.

Figure 4.17: Time averaged anisotropy parameter downstream of a shock, for upstream conditions of $M_t \approx 0.18$ and $Re_\lambda \approx 500$ on a $1024\times256\times256$ base grid with 4× AMR. The solid line shows χ^{2D} calculated from the results of LIA applied to the model spectrum (3.10), and the dashed line is the preshock result for (3.10). The dotted line is the result for an infinite $k^{-5/3}$ spectrum. The LES results are given by the symbols, and are calculated in cross-sectional planes downstream of the shock at streamwise locations given in the subcaptions.

spectra limits the direct usefulness of χ^{2D} in determining when specific scales in the flow relax to isotropy, but this parameter will also be used in subsequent sections to connect the results of this LES to model problems that simplify analysis in 3D.

Figure 4.18 shows the behavior of the first few wavenumbers of the radial velocity spectra immediately downstream of the $M_s = 2.2$ shock. These spectra are taken at planes within the region where exponentially decaying pressure modes contribute significantly to the Reynolds stresses, but the radial spectrum of the streamwise Reynolds stresses predicted by LIA and LES still show remarkable agreement. The transverse velocity spectrum predicted in LIA shows qualitative agreement with the LES within the inertial range, but at low radial wavenumbers the transverse fluctuations see no significant amplification in the LES, and even see damping in the lowest radial wavenumbers as the flow progresses downstream from $k_0x = 0.7$ to $k_0x = 2.3$. It is notable that this damping at the lowest radial wavenumbers is not necessarily a large scale phenomenon, and would also be consistent with a loss of energy in fine scale transverse velocity modes with wavenumbers approximately normal to the shock plane that have been aliased onto low radial wavenumbers.

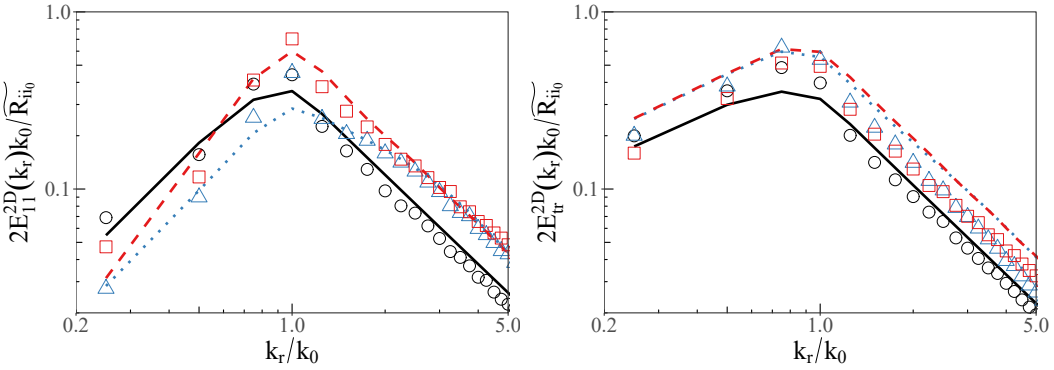

(a) Streamwise Velocity Spectra (b) Transverse Velocity Spectra

Figure 4.18: Time averaged radial power spectra of the streamwise and transverse velocities downstream of a $M_s = 2.2$ shock, for upstream conditions of $M_t \approx 0.18$ and $Re_\lambda \approx 500$ on a $1024 \times 256 \times 256$ base grid with 4× AMR. The symbols show the LES, and the lines show LIA applied to the model spectrum (3.10). Solid line (○): $k_0 x = -1.5$ upstream spectra. Dotted line (△): $k_0 x = 0.7$. Dashed line (□): $k_0 x = 2.3$.

The effect of a return to isotropy at inertial range scales

Previous DNS [45, 46] and experiments [4] have tended to observe larger Reynolds stress amplifications in the streamwise direction than in the transverse directions. This agrees with LIA at low M_s but, contrary to recent DNS, LIA predicts that the Reynolds stress anisotropy begins to strongly favor R_{tr} as M_s is increased. The behavior of the radial spectra in Figure 4.18, combined with the return to isotropy of most wavenumbers observed in Figure 4.17, offers insight into a mechanism that could explain why the Reynolds stress anisotropy from LIA has not reliably predicted the results of DNS at high M_s.

First, it is noted that low radial wavenumbers in the transverse velocity spectrum contain significantly more energy than those in the streamwise velocity spectrum. This is because vorticity modes with a 3D wavenumber vector normal to the shock contribute energy to the transverse Reynolds stresses, but when the 3D wavenumber is projected onto the plane of the shock the resulting radial wavenumber is small. Furthermore, to zeroth order, the modes with a wavenumber normal to the shock will see the greatest change in wavenumber across the shock as a result of the mean compression. This results in the transverse modes being disproportionately moved towards high wavenumbers as they pass over the shock, relative to streamwise velocity modes. At the lowest wavenumbers there are no energetic lower wavenumber modes available, and this transfer can result in the energy content in a fixed low

wavenumber decreasing across the shock, even if every upstream mode crossing the shock is amplified. LIA confirms that the shock damps the 1D transverse velocity spectrum at low wavenumbers [49, 73]. This means that the amplification of transverse modes is weighted towards high wavenumbers, which are shown in the LES to begin to return to isotropy downstream of the shock. The low wavenumbers, where the streamwise modes see greater amplifications, do not show the same return to isotropy, at least according to the radial spectra considered in Figure 4.17. Thus, the return to isotropy may drive energy from R_{tr} to R_{11} downstream of a shock even in scenarios where $R_{11} > R_{tr}$, because transverse fluctuations are focused at scales where the return to isotropy is faster.

LES with LIA modeling of the shock

It is noted that, while Figure 4.17 shows that the anisotropy parameter over the extent of the inertial range relaxes to a profile similar to that seen in the isotropic upstream turbulence, the relaxation to isotropy appears to be much slower than the development of the Reynolds stress anisotropy, which takes an approximately steady value for downstream positions $k_0 x > 5$. If the Reynolds stress anisotropy is strongly influenced by the relaxation to isotropy in the inertial range, then the inertial range must relax to isotropy more quickly than suggested by the 2D anisotropy parameter (4.4).

Describing the scale dependency of anisotropy with respect to 3D wavenumber is complicated by the shock and inhomogeneous direction in the full shock-turbulence LES, but some estimation of this behavior may be extracted from homogeneous LES initialized with a post-shock field from LIA. LIA is applied directly to the Fourier transform of a $Re_\lambda = 500$, $M_t = 0.18$, 256^3 forced periodic box LES to produce a 3D approximation to the far-field downstream of the shock [55, 76], that is anisotropic but remains periodic and homogeneous. This is then used as an initial condition for a decaying 256^3 LES, which acts as a model for the decay of a periodic, anisotropic element of turbulence downstream of a shock. This is referred to as LIA-processed LES, as LIA is used to model the instantaneous interaction of a periodic cube of turbulence with a shock. LES where the shock is explicitly simulated in the computational domain, as done in the other sections of this study, is referred to as shock-processed LES. DNS initialized with the far-field LIA result has been shown to converge towards shock-processed DNS as M_t is reduced [11], but LIA can alternatively produce a prediction for the near-field immediately downstream of a

shock. The decay of turbulence initialized with this near-field might produce a better agreement to shock-processed DNS, but the near-field from LIA is inhomogeneous which complicates boundary conditions and prevents the calculation of 3D spectra that are the primary motivation for this analysis.

Figure 4.19 shows the 3D spectra of the LIA-processed LES before LIA is applied, immediately after the application of LIA, and then after a small amount of post-LIA decay. The time at which these spectra are taken is converted to a spatial location using the mean streamwise velocity downstream of a stationary $M_s = 2.2$ shock, which allows comparison with the shock-processed LES. The oscillations in the spectra of the transverse velocity fluctuations are a result of the discretization of the upstream field onto integer wavenumbers, as some wavenumbers may not have a significant amount of energy mapped to them by LIA. The transfer of transverse fluctuations towards smaller scales over the shock is clearly visible in the spectra, and the energy content of transverse fluctuations is considerably damped at low wavenumbers. The downstream $k_0 x$ is quite close to the shock, but the flow has already begun to show a noticeable movement towards isotropy over most of the inertial range. The initial anisotropy in the inertial range varies greatly with shock Mach number, but these scales reliably return to isotropy over the range of M_s considered, as shown in Figure 4.20. The flows are initialized using the far-field LIA result, and thus do not contain the exponentially decaying pressure modes that are predicted near the shock. LIA predicts that pressure fluctuations are weighted towards high streamwise wavenumbers downstream of the shock [74], and pressure-velocity correlations are often believed to drive the Reynolds stresses towards isotropy. Thus, the actual flow which contains these fluctuations near the shock would be expected to return to isotropy at small scales faster than observed in this test case. The relaxation of these intermediate scale modes to isotropy may also be affected by the construction of the subgrid model, but it is noted that, unlike many SGS models, the HSVM-LES approach does not assume isotropy in the subgrid flows [70] , which has allowed previous applications of the model to anisotropic flows such as buoyancy-driven turbulence [14] . The SGS Reynolds stress anisotropy in HSVM-LES of modeled post-shock flows shows qualitatively similar behavior to that predicted by LIA [11], and the shock-processed LES conducted in this study also shows comparable results.

Figure 4.21 gives the Reynolds stress anisotropy from the same simulation as shown in Figure 4.19. Even though the LIA-processed LES is initialized with the far-field LIA result, which does not contain the exponentially decaying pressure modes

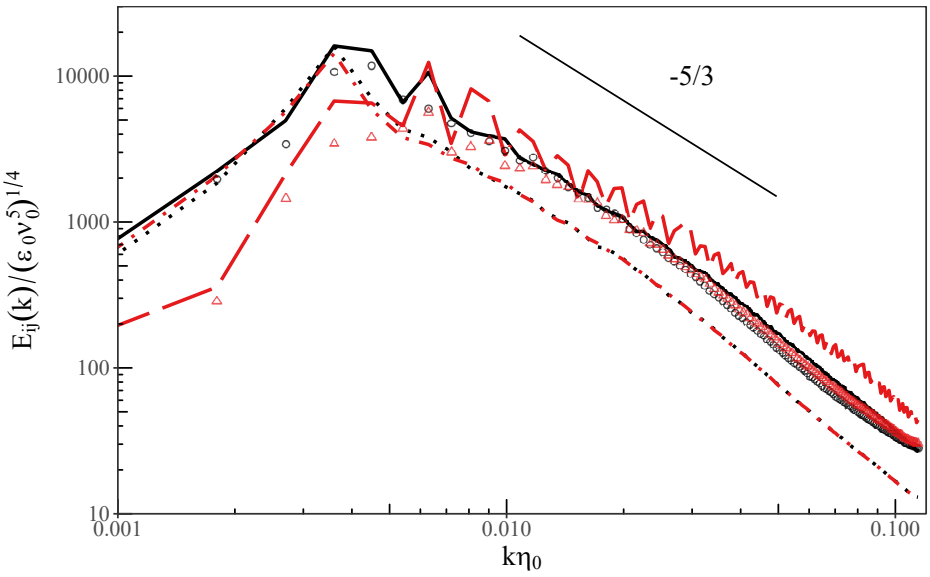

Figure 4.19: Three dimensional spectra of streamwise and transverse velocity fluctuations in LIA-processed LES, in which a periodic, anisotropic 256^3 LES is initialized by applying LIA to an isotropic LES with $Re_\lambda \approx 500$ and $M_t \approx 0.18$. The LIA models a $M_s = 2.2$ shock. An equivalent downstream position k_0x is produced by scaling the simulation time by the mean convection velocity downstream of a stationary shock. Dotted line: $E_{11}(k)$ pre-LIA. Dot-dashed line: $E_{22}(k)$ pre-LIA. Solid line: $E_{11}(k)$ at $k_0x = 0$. Dashed line: $E_{22}(k)$ at $k_0x = 0$. Circles: $E_{11}(k)$ at $k_0x = 6.0$. Triangles: $E_{22}(k)$ at $k_0x = 6.0$.

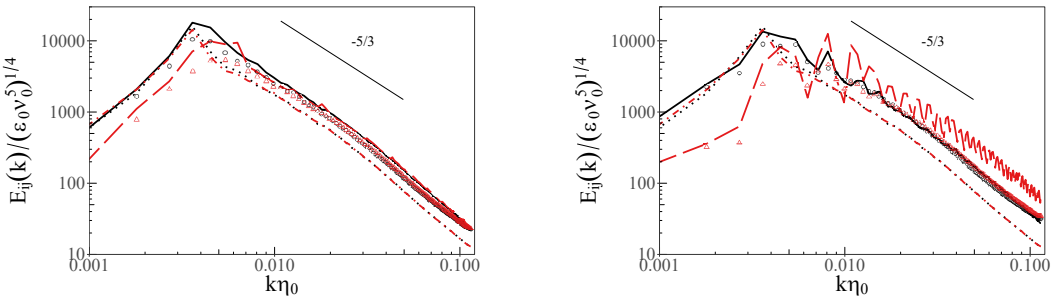

(a) $M_s = 1.5$. (b) $M_s = 3.0$.

Figure 4.20: Three dimensional spectra of streamwise and transverse velocity fluctuations in LIA-processed LES. Pre-LIA flow conditions are the same as in Figure 4.19. Dotted line: $E_{11}(k)$ pre-LIA. Dot-dashed line: $E_{22}(k)$ pre-LIA. Solid line: $E_{11}(k)$ at $k_0x = 0$. Dashed line: $E_{22}(k)$ at $k_0x = 0$. Circles: $E_{11}(k)$ at $k_0x = 6.0$. Triangles: $E_{22}(k)$ at $k_0x = 6.0$.

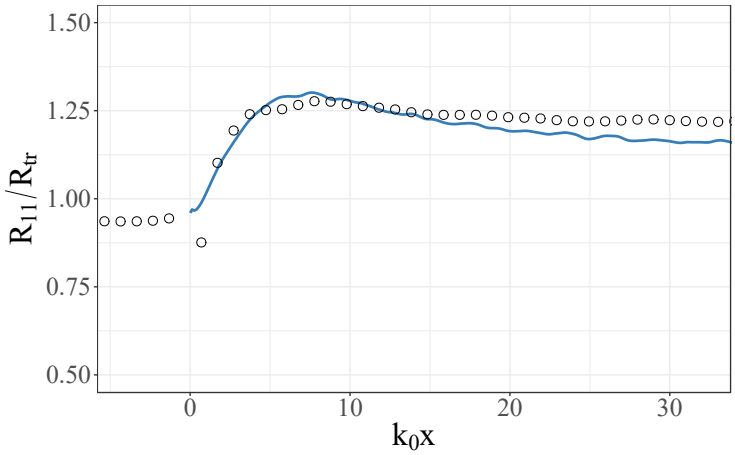

Figure 4.21: Reynolds stress anisotropy. The symbols show the anisotropy from shock-processed LES with $M_s = 2.2$, upstream $M_t \approx 0.18$ and $Re_\lambda \approx 500$ on a $1024 \times 256 \times 256$ base grid with 4× AMR. The line shows LIA-processed LES, in which LES in a periodic 256^3 box is initialized by applying LIA to an LES of homogeneous isotropic turbulence with the same upstream conditions. The temporal decay in the LIA-processed LES is converted to a spatial coordinate using the mean convection velocity downstream of the shock.

that contribute to the rapid rise in R_{11} downstream of a shock, there is still a rapid correction towards $R_{11} > R_{tr}$ within the span of time shown in Figure 4.19. The Reynolds stress anisotropy in the LIA-processed LES agrees well with the shock-processed LES, and both methods level off to an approximately constant Reynolds stress anisotropy beyond $k_0 x \approx 5$ downstream of the shock. The anisotropy parameter (4.4) calculated in 2D cross-sectional planes of the LIA-processed LES also exhibits similar behavior to that seen in transverse planes of the shock-processed LES, as shown in Figure 4.22. Despite difficulties in interpreting the 2D anisotropy parameter directly, its strong similarity to the model problem of the LIA-processed LES suggests that the scale-dependent relaxation to isotropy in the shock-processed LES proceeds in a similar manner to the LIA-processed LES. The inertial range of the LIA-processed LES relaxes to isotropy quickly, over timescales that would imply that the shock-processed LES has returned to isotropy over much of the extent of the inertial range by the time the Reynolds stress anisotropy has relaxed to its far-field value.

Post-processed LIA

To further illustrate the effect of inertial range isotropy on the Reynolds stresses, the far-field results of LIA applied to (3.10) with $k_{c,LIA} = 128$ are post-processed to

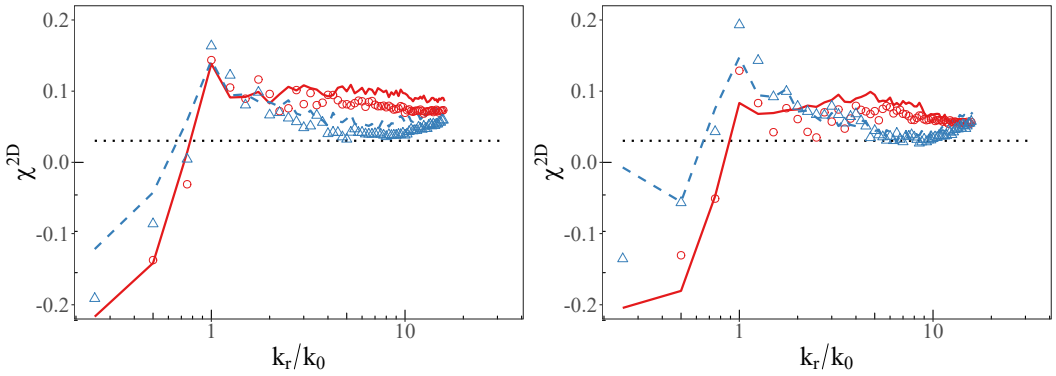

(a) $M_s = 1.5$ (b) $M_s = 2.2$

Figure 4.22: Anisotropy parameter calculated from 2D radial spectra in planes parallel to the shock. The pre-shock flow has $Re_\lambda = 500$ and $M_t = 0.18$. The lines show shock-processed LES, in which the shock is explicitly simulated, and the symbols show LIA-processed LES. The temporal decay in the LIA-processed LES is converted to a spatial coordinate using the mean convection velocity downstream of the shock. Solid lines and circles: $k_0 x \approx 2.3$. Dashed line and triangles : $k_0 x \approx 7.7$. Dotted line: $\chi^{2D} = 1/33$ analytical result for an infinite isotropic $k^{-5/3}$ spectrum.

enforce that the 3D spectra of $E_{11}(k)$ and $E_{22}(k)$ are equal for $k \geq k_{iso}$, where $k_{iso} = 2k_0$. The Reynolds stresses are then reconstructed by integrating the spectra, and the resulting Reynolds stress anisotropy is shown in Figure 4.23. This post-processing affects the distribution of energy in the Reynolds stresses, but aggregate quantities such as the turbulent kinetic energy remain unchanged. With this modification, LIA agrees more closely with the shock-processed LES at high M_s. The selection of $k_{iso} = 2k_0$ is arbitrary because in practice the largest scales that are isotropic will depend on the shock Mach number and how far downstream measurements are taken, but this selection is approximately the beginning of the inertial range in the post shock flow in Figure 4.19. LIA also predicts that the intersection of $E_{11}(k)$ and $E_{22}(k)$ in the post shock field also corresponds to roughly $k = 2k_0$ for $M_s > 2$.

DNS also exhibits behavior consistent with the assertion that Reynolds stress anisotropy is significantly affected by a rapid return to isotropy at finer scales. Good agreement between DNS and LIA has been observed regarding the kinetic energy amplification over a shock, but DNS has not shown a distinct trend towards the LIA results for the individual Reynolds stresses as Re_λ is increased up to $Re_\lambda \approx 75$ [46], despite the prediction of Ryu and Livescu [76] that LIA will become more accurate at high Re_λ based on the ratio of the viscous to shock lengthscales. The scaling argument of Ryu and Livescu [76] is a predictor of nonlinear behavior in

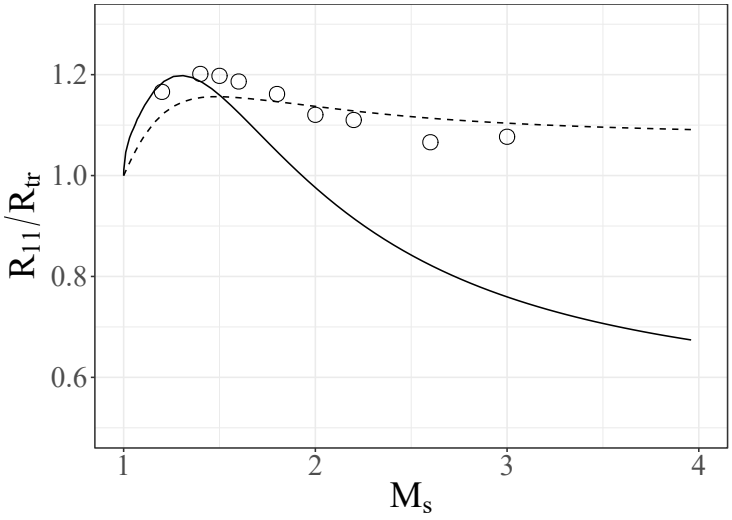

Figure 4.23: Reynolds stress anisotropy. The symbols show the anisotropy at the location of the peak downstream value of R_{11} in LES with upstream $M_t \approx 0.06$ and $Re_\lambda \approx 500$ on a $512 \times 128 \times 128$ base grid with 4× AMR. The solid line is the far field result of LIA. The dashed line is produced by applying LIA to the model spectrum (3.10) and post-processing the results to enforce that all wavenumbers $k/k_0 > 2$ have returned to isotropy downstream of the shock.

the instantaneous interaction of turbulence with a shock, whereas a scale-dependent relaxation to isotropy as suggested here would result from rapid nonlinear effects in the downstream turbulence. This is not the only non-linear phenomenon that could restrict the range of flow conditions over which LIA is practically useful at larger M_s, but Figure 4.23 suggests that this process may have substantial effect on the Reynolds stress anisotropy, sufficient to explain much of the discrepancy between LIA and DNS.

4.7 Discussion

LES of canonical shock-turbulence interactions are conducted to investigate the flow at high Reynolds number. Adaptive mesh refinement is applied in the direct vicinity of the shock. The results show reasonable agreement with previous DNS at low Taylor-based Reynolds number, with an acceptably small amount of variation with mesh resolution. With sufficient mesh refinement about the shock, the LES shows a convergence towards the $k^{-11/3}$ scaling in the shock surface corrugation predicted by linear analysis, providing an additional validation that the mesh is fine enough that the shock-capturing scheme is not interfering with the interaction of the turbulence with the shock. The amplification in the kinetic energy dissipation rate predicted by LES ceases to agree well with Linear Interaction Analysis (LIA) at larger shock

Mach numbers, and thus results are focused on the parameter space of $M_s \leq 2.2$.

No significant Reynolds number effects are observed in the LES for Reynolds numbers larger than $Re_\lambda = 100$. There is a discernible dependency on Re_λ in the Reynolds stress amplifications at $Re_\lambda < 100$, but as seen in previous DNS the effects of Re_λ within this range remains quite small.

Studies of shock-turbulence interactions at high shock Mach numbers have observed that the downstream Reynolds stress anisotropy, defined as the ratio of the streamwise to transverse Reynolds stresses, R_{11}/R_{tr}, consistently favors R_{11}. The transverse Reynolds stresses are disproportionately weighted towards smaller scales at high M_s, and as the flow relaxes towards isotropy at inertial range scales there is a transfer of energy towards the streamwise Reynolds stress. The LES suggests that this relaxation to isotropy occurs quickly over the extent of the inertial range, producing larger R_{11} values than predicted by linear theory. An unusual phenomenon in which the return to isotropy transfers energy from R_{tr} into R_{11} may occur even in the situations where $R_{11} > R_{tr}$.

LIA, as applied here, neglects the interaction of dilatational modes in the upstream turbulence with the shock and this assumption, along with other phenomena, could also contribute to LIA requiring increasingly restrictive flow conditions at higher M_s in order to capture the Reynolds stress anisotropy downstream of the shock. LIA is shown to agree more closely with the LES when the LIA results are post-processed to assume the downstream inertial range scales are isotropic, showing that the effects of this relaxation of inertial range scales to isotropy are of a sufficient magnitude that this process could explain much of the difference between LIA and LES. The agreement between the LES and LIA regarding factors other than the Reynolds stresses, such as the shock corrugation spectrum and the radial spectrum of streamwise velocity fluctuations near the shock, suggests that at high Reynolds numbers the instantaneous interaction of the shock with the turbulence at the subject $M_t \leq 0.18$ turbulent Mach numbers can be considered to be effectively linear, but nonlinear small scale interactions are significant over the short distance downstream of the shock as the flow is relaxing towards its far-field behavior, particularly at large M_s. It is noted that some Reynolds-averaged models have either been tuned [80] or explicitly constructed [e.g. 83] to agree with the Reynolds stress trends seen in LIA, and this analysis would suggest that this may be a more robust approach than previously recognized, so long as the scale dependent relaxation to isotropy is accurately modeled.

Chapter 5

ENSEMBLE AVERAGING OF A CORRUGATED SHOCK

5.1 Introduction

Large Eddy Simulation (LES) relaxes the computational requirements to simulate the canonical shock-turbulence problem relative to DNS, but LES may still become prohibitively expensive in complex problems or when a large parameter space must be explored. Performing LES of shocked flows is also non-trivial, because standard methods to numerically stabilize a shock tend to be excessively dissipative when applied to turbulence [25] and models for the effects of subgrid flows may not perform well at discontinuities. Furthermore, LES should resolve corrugations that develop in the shock [26], and this will usually require localized mesh refinement which substantially increases computational cost.

Reynolds-Averaged Navier-Stokes (RANS) methods thus remain in widespread use, particularly in practical engineering applications. These models average the governing equations, relaxing resolution requirements and often reducing the dimensionality of problems, but introduce unclosed correlations that must be modeled, typically by empirical calibration to experiments or high fidelity simulations. Recent efforts have been made to develop RANS models for compressible and variable density flows [7, 32, 80], applicable to fundamental flows such as Richtmyer-Meshkov instabilities in which a shock perturbs a material interface, which then develops into a turbulent layer upon reshock.

Capturing the behavior of shocks in RANS remains difficult, even in the simplified case where density fluctuations in the turbulence arise only from compressibility effects. Sinha et al. [83] showed common transport models for turbulent kinetic energy and dissipation failed to converge upon mesh refinement in the presence of shocks, and presented a model [81, 83] based on linear analysis that resolves mesh convergence problems but requires explicit knowledge of the shock Mach number. Reconstruction of the closure models into a conservative form is shown to improve numerical convergence [82, 88], but it is not generally possible to convert an existing model to this form. Schwarzkopf et al. [80] produced Reynolds stress amplifications through a shockwave that agreed reasonably well with linear theory, but did not consistently observe a monotonic decay in the effects of changing the

computational mesh , even at meshes that would be impractical outside of one-dimensional problems. The magnitude of the observed mesh resolution effects was considered to be acceptably small, but the absence of a consistent scaling in mesh effects, such as $O(\Delta x)$, suggests that the numerical convergence behavior of this model is difficult to predict and likely dependent on the specific numerical method used at the shock. Griffond et al. [34] produce a model tuned to match Linear Interaction Analysis (LIA) by coupling the closure model with a pseudopressure numerical approach that constructs shock fronts as continuous features, and Griffond and Soulard [33] expand on this approach to allow for the evaluation of other turbulence models against LIA.

Models using traditional shock-capturing schemes that apply artificial viscous dissipation to stabilize the shock at roughly the thickness of the local mesh often face convergence issues in RANS arising from the shrinking shock width as the mesh is refined. Direct Numerical Simulation (DNS, e.g. [45]) shows that the corrugation the shock undergoes as it passes through turbulence produces mean profiles with an ensemble-averaged shock width of a comparable order of magnitude to the energetic turbulent scales, which are often possible to resolve on the computational mesh. This implies that if the correct profiles for primitive quantities-averaged density, velocity and pressure-were produced in RANS, convergence problems would be reduced to, at worst, resolving a reasonably large shock lengthscale. This concept has similarities with the pseudopressure formulation used by Griffond and Soulard [33], but differs in that the proposed shock width is a physical quantity. Subsequent references to shock thickness refer to the thickness of profiles of ensemble averaged variables near a shock, and should not be confused with the instantaneous shock thickness which remains on the order of the mean free path.

It is also apparent from DNS [45, 46, 48] that shock-turbulence interactions see a small but significant deviation from the laminar Euler equation amplifications in primitive mean flow variables, with the post-shock mean densities lower than predicted by the laminar normal shock relations. This effect approximately scales with the square of the ratio of the turbulent Mach number to the shock Mach number [46]. Lele [51] modeled the effect of turbulence on the mean flow jump relations using rapid distortion theory, and showed that the velocity of the shock passing through turbulent flow is also changed relative to the laminar case.

The purpose of this study is to address capturing the shock jump conditions and averaged shock profile width in RANS. Section 5.2 describes the existing RANS

model that this study uses as a starting point. A simple model for the large Reynolds stress present in the vicinity of the shock is produced by analysis of two uniform flow regions separated by an interface consistent with the shock corrugation predicted by linear analysis, as discussed in section 5.3. Section 5.4 develops a model for correlations in the energy equation that accounts for the generation and convection of turbulent entropy or acoustic modes, and section 5.5 evaluates the effectiveness of the proposed changes to the RANS model.

5.2 The BHR-3 RANS Model

The subject work uses the two-lengthscale BHR-3 RANS model of Schwarzkopf et al. [80], but only single species fluids are considered here. The Navier-Stokes equations are decomposed into ensemble-averaged and fluctuating components, $f = \overline{f} + f'$. Favre, or density-weighted, averages are constructed as $\tilde{f} = \overline{\rho f}/\overline{\rho}$ and $f'' = f' - \overline{\rho' f'}/\overline{\rho}$. Note that the definitions for $\overline{f}$ and $\tilde{f}$ are defined as averaged quantities in RANS, whereas in the previous LES chapters they referred to filtered fields. The Favre-averaged governing equations for the density ρ, velocity u_i, and total energy E are given as

$$\frac{\partial \overline{\rho}}{\partial t} + \frac{\partial}{\partial x_i}\left(\overline{\rho}\tilde{u}_i\right) = 0, \tag{5.1a}$$

$$\frac{\partial \overline{\rho}\tilde{u}_i}{\partial t} + \frac{\partial}{\partial x_j}\left(\overline{\rho}\tilde{u}_i\tilde{u}_j + \overline{P}\delta_{ij} + \overline{\rho}\tilde{R}_{ij}\right) = \overline{\rho}g_i, \tag{5.1b}$$

$$\begin{aligned}\frac{\partial \overline{\rho}\tilde{E}}{\partial t} + \frac{\partial}{\partial x_j}\left(\overline{\rho}\tilde{u}_j\tilde{E}\right) &= -\frac{\partial}{\partial x_j}\left(\overline{P}\tilde{u}_j\right) - \frac{\partial}{\partial x_j}\left(\overline{\rho}\tilde{u}_j\tilde{R}_{ij}\right) \\ &-\frac{\partial}{\partial x_j}\left(\overline{P'u'_j}\right) - \frac{\partial}{\partial x_j}\left(\overline{\rho I'' u''_j}\right) - \frac{1}{2}\frac{\partial}{\partial x_j}\left(\overline{\rho u''_i u''_i u''_j}\right),\end{aligned} \tag{5.1c}$$

where g_i is a body force and $\tilde{R}_{ij} = \overline{\rho u''_i u''_j}/\overline{\rho}$ is the Reynolds stress. Repeated indices denote summation. The pressure P, temperature T, and internal energy I are related by the ideal gas equation of state $\overline{P} = (\gamma - 1)\,\overline{\rho}\tilde{I}$, and $\tilde{I} = C_v\overline{T}$ for a constant specific heat at constant volume, C_v. The ratio of specific heats, $\gamma = 1.4$, is constant. The total energy is related to the internal energy by $\tilde{E} = \tilde{I} + \tilde{R}_{ii}/2 + \tilde{u}_i\tilde{u}_i/2$. The BHR-3 model tracks transport equations for $\tilde{R}_{ij}$, a turbulent transport lengthscale S_T, a turbulent dissipation lengthscale S_D, the mass-weighted turbulent velocity $a_i = -\overline{u''_i}$, and the density-specific volume correlation $b = \overline{\rho' v'}$. For brevity these equations are not reproduced here, as they are used without modification from previous work [80]. Schwarzkopf et al. [80] models the pressure-velocity and internal energy-velocity

correlations on the right hand side of (5.1c) by gradient diffusion relations, but these are treated differently in this work as discussed in section 5.4.

The model is implemented numerically in the adaptive mesh refinement AMROC framework [19] with a 2nd order WENO scheme in space and a 3rd order strong stability preserving Runge-Kutta scheme in time [31].

5.3 Ensemble Averaging of a Corrugated Shock

The surface of a shock passing through a turbulent upstream flow corrugates, and over an ensemble of different turbulent initial conditions the instantaneous position of a shock will occur over a distribution of possible locations. The width of the ensemble-averaged shock profile is thus expected to be much wider than the instantaneous shock front, and it has previously been observed that this corrugation produces a large spike in the streamwise Reynolds stress, which reaches a value of $\Delta\overline{u}_1^2/4$ at the center of the shock [46], where $\Delta\overline{u}_1$ is the change in the mean streamwise velocity across the shock. Reconstructing the correct shock profile width in RANS is thus expected to be a matter of properly capturing this large, near-shock Reynolds stress.

A simple model for the Reynolds stress within a shock is obtained by considering a single mode perturbation on a shock which separates a region of unshocked flow with constant average velocity $\overline{u}_{1,u}$ from shocked flow with constant average velocity $\overline{u}_{1,d}$, such that

$$u_1(x, y, z, t) = \overline{u}_{1,u} + \Delta\overline{u}_1 H(x + \xi(y, z, t)) + u'_{turb}(x, y, z, t). \tag{5.2}$$

The x direction corresponds to the mean shock normal direction, $H(x)$ is the Heaviside step function, ξ is the instantaneous perturbation of the shock front from its mean position, and u'_{turb} represents turbulent fluctuations in the flow. The subscripts 'u' and 'd' refer to quantities in the upstream pre-shock and downstream post-shock states, respectively. The reference frame is such that the mean location of the shock is stationary and located at $x = 0$. The pre-shock turbulence is assumed to be vortical and satisfy $M_t \ll (M_s - 1)$ for turbulent Mach number $M_t = \sqrt{\widetilde{R}_{ii,u}}/\overline{c}_u$ and shock Mach number $M_s = \tilde{u}_{1,u}/\overline{c}_u$, where $\overline{c} = \sqrt{\gamma\overline{P}/\overline{\rho}}$ is the sound speed. Fluctuations in the turbulence are small compared to the mean shock jump under this condition, implying that $\Delta\tilde{u}_1 \approx \Delta\overline{u}_1 = \overline{u}_{1,d} - \overline{u}_{1,u}$. Likewise, fluctuations in (5.2) that arise from the perturbed motion of the shock, ξ, are on the order of the mean shock jump and are consequently much larger than turbulent fluctuations. Thus, the upstream

turbulent fluctuations are considered when determining the behavior of the shock perturbation, ξ, but the contribution of u'_{turb} to mean profiles or correlations such as $\tilde{R}_{ij}$ is small within the extent of the shock corrugations, allowing u'_{turb} to be otherwise neglected in this analysis. The pressure and density fields follow equivalent relations as (5.2).

Linear Interaction Analysis (LIA) is used to connect the shock perturbation to turbulent quantities in the upstream flow. LIA is discussed in more detail in Appendix A. LIA is limited to the low turbulent Mach number regime considered here, $M_t \ll (M_s - 1)$, but under this condition it has shown reasonable agreement with DNS [76]. The shock perturbation corresponding to a single upstream vorticity mode oriented in the $x - y$ plane is predicted in LIA as

$$\xi = -\frac{1}{mk} L e^{ik\left(ly - \overline{u}_{1,u} mt\right)}, \tag{5.3}$$

where $m = \cos(\psi)$ and $l = \sin(\psi)$ for a mode of wavenumber k and incident angle ψ with the shock. Expressions to determine the constant L are provided in Mahesh et al. [64]. Neglecting the contribution of turbulent fluctuations about the upstream and downstream mean flows, the field (5.2) can then be written as

$$u_1(x, y) = \overline{u}_{1,u} + \Delta\overline{u}_1 H\left(x + \frac{L}{m\,k}\cos(k\,l\,y)\right), \tag{5.4}$$

noting that the time dependency only introduces a phase shift and thus has been dropped. Averaging (5.4) in the y-direction provides mean flow profiles consistent with the single wave LIA solution,

$$\overline{u}_1(x) = \overline{u}_{1,d} - \frac{\Delta\overline{u}_1}{\pi}\cos^{-1}\left(\frac{mkx}{L}\right). \tag{5.5}$$

The field of velocity fluctuations is given by

$$u'_{1,u}(x) = \overline{u}_{1,u} - \overline{u}_1(x) = \frac{-\Delta\overline{u}_1}{\pi}\cos^{-1}\left(\frac{-mkx}{L}\right), \tag{5.6a}$$

$$u'_{1,d}(x) = \overline{u}_{1,d} - \overline{u}_1(x) = \frac{\Delta\overline{u}_1}{\pi}\cos^{-1}\left(\frac{mkx}{L}\right), \tag{5.6b}$$

$$u'_1(x, y) = u'_{1,u}(x) + (u'_{1,d}(x) - u'_{1,u}(x))H\left(x + \frac{L}{m\,k}\cos(k\,l\,y)\right). \tag{5.6c}$$

The fields of pressure and density fluctuations again follow equivalent forms. Correlations of interest, such as the Reynolds stresses, may be constructed by multiplying

various combinations of the fluctuating fields and averaging in the transverse direction. The Reynolds-averaged and Favre-averaged Reynolds stresses,

$$\overline{u_1' u_1'} = \frac{\Delta\overline{u}_1^2}{\pi^2} \cos^{-1}\left(\frac{k\, m\, x}{L}\right) \cos^{-1}\left(\frac{-k\, m\, x}{L}\right), \tag{5.7a}$$

$$\widetilde{R}_{11} = \frac{\overline{\rho u_1'' u_1''}}{\overline{\rho}} = \frac{\overline{\rho}_u\, \overline{\rho}_d\, \Delta\overline{u}_1^2 \cos^{-1}\left(\frac{k\, m\, x}{L}\right) \cos^{-1}\left(\frac{-k\, m\, x}{L}\right)}{\left(\overline{\rho}_u \cos^{-1}\left(\frac{k\, m\, x}{L}\right) + \overline{\rho}_d \cos^{-1}\left(\frac{-k\, m\, x}{L}\right)\right)^2}, \tag{5.7b}$$

are shown in Figure 5.1, normalized by the velocity jump. Both averaging methods yield the same peak value, but the distribution of the Favre-averaged Reynolds stress skews towards the upstream flow as the shock Mach number is increased. A more detailed derivation of the Reynolds stress within this region is provided in Appendix C, which also contains expressions for some other correlations of interest.

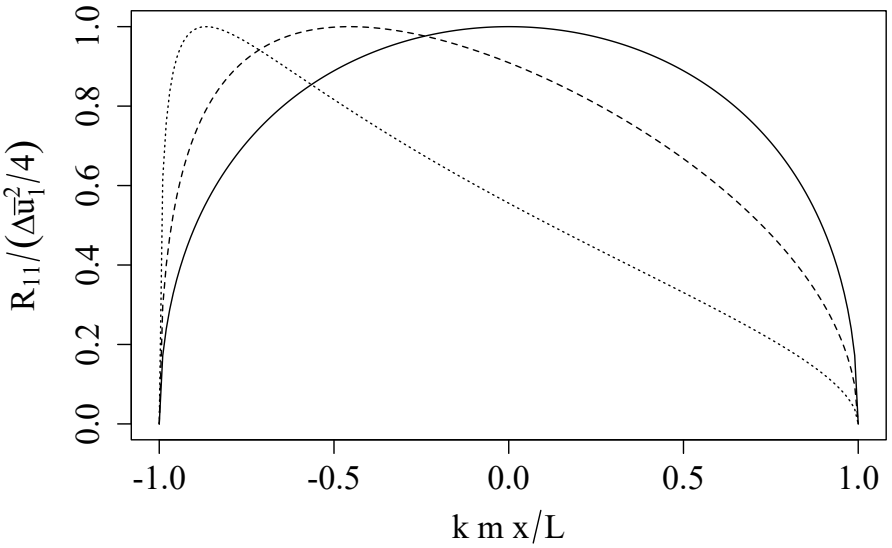

Figure 5.1: Reynolds stress distribution within the region of interface corrugation. The solid line corresponds to $\overline{u_1' u_1'}$ at all M_s and $\widetilde{R}_{11}$ at $M_s = 1$. Dashed line : $\widetilde{R}_{11}$ at $M_s = 1.5$. Dotted line : $\widetilde{R}_{11}$ at $M_s = 5$.

5.3.1 Reynolds Stress Transport

The exact transport equation for the Favre-averaged Reynolds stress is [79]

$$\begin{aligned}\frac{\partial \overline{\rho}\tilde{R}_{ij}}{\partial t} + \frac{\partial \overline{\rho}\tilde{u}_k\tilde{R}_{ij}}{\partial x_k} = \; & a_i\frac{\partial \overline{P}}{\partial x_j} + a_j\frac{\partial \overline{P}}{\partial x_i} - \overline{\rho}\tilde{R}_{ik}\frac{\partial \tilde{u}_j}{\partial x_k} - \overline{\rho}\tilde{R}_{jk}\frac{\partial \tilde{u}_i}{\partial x_k} \\ & - a_i\frac{\partial \tilde{\sigma}_{jk}}{\partial x_k} - a_j\frac{\partial \tilde{\sigma}_{ik}}{\partial x_k} - \frac{\partial}{\partial x_k}\overline{\rho u_i'' u_j'' u_k''} \\ & + \frac{\partial}{\partial x_k}\left(\overline{u_i''\sigma_{jk}''} + \overline{u_j''\sigma_{ik}''}\right) - \frac{\partial}{\partial x_j}\overline{u_i'' P'} - \frac{\partial}{\partial x_i}\overline{u_j'' P'} \\ & + \overline{P'\frac{\partial u_i''}{\partial x_j}} + \overline{P'\frac{\partial u_j''}{\partial x_i}} - \overline{\sigma_{jk}''\frac{\partial u_i''}{\partial x_k}} + \overline{\sigma_{ik}''\frac{\partial u_j''}{\partial x_k}},\end{aligned} \tag{5.8}$$

where σ is the viscous stress tensor. Modeling unclosed terms on the right hand side of (5.8) represents the bulk of the assumptions in Reynolds-averaged methods, and there is interest in observing how the transport equation behaves as it processes the turbulence in a corrugated shock. The large Reynolds stress arising from shock corrugations is transported with the shock, rather than with the fluid, which suggests that (5.8) may not be a practical basis for modeling shock corrugation effects, but integration of (5.8) using Favre-averaged profiles constructed from (5.5) and (5.6) provides insight into how the large Reynolds stress at the shock is produced in the governing equations. Assuming a statistically stationary state and neglecting viscous stresses, (5.8) is integrated from the upstream flow to the peak position of $\widetilde{R}_{11}$, denoted x_0,

$$\begin{aligned}\overline{\rho}_u\tilde{u}_u\Delta_{x_0}\tilde{R}_{11} = & 2\int_{-\infty}^{x_0} a_1\frac{\partial \overline{P}}{\partial x_1}dx - 2\int_{-\infty}^{x_0}\overline{\rho}\tilde{R}_{11}\frac{\partial \tilde{u}_1}{\partial x_1}dx \\ & - \Delta_{x_0}\overline{\rho u_1'' u_1'' u_1''} - 2\Delta_{x_0}\left(\overline{u_1'' P'}\right) + 2\int_{-\infty}^{x_0}\overline{P'\frac{\partial u_1''}{\partial x_1}}dx,\end{aligned} \tag{5.9}$$

$$x_0 = \frac{L}{m\,k}\cos\left(\frac{\pi\overline{\rho}_d}{\overline{\rho}_u + \overline{\rho}_d}\right). \tag{5.10}$$

The notation $\Delta_{x_0} f = f|_{x=x_0} - f|_{x=-\infty}$ denotes the difference between the value of f at x_0 and in the upstream flow. The first two integrals on the right hand side of (5.9) are traditionally considered to represent the production of turbulent kinetic energy from the pressure gradient and velocity gradient, respectively, but the shock corrugations are expected to behave significantly differently than traditional turbulent Reynolds stresses. These first two integrals can be integrated in a straightforward manner after the relevant correlations have been constructed from (5.6). The contribution

from the triple correlation integrates to zero. The last integral contains a Heaviside function multiplied by a Dirac delta function, which is not formally integrable, but it may be shown, if the order of integration and differentiation are allowed be interchanged, that

$$\overline{P'\frac{\partial u_1''}{\partial x_1}} = \frac{\Delta\overline{u}_1}{\Delta\overline{P}}\overline{P'\frac{\partial P'}{\partial x_1}} = \frac{\Delta\overline{u}_1}{2\Delta\overline{P}}\frac{\partial}{\partial x_1}\overline{P'P'} = \frac{1}{2}\frac{\partial}{\partial x_1}\overline{P'u_1''}. \tag{5.11}$$

Figure 5.2 shows the relative contribution of each source term to the Reynolds stress amplification between the upstream edge of the shock profile and x_0. At low Mach numbers, the combined pressure-dilatation and pressure-velocity correlations are responsible for most of the Reynolds stress amplification, but as the Mach number is increased the first two integrals of (5.9) quickly become significant. The inability of conventional RANS models to reproduce the large Reynolds stresses within the extent of the shock corrugations thus cannot be blamed on a single closure model in the Reynolds stress equations failing inside of a shock.

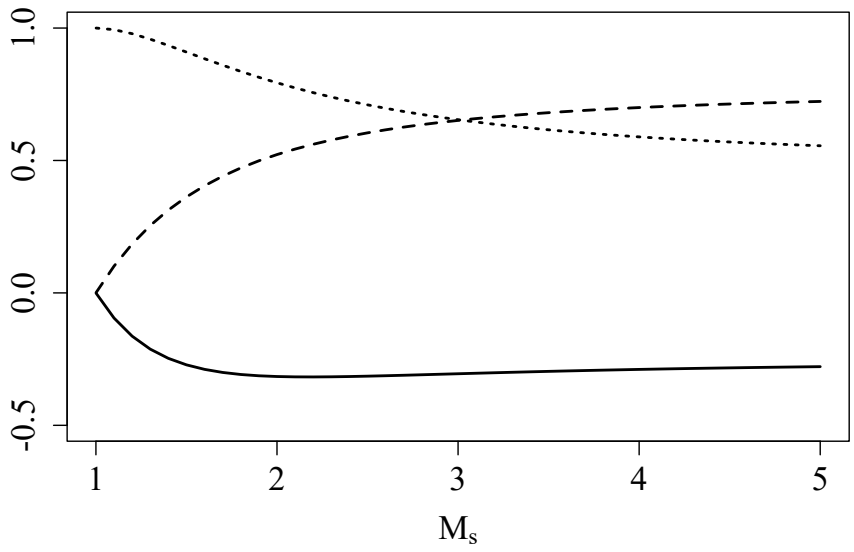

Figure 5.2: Reynolds stress source terms integrated from upstream to the peak-$\widetilde{R}_{11}$ location. Solid line : $2\int_{-\infty}^{x_0} a_1 \frac{\partial \overline{P}}{\partial x_1} dx$. Dashed line : $-2\int_{-\infty}^{x_0} \overline{\rho}\tilde{R}_{11}\frac{\partial \tilde{u}_1}{\partial x_1} dx$. Dotted line : $-\Delta_{x_0}\left(\overline{u_1''P'}\right)$. All results are normalized with respect to $\overline{\rho}_u\tilde{u}_u\Delta\overline{u}_1^2/4$.

5.3.2 A Localized Shock Corrugation Model

It is desirable to develop a model that is capable of reproducing the large spike in Reynolds stresses that results from averaging over corrugations in the shock, without requiring a priori knowledge of the shock Mach number or location. The goal of including the large Reynolds stress immediately near the shock is to reproduce the physical width of the ensemble-averaged shock profile. An additional Reynolds stress term representing shock corrugation effects, $\widetilde{R}_{ij,shock}$, is explicitly introduced into the averaged momentum and energy equations where $\widetilde{R}_{ij}$ now denotes the convective model for the Reynolds stress that is tracked in BHR-3 [80]. The Reynolds stress resulting from shock corrugation is not transported with the flow, nor is it modeled in conventional Reynolds stress transport models such as BHR-3, and thus a linear combination of the Reynolds stress arising from shock corrugation with the Reynolds stress arising directly from turbulent fluctuations is considered. The resulting momentum and energy equations are given by

$$\frac{\partial}{\partial t}\left(\overline{\rho}\tilde{u}_i\right) + \frac{\partial}{\partial x_j}\left(\overline{\rho}\tilde{u}_i\tilde{u}_j + \overline{P}\delta_{ij} + \overline{\rho}\left(\widetilde{R}_{ij,shock} + \widetilde{R}_{ij}\right)\right) = \overline{\rho}g_i, \tag{5.12a}$$

$$\begin{aligned}\frac{\partial}{\partial t}\left(\overline{\rho}\tilde{E}\right) + \frac{\partial}{\partial x_j}\left(\overline{\rho}\tilde{u}_j\tilde{E}\right) = &-\frac{\partial}{\partial x_j}\left(\overline{\rho}\tilde{u}_j\left(\widetilde{R}_{ij,shock} + \widetilde{R}_{ij}\right)\right) - \frac{\partial}{\partial x_j}\left(\overline{P}\tilde{u}_j\right) \\ &-\frac{\partial}{\partial x_j}\left(\overline{P'u'_j}\right) - \frac{\partial}{\partial x_j}\left(\overline{\rho I''u''_j}\right) - \frac{\partial}{\partial x_j}\left(\overline{\rho u''_i u''_i u''_j}\right).\end{aligned} \tag{5.12b}$$

A model is developed for $\widetilde{R}_{ij,shock}$ by considering the behavior of $\overline{u'_1u'_1}$ at the centerpoint of the shock profile. The Reynolds-averaged Reynolds stress is used for its simplicity, and as previously shown in Figure 5.1 the Favre-averaged Reynolds stress behaves in a similar manner except for its more complex distribution. Evaluating (5.7a) and the gradient of (5.5) at the centerline of the shock yields

$$\overline{u'_1u'_1}(x=0) = \Delta\overline{u}_1^2/4, \tag{5.13a}$$

$$\Delta\overline{u}_1 = \frac{\pi L}{mk}\left.\frac{\partial\overline{u_1}(x)}{\partial x}\right|_{x=0}. \tag{5.13b}$$

Inserting the second relation into the first provides an approximation for the Reynolds stress term inside the shock as a function of the local velocity divergence

$$\overline{u'_1u'_1} = \frac{\pi L\Delta\overline{u}_1}{4mk}\frac{\partial\overline{u_1}}{\partial x}. \tag{5.14}$$

Alternative formulations in terms of the square of the velocity divergence are also possible, but (5.14) is selected because it was found to simplify the subsequent analysis. Equation (5.14) is only valid for only a single mode perturbation, and L, m, and k must be related to general turbulent statistics in the upstream flow. Following the procedure of Mahesh et al. [64], the solution is integrated over all upstream Fourier modes in spherical coordinates. Assuming vortical, isotropic upstream turbulence,

$$\widetilde{R}_{11,shock} = 4\pi \int_{k=0}^{\infty} \frac{\pi \overline{u}_{1,u} A_v}{k} k^2 \, dk \int_{\psi=0}^{\pi/2} \frac{\breve{L}}{4m} \sin\psi \, d\psi \left(\frac{\overline{u}_{1,d}}{\overline{u}_{1,u}} - 1 \right) \frac{\partial \overline{u}(x)}{\partial x}. \quad (5.15)$$

$\breve{L} = L/A_v$ is the shock perturbation amplitude normalized by the non-dimensional pre-shock vorticity wave amplitude, A_v, which is related to the upstream energy spectrum as $\overline{u}_{1,u}^2 A_v^2 = E(k)/\left(4\pi k^2\right)$. The wavenumber integral thus has a dependence on the specific shape of the energy spectrum, consistent with the findings of LIA [64]. The upstream spectrum will typically not be known, but LIA suggests that the shock perturbation amplitude decays like $E(k)/k^2$. This means the shock corrugation is primarily driven by the low wavenumbers, and so it is considered sufficient to assume all turbulent energy exists in a single band of wavenumbers,

$$\overline{u}_{1,u} A_v \approx \frac{\sqrt{K}}{4\pi k^2} \delta(k - k_0). \quad (5.16)$$

k_0 is the wavenumber corresponding to the maximum in the upstream energy spectrum, and $\delta(x)$ is the 1-D Dirac delta function. The upstream turbulent kinetic energy is approximated by the Favre-averaged $K = \tilde{R}_{ii}/2$, noting that density fluctuations are small in the vortical upstream turbulence and so there is minimal difference between Reynolds and Favre averaging. The integral then reduces to

$$4\pi \int_{k=0}^{\infty} \frac{\pi \overline{u}_{1,u} A_v}{k} k^2 \, dk \approx \frac{\pi}{k_0} \sqrt{K} \approx S_T \sqrt{K}. \quad (5.17)$$

The transport lengthscale is approximated by $S_T = \pi/k_0$. The integral over wave orientations in (5.15) is a function of Mach number, but for large M_s this dependency largely cancels with the M_s-dependency of the velocity ratio. This term is used as a shock detection flag, and as a means to turn off the model in regions of smooth compressions. The integral is approximated by

$$\begin{aligned} \phi_{1D}(M_s) &= \left(1 - \frac{\overline{u}_{1,d}}{\overline{u}_{1,u}}\right) \int_{\psi=0}^{\pi/2} \frac{\breve{L}}{m} \sin\psi \, d\psi \\ &\approx 1 - \exp\left(-\frac{1}{2\tilde{c}} \sqrt{\max\left(0, \widetilde{R}_{11,shock}\Big|_{\phi_{1D}=1}\right)} \right). \end{aligned} \quad (5.18)$$

A comparison of this fit to the integral from LIA is provided in Figure 5.3, noting that $\widetilde{R}_{ij,shock} \approx \Delta\overline{u}_1^2/4$ in the shock. The final model then reduces to

$$\widetilde{R}_{11,shock} = -\frac{1}{4}\phi_{1D} S_T \sqrt{K} \frac{\partial \tilde{u}_1}{\partial x}. \tag{5.19}$$

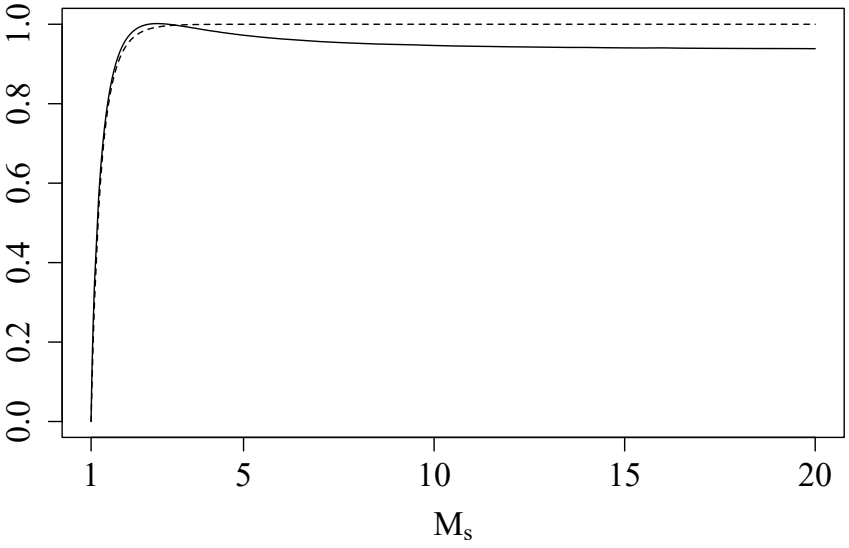

Figure 5.3: Fit of 1-D cutoff function ϕ_{1D} to LIA integral. Solid line : $\left(1 - \frac{\overline{u}_{1,d}}{\overline{u}_{1,u}}\right) \int_{\psi=0}^{\pi/2} \frac{\sqrt{\tilde{L}\tilde{L}^*}}{m} \sin\psi \, d\psi$ calculated from LIA. Dotted line : $1 - \exp\left(-\frac{1}{2\overline{c}_u}\sqrt{\frac{\Delta\overline{u}_1^2}{4}}\right)$.

In (5.18), the $\widetilde{R}_{11,shock}\Big|_{\phi_{1D}=1}$ term denotes (5.19) evaluated with $\phi_{1D} = 1$. The Reynolds averaged $\overline{u}_1$ is modeled by the Favre averaged $\tilde{u}_1$ in (5.19). The original model equations (5.5) and (5.6) suggest that $\overline{u}_1$ and $\tilde{u}_1$ have different profiles within the region of shock corrugation, but under the previous assumption of low M_t, vortical upstream turbulence both Reynolds and Favre averaged velocity fields see the same shock jump and shock width, which implies that the amplitude of the divergence of the averaged velocity field is expected to be similar in each method.

5.3.3 Extension to higher dimensions

The 1-D model (5.19) is extended to higher dimensions by computing the 1-D result as a function of the velocity field divergence and rotating it to align with the shock.

The unit vector normal to the shock, e, may be enforced artificially if it is known a priori, or it may be selected based on a local criteria such as the principal compressive eigenvector of the rate of strain tensor. The cutoff $0 \leq \phi_{3D} \leq 1$ represents some function that goes to 0 away from the shock and takes a value of 1 at the shock. This is introduced as a means to limit the influence of the shock corrugation model in smooth compressions. In many flow configurations the velocity dilatation outside of shocks is small enough that the model will disable itself, but an example of a case where extremely strong smooth compressions arise, requiring careful selection of ϕ_{3D}, is provided in section 5.5.2. The three-dimensional model follows as

$$\widetilde{R}_{ij,shock} = R \begin{pmatrix} \overline{u_k' u_k'} & 0 & 0 \\ 0 & 0 & 0 \\ 0 & 0 & 0 \end{pmatrix} R^T, \tag{5.20a}$$

$$\overline{u_k' u_k'} = -\frac{1}{4} \phi_{3D} S_T \sqrt{K} \frac{\partial \tilde{u}_i}{\partial x_i}, \tag{5.20b}$$

$$R = \begin{pmatrix} 1 - \frac{{e_3}^2}{(e_1+1)} - \frac{{e_2}^2}{(e_1+1)} & -e_2 & -e_3 \\ e_2 & 1 - \frac{{e_2}^2}{(e_1+1)} & -\frac{e_2 e_3}{(e_1+1)} \\ e_3 & -\frac{e_2 e_3}{(e_1+1)} & 1 - \frac{{e_3}^2}{(e_1+1)} \end{pmatrix}. \tag{5.20c}$$

5.4 Energy Equation Closure

DNS of the shock-turbulence interaction [45, 48] have observed that, under averaging, there is a small but significant deviation away from the Euler equation amplifications in primitive quantities as the flow passes through a shock, and this coincides with a change in shock speed relative to the speed an equivalent shock would have in laminar flow. Lele [51] constructed exact jump conditions for the mean variables, but focuses on the effects of the Reynolds stresses when modeling unclosed terms.

The correlations in the energy equation of (5.1) contain contributions from the acoustic and entropy modes of the turbulence that are separate from the Reynolds stresses, and Schwarzkopf et al. [80] models these correlations by the gradient diffusion hypothesis, as gradients of the mean temperature field. These fluctuations are expected to be related to the transported correlations in the model, a_i and b, and an alternative formulation in terms of these existing quantities is desired.

Decomposing the turbulent flow into a linear combination of acoustic and combined vorticity/entropy modes [44], the fluctuating part of a weakly turbulent, single

component fluid field can be split $f' = \dot{f}' + \ddot{f}'$, where $\dot{f}'$ is the fluctuation associated with the acoustic field and $\ddot{f}'$ is associated with the vorticity/entropy field. Acoustic modes and entropy modes move at different velocities, and are assumed to be uncorrelated, $\overline{\dot{f}'\ddot{g}'} = 0$. The thermodynamic fluctuations in acoustic and entropy modes are related by

$$\frac{\ddot{\rho}'}{\overline{\rho}} = \frac{-\ddot{T}'}{\overline{T}}, \tag{5.21a}$$

$$\ddot{p}' = 0, \tag{5.21b}$$

$$\frac{\dot{p}'}{\overline{p}} = \gamma \frac{\dot{\rho}'}{\overline{\rho}}, \tag{5.21c}$$

$$\frac{\dot{\rho}'}{\overline{\rho}} = \frac{1}{\gamma - 1} \frac{\dot{T}'}{\overline{T}}. \tag{5.21d}$$

Expanding the correlations in the energy equation in terms of the individual modes yields

$$\overline{p'u_j'} + \overline{\rho I'' u_j''} = C_v \overline{T} \gamma^2 \overline{\dot{\rho}' \dot{u}_j'} + \overline{\rho' I' u_j'}. \tag{5.22}$$

It is noted that useful relations for converting between fluctuations in Favre and Reynolds averaged quantities may be found in Besnard et al. [7]. In general flows, or when addressing multiple species, (5.22) requires knowledge of the relative influence of the acoustic and entropic components of the turbulence, but in the cases when one of the components can be assumed to dominate the other then (5.22) simplifies to a form that can be written in terms of existing quantities in the model. If the acoustic modes are dominant then

$$\overline{p'u_j'} + \overline{\rho I'' u_j''} \approx C_v \overline{T} \left(\gamma^2 \overline{\rho} a_j + (\gamma - 1) \overline{\rho} \frac{C_\mu}{\sigma_b} S_T \sqrt{K} \frac{\partial b}{\partial x_j} \right), \tag{5.23}$$

and if the entropy modes are dominant then

$$\overline{p'u_j'} + \overline{\rho I'' u_j''} \approx -C_v \overline{T} \overline{\rho} S_T \sqrt{K} \frac{C_\mu}{\sigma_b} \frac{\partial b}{\partial x_j}. \tag{5.24}$$

These relations use the small density fluctuation approximation that $b \approx \overline{\rho'\rho'}/\overline{\rho}^2$ and

$$\frac{\overline{u_j'\rho'\rho'}}{\overline{\rho}^2} \approx -\overline{u_j'\rho'\nu'} \approx \frac{C_\mu}{\sigma_b} S_T \sqrt{K} \frac{\partial b}{\partial x_j}, \tag{5.25}$$

follows from previous derivations in Schwarzkopf et al. [80], where C_μ and σ_b are empirically tuned constants that are left unchanged from the existing model.

The entropy closure (5.24) effectively reduces to a gradient diffusion form in terms of the gradient of b rather than $\overline{T}$, but is otherwise similar to the existing BHR-3 model. The acoustic form (5.23) has an additional contribution to the fluxes, which allows it to directly modify the shock jump relations. Except at low shock Mach numbers $M_s < 1.65$ [49], if the upstream turbulence is purely vortical then LIA suggests that entropy modes are the dominant form of density fluctuations in the far-field downstream of a shock, and so in this study (5.24) is favored over (5.23). LIA predicts that large, exponentially decaying density and pressure fluctuations exist in the region immediately downstream of the shock, but the dynamics of this near-shock region are not captured in BHR-3.

5.5 Model Evaluation

The evaluated modified BHR-3 (mBHR-3) model is summarized by

$$\frac{\partial \overline{\rho}}{\partial t} + \frac{\partial}{\partial x_i}\left(\overline{\rho}\tilde{u}_i\right) = 0, \tag{5.26a}$$

$$\frac{\partial}{\partial t}\left(\overline{\rho}\tilde{u}_i\right) + \frac{\partial}{\partial x_j}\left(\overline{\rho}\tilde{u}_i\tilde{u}_j + \overline{P}\delta_{ij} + \overline{\rho}\left(\widetilde{R}_{ij,shock} + \widetilde{R}_{ij}\right)\right) = 0, \tag{5.26b}$$

$$\begin{aligned}\frac{\partial}{\partial t}\left(\overline{\rho}\tilde{E}\right) + \frac{\partial}{\partial x_j}\left(\overline{\rho}\tilde{u}_j\tilde{E}\right) &= -\frac{\partial}{\partial x_j}\left(\overline{P}\tilde{u}_j\right) - \frac{\partial}{\partial x_j}\left(\overline{\rho}\tilde{u}_j\left(\widetilde{R}_{ij,shock} + \widetilde{R}_{ij}\right)\right) \\ &- \frac{\partial}{\partial x_j}\left(-C_v\overline{T}\frac{C_\mu}{\sigma_b}\overline{\rho}S_T\sqrt{K}\frac{\partial b}{\partial x_j} + \frac{C_\mu\overline{\rho}S_T\sqrt{K}}{\sigma_k}\frac{\partial K}{\partial x_j}\right),\end{aligned} \tag{5.26c}$$

where the shock corrugation effect $\widetilde{R}_{ij,shock}$ is given by (5.20). The constants σ_b, σ_k, and C_μ, and the closure models for $\widetilde{R}_{ij}$, a_i, b, S_T, and S_D are left unchanged from Schwarzkopf et al. [80].

5.5.1 Canonical Shock-Turbulence Interaction

The first case considered is that of a stationary normal shock passing through isotropic turbulence. This flow geometry reduces to one dimension under ensemble averaging, and is a canonical problem that isolates the hydrodynamics associated with a shock passing through turbulent flow, which may occur in more complex problems such as in reshocked Richtmyer-Meshkov instabilities.

The mesh convergence behavior of this simulation is shown in Figure 5.4, which plots the difference in the streamwise Reynolds stress amplification relative to the finest resolution run. The Reynolds stress amplification is defined as the ratio between the Reynolds stress immediately upstream and downstream of the shock, noting that the Reynolds stress components decay monotonically downstream of the

shock in the BHR-3 and mBHR-3 models. The degree of refinement is measured by the non-dimensional parameter $\theta = (S_{T_u} K_u^{1/2})/(\Delta x V_s)$, which scales as a ratio of turbulent to numerical viscosity for shock velocity V_s. The convergence behavior of the BHR-3 model implemented in the xRAGE hydrocode [30] used in Schwarzkopf et al. [80] is also plotted to show that the slow convergence of the BHR-3 model in the presence of shocks is not limited to WENO solvers. As the mesh is refined, the xRAGE implementation transitions from overestimating the fine mesh Reynolds stress amplification to underestimating it, resulting in the abrupt drop in the error near $\theta = 1$. The xRAGE and AMROC implementations of the standard BHR-3 model behave differently on coarse meshes because the interaction is driven by the numerical behavior of the shock, and the codes use different shock stabilization schemes. Both the standard and modified BHR-3 model consistently show slow convergence on coarse grids. Further refinement beyond $\theta > 1$ results in an increasing number of mesh points being present across the shock in the mBHR-3 model, because the large near-shock Reynolds stress in the shock corrugation model begins to fix a shock profile width larger than the mesh-defined shock width produced by WENO. The standard BHR-3 model does appear to eventually converge, but requires mesh resolutions an order of magnitude larger to reach a equivalent degree of convergence at this M_s. It is noted that lower M_s simulations in the standard BHR-3 model show less variation with θ than the $M_s = 5$ case considered here.

Figure 5.5 shows the maximum streamwise Reynolds stress attained at different shock Mach numbers and for upstream conditions with $M_t = 0.22$, using the mBHR-3 model. The shocks are well resolved, with profiles containing at least 10 cells. The streamwise Reynolds stress should take a value of $\Delta\overline{u}_1^2/4$ at the center of the shock [46], and the shock corrugation model reproduces this at higher shock Mach numbers. At very low shock Mach numbers the $\Delta\overline{u}_1^2/4$ approximation becomes inaccurate because the Reynolds stress associated with the turbulence become larger than that associated with the shock corrugation.

Figure 5.6 compares the shock thickness produced in the mBHR-3 model to that observed in DNS [46] and to the root-mean-square (RMS) shock perturbation amplitude predicted in LIA [63]. The shock width is defined in DNS and RANS by the region where the divergence of the mean velocity is at least 5% of its maximum value. The RMS shock perturbation amplitude used for the LIA results should scale with the shock thickness, but will generally be smaller than the full width of the shock profile, which is driven by the largest amplitude perturbations. A factor

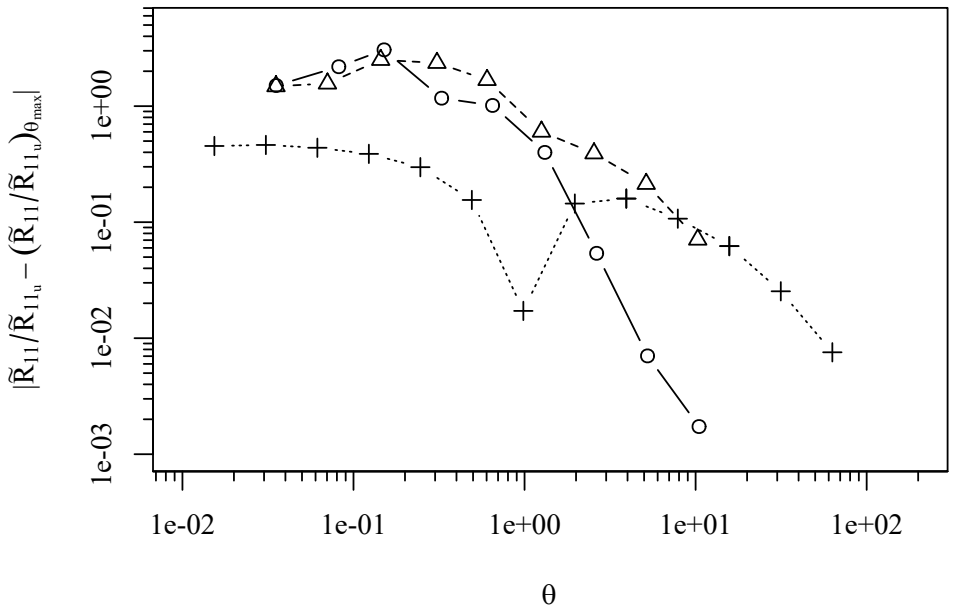

Figure 5.4: Absolute error in the streamwise Reynolds stress amplification in 1-D shock turbulence simulations, with $M_s = 5$. Error is calculated relative to the finest mesh resolution simulation available for the same code and model, which has $\theta_{max} = 21$ in the AMROC simulations and $\theta_{max} = 126$ in the xRAGE simulations, where $\theta = (S_{T_u} K_u^{1/2})/(\Delta x V_s)$. The mesh resolution becomes finer moving from left to right. Circles : mBHR-3 with shock-corrugation and entropic mode transport models. Triangles : standard BHR-3 model. Pluses : standard BHR-3 model, implemented in the xRAGE hydrocode [80].

of 3 is applied to the LIA thickness to compare scaling behavior with the other methods and, if the waves follow a normal distribution, 3 times the RMS amplitude is an approximation of the shock width. The shock thickness is an energy spectrum dependent quantity so the mBHR-3 model cannot be expected to reliably match the quantitative values from LIA and DNS, but the scaling behavior with M_s appears to be consistent between the three methods.

The amplification of the streamwise and transverse Reynolds stresses are shown in Figure 5.7. Simulations are performed with different upstream M_t and one set of simulations are conducted with the shock corrugation model (5.19) set to twice its normal value. The instantaneous jump in Reynolds stress over the shock predicted by the mBHR-3 model appears to be largely unaffected by these parameters. The

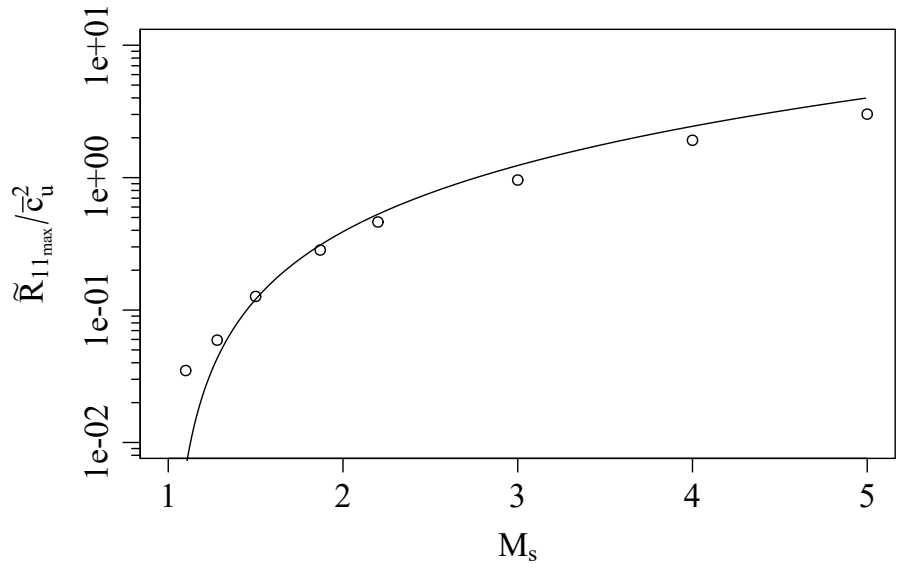

Figure 5.5: Maximum streamwise Reynolds stress attained at the center of a shock, normalized by the upstream sound speed. Circles: mBHR-3 model. Line: $\Delta\overline{u}_1^2/4$ as calculated from the laminar Euler equations.

mBHR-3 model yields lower amplifications than both Schwarzkopf et al. [80] and LIA, but the qualitative behavior of the model remains comparable to LIA. Important features such as the decreasing $\widetilde{R}_{11}$ amplification are still observed in the mBHR-3 model, and re-tuning of constants in the transport equations of the mBHR-3 model would likely improve quantitative agreement with LIA. Precise tuning to match the individual amplifications predicted by LIA may be not be productive, because these predictions have shown only limited agreement with DNS [45, 46].

Figure 5.8 compares the mBHR-3 model against the $Re_\lambda = 40$ DNS of Larsson et al. [46]. The DNS sees a peak in the density immediately downstream of the shock, followed by a rapid but small decrease, and then a gradual rise back towards the Euler jumps. The decreasing mean density downstream of shock is most prominent in the higher M_s cases, and is not captured in the RANS. The mBHR-3 model agrees fairly well with the DNS regarding less complex features such as the shock thickness, overall density amplification, and slowly increasing downstream density.

A difficulty with comparisons such as that shown in Figure 5.8 is that the peak wavenumber k_0 is not well defined in the BHR-3 model, requiring the ad hoc normalization by the transport lengthscale of $k_0 = \pi/S_T$. Larsson et al. [46]

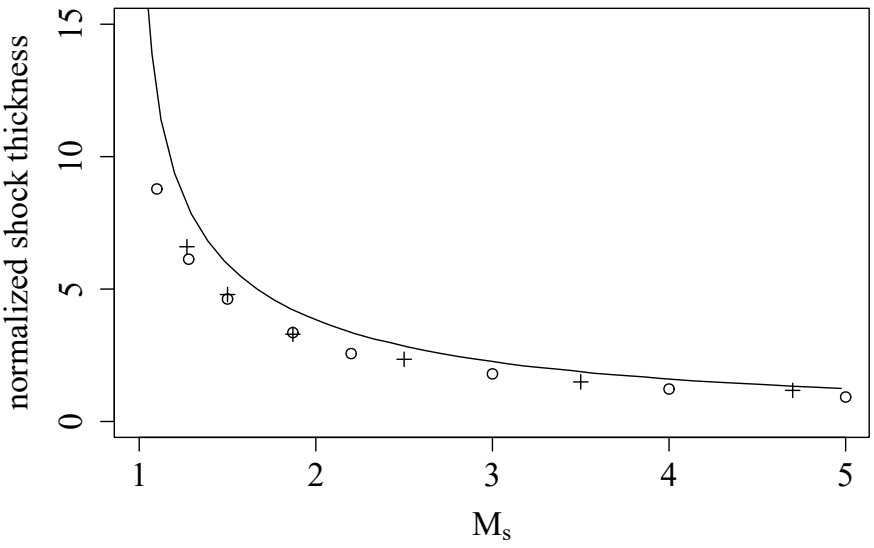

Figure 5.6: Shock thickness from the mBHR-3 model compared to the LIA of Mahesh [63] and $Re_\lambda = 40$ DNS of Larsson et al. [46]. The DNS and RANS have an upstream $M_t = 0.22$. The shock thickness in the DNS and RANS is defined as the region where the divergence of the mean velocity is at least five percent of its maximum value. The DNS is normalized by M_t/k_0, and the mBHR-3 result is normalized by $S_T M_t/\pi$. The LIA result shows the RMS shock perturbation amplitude, normalized by $M_t/(3k_0)$. The factor of 3 applied to the LIA results is included to show the consistent scaling behavior of the methods. Solid line: LIA [63]. Pluses: DNS [46]. Circles: mBHR-3.

propose a normalization by the dissipation lengthscale, defined in the DNS as $S_{D,DNS} = (R_{ii}/2)^{3/2}/\varepsilon$, where ε is the dissipation rate, which provides a direct comparison with RANS models such as BHR-3 but is strongly Reynolds number dependent in low Reynolds number flows. Thus, normalization by the dissipation lengthscale requires the DNS to be conducted at high Reynolds number to be consistent with the assumptions in the RANS models. The DNS with the highest Re_λ that is currently available is plotted in Figure 5.9, for $M_s = 1.5$ and an upstream $Re_\lambda \approx 75$ [46]. The mBHR-3 model shows good agreement with the DNS in this comparison, but it remains unclear if $Re_\lambda = 75$ is sufficiently large for Reynolds number effects in the spatial normalization to become negligible.

The influence of the model for the transport of entropy modes, as discussed in section 5.4, is shown in Figure 5.10. The BHR-3 model is tested with the shock corrugation model active, but with the energy equation correlations modeled by the diffusion

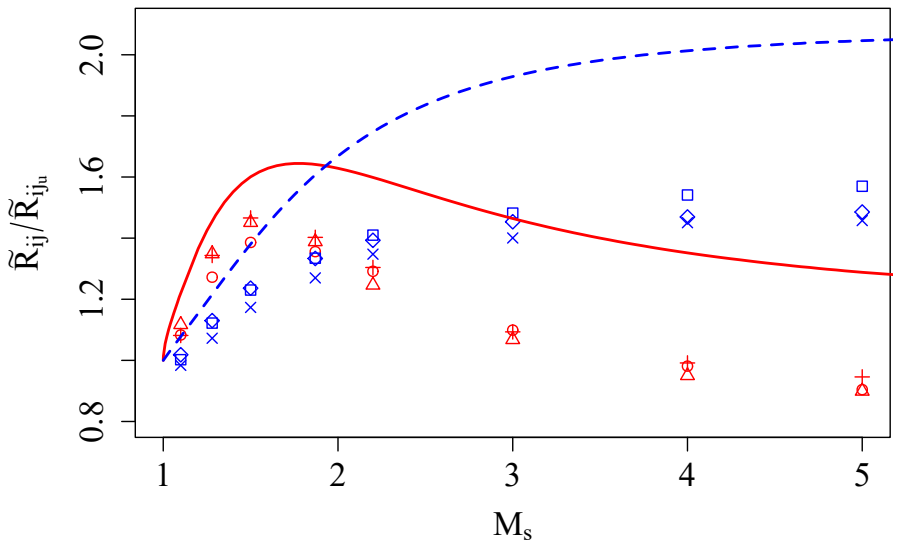

Figure 5.7: Reynolds stress amplifications through a shock. Triangles and circles: mBHR-3 streamwise Reynolds stress at $M_t = 0.1$ and $M_t = 0.22$, respectively. Diamonds and crosses: mBHR-3 transverse Reynolds stress at $M_t = 0.1$ and $M_t = 0.22$. The pluses and squares show the streamwise and transverse Reynolds stresses with $M_t = 0.1$, and $R_{11,shock}$ set to twice its normal value. Solid line: LIA streamwise Reynolds stress. Dashed line: LIA transverse Reynolds stress.

relations used in Schwarzkopf et al. [80] instead of (5.24). The mBHR-3 model using the entropy closure predicts a slightly smaller density jump, but otherwise behaves similarly to the gradient diffusion closure used by Schwarzkopf et al. [80]. Both models capture most of the perturbation from the laminar jump.

At low shock Mach numbers, the closure assuming density fluctuations arise from acoustic modes (5.23) may be more appropriate than the model used in the mBHR-3 model (5.24), which is derived from entropy modes. Figure 5.11 shows that the acoustic closure does perform better at low shock Mach numbers, but begins to overestimate the effect of the turbulence on the jump conditions as the shock Mach number is increased.

5.5.2 Converging Shockwave

Methods such as DNS, where most energetic dynamics of the flow are resolved, often view capturing the shock as only a matter of stably producing the correct jump conditions. Shock capturing schemes may be scrutinized for effects such as

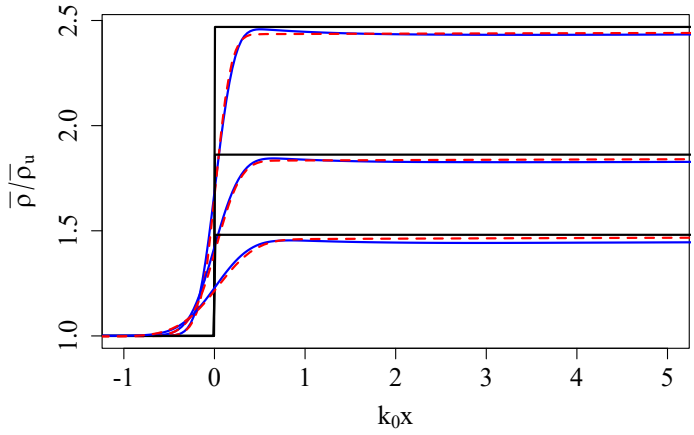

(a)

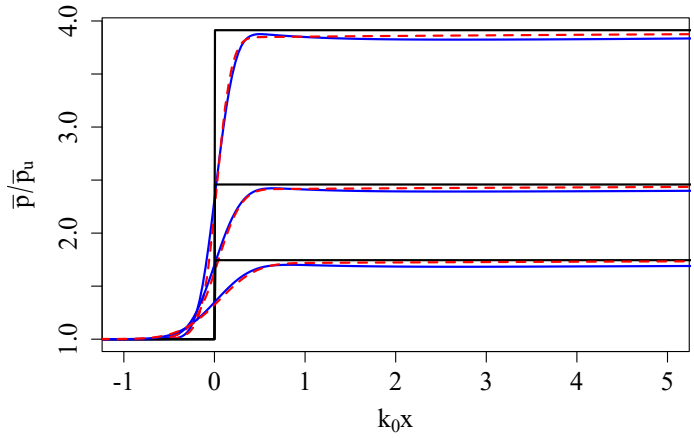

(b)

Figure 5.8: Mean density and pressure profiles in shock-turbulence interactions, with an upstream $M_t = 0.22$. The DNS was performed by Larsson and Lele [45] and has an upstream $Re_\lambda = 40$. The mBHR model uses the normalization $k_0 \approx \pi/S_T$ in the streamwise coordinate. Results are shown for shock Mach numbers of $M_s = 1.28$, $M_s = 1.5$, and $M_s = 1.87$, in order of increasing density and pressure amplification. Solid black lines: laminar Euler equations. Solid blue lines: DNS[45]. Dashed lines: mBHR-3 model.

artificial viscosity, but the failure to resolve the physical shock profile is not usually a concern, as the shock is much thinner than physical scales of interest.

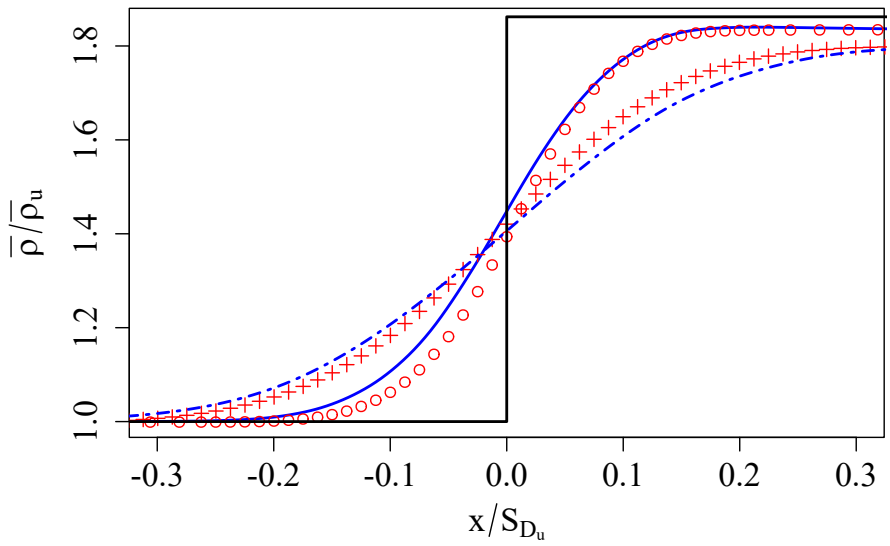

Figure 5.9: Density profiles in shock-turbulence interactions, for a $M_s = 1.5$ shock. The DNS was performed by Larsson et al. [46] and has an upstream $Re_\lambda \approx 75$. Solid line: DNS, $M_t = 0.22$. Circles: mBHR-3 model, $M_t = 0.22$. Dash-dotted line: DNS, $M_t = 0.38$. Pluses: mBHR-3 model, $M_t = 0.38$.

The ensemble-averaged shock width in RANS encodes information about the shape of a shock that is not included elsewhere in the method, and as a result there is more potential for the shock width to play an important role in the physics of a simulation. A practical situation where averaged shock thickness effects may not be negligible arises in Inertial Confinement Fusion (ICF), in which a converging spherical shock is generated by rapidly heating the surface of a fluid pellet. The compression achieved by the shock at the center of the pellet is reduced if the shock is aspherical, which may be caused by fluid instabilities or non-uniformities in the material and heating. A simple hydrodynamical model for this problem is of a converging spherical shock passing through a turbulent flow, and DNS has shown that the corrugated aspherical shock in the turbulent case produces significantly lower compression ratios relative to the spherical shock case [8].

The DNS of Bhagatwala and Lele [8] is reproduced using the mBHR-3 model to evaluate the ability of the RANS to capture the reduced compression resulting from shock corrugation. The simulation is initialized as a spherical shock-tube problem with zero initial velocity and a spherical discontinuity separating regions of constant pressure and density. The states on either side of the discontinuity are

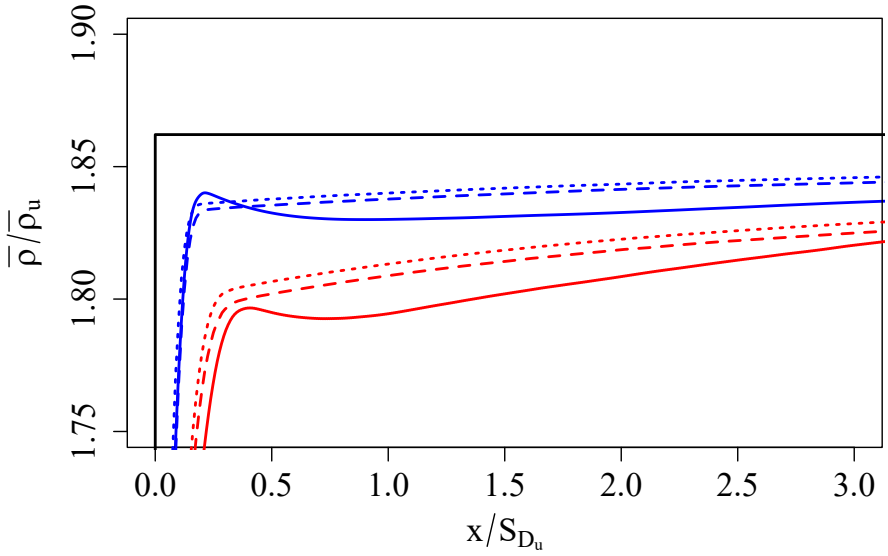

Figure 5.10: Density profiles in shock-turbulence interactions, for a $M_s = 1.5$ shock. The DNS was performed by Larsson et al. [46] and has an upstream $Re_\lambda \approx 75$. The colours indicate the upstream turbulent Mach number. Blue: $M_t = 0.22$. Red: $M_t = 0.38$. The solid black line is the laminar shock jump condition. Solid line: DNS. Dashed line: mBHR-3 model. Dotted line: BHR-3 with the shock corrugation model but not the entropy mode closure.

tuned to generate an inward moving shock with initial shock Mach number M_{s0}, and no contact discontinuity [8]. Simulations are conducted with uniform initial background turbulence intensities of $M_{t0} = 0.4$ and $M_{t0} = 0.8$ in addition to a reference case where no turbulence is present.

The problem contains spherical symmetry in RANS, but is simulated in 3D in order to make comparisons with the numerical procedure used by Bhagatwala and Lele [8], because the DNS was not mesh converged with respect to the maximum compression ratios achieved. The RANS simulations are periodic in all directions, but are completed before the outward moving expansion fan produced by the initial condition reaches the boundary. The mesh is 64^3 on the coarsest level, and with AMR is equivalent to 512^3 on the finest mesh level. The domain has been doubled in size relative to the DNS in order to allow for a longer simulation time before the expansion fan reaches the outer boundaries, and thus the resolution at the center of the converging shock is comparable to the 288^3 resolution used in the DNS.

In the mBHR-3 model of shock corrugation, (5.20), the shock normal, e, is taken to

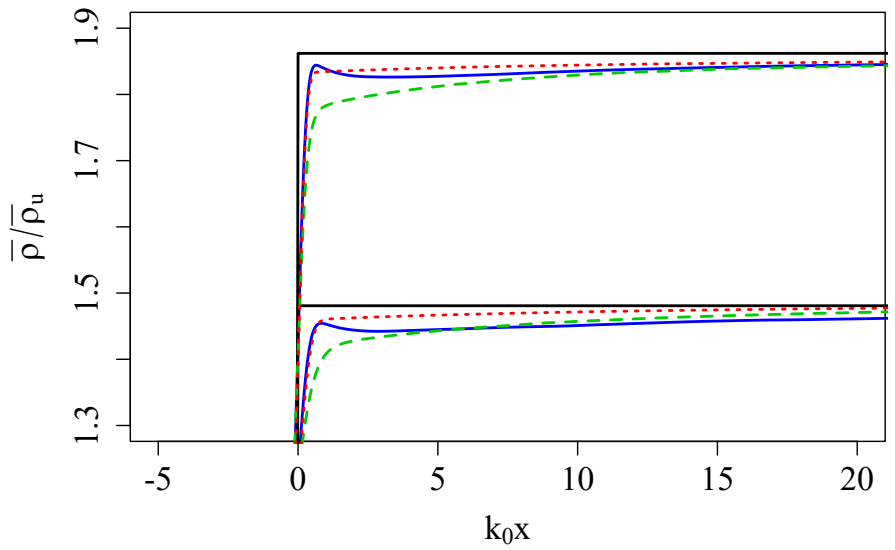

Figure 5.11: Density profiles in shock-turbulence interactions with $M_t = 0.22$. The DNS was performed by Larsson and Lele [45] and has an upstream $Re_\lambda \approx 40$. Results are shown for shock Mach numbers of $M_s = 1.28$ and $M_s = 1.5$, in order of increasing density amplification. The solid black lines are the laminar shock jump condition. Solid line: DNS. Dotted line: mBHR-3 model. Dashed line: mBHR-3 model, using the acoustic closure (5.23) instead of the entropy closure (5.24).

be the radial direction. As the shock converges it accelerates flow towards the center of the domain, and this results in a strong velocity dilatation behind the shock which would erroneously activate the shock corrugation model. The requirement to locally apply a specific method only in the vicinity of a shock is a common occurrence in fluid simulations, but most existing approaches to shock detection, such as slope limiters, are not applicable to the subject model because the shock remains smooth at the grid resolution. The shock corrugation model is disabled in the region of smooth compression by the means of a smooth cutoff function ϕ_{3D},

$$\phi_{3D} = \frac{\phi_{1D}}{2}\left(1 + \tanh\left(40\left[\frac{\sqrt{\max\left(0, \overline{u_k'u_k'}\big|_{\phi_{3D}=1}\right)}}{\tilde{c}} - \frac{\sqrt{\tilde{R}_{kk,M_{s0}}}}{c_0}\right]\right)\right), \tag{5.27}$$

where ϕ_{1D} is given by (5.18) and $\overline{u_k'u_k'}$ is as given in (5.20). The function ϕ_{3D} disables the shock corrugation model if the dilatation is below that expected in a

shock with a given characteristic Mach number. The Reynolds stress associated with this Mach number is taken here to be $\tilde{R}_{kk,M_{s0}} = 0.80\Delta\overline{u}_0^2/4$, where $\Delta\overline{u}_0$ is the velocity jump over a shock of strength M_{s0}, and c_0 is the initial speed of sound at the center of the sphere.

Density profiles from mBHR-3 are shown in Figure 5.12 at various times as the shock converges towards the center of the domain. The times are normalized by t_s, which is given as the time when the shock from the Euler equation solution for laminar flow reaches its maximum pressure. The mBHR-3 model predicts a similar solution to the Euler equations away from the shock, but produces a smoother shock profile as expected. The velocity of the shock is faster in the mBHR-3 simulations due to the presence of turbulence, consistent with the predictions of analytical models of normal shocks [51, 91], and this results in a slightly reduced time to reach peak values in the density and pressure compressions.

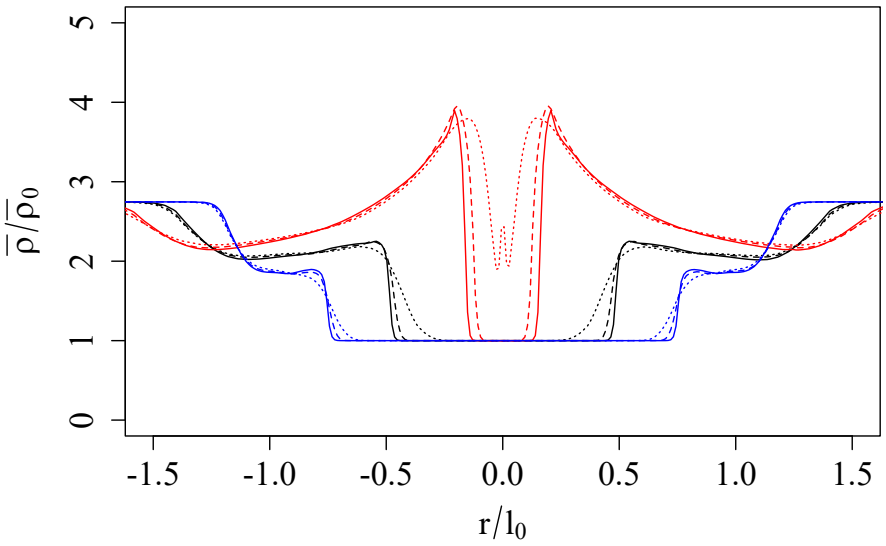

Figure 5.12: Density profiles in converging shock-turbulence interaction. The shock has an initial $M_{s0} = 1.4$ and the turbulence is initialized with a uniform M_{t0}. Density profiles are shown at times $t/t_s = 0.3$ (blue), $t/t_s = 0.6$ (black), and $t/t_s = 0.9$ (red). Solid lines: numerical Euler equations. Dashed lines: mBHR-3, $M_{t0} = 0.4$. Dotted lines: mBHR-3, $M_{t0} = 0.8$.

Table 5.1 shows the peak pressure and densities achieved at the center of the shock for each simulation. These peak values are not numerically resolved, but the ratio of the Euler solution to the turbulent solution has been shown to be approximately mesh

Table 5.1: Maximum amplifications in density and pressure achieved in converging shock simulations. The simulations are initialized with a shock of strength $M_{s0} = 1.4$. The DNS was conducted by Bhagatwala and Lele [8].

	DNS		mBHR-3		
	laminar	$M_{t0} = 0.4$	laminar	$M_{t0} = 0.4$	$M_{t0} = 0.8$
$\rho_{\max}/\rho_0$	20	14	34.2	33.3	27.9
$p_{\max}/p_0$	162	58	193.8	199.2	103.7

independent [8]. The mBHR-3 appears to begin to capture the reduced compression at higher turbulent Mach numbers, but does not resolve a distinguishable effect of the turbulence in the $M_{t0} = 0.4$ case, despite using a comparable mesh to the DNS at the shock center. This is mostly likely the result of dynamics not accounted for in the derivation of the shock corrugation model, which was produced from a statistically steady state analysis of a normal shock. The inherently unsteady converging shock problem sees far larger density amplifications than those possible in the steady normal shock case [8], and this means the dilatation model derived for a normal shock is not guaranteed to be a good approximation for the profile of a spherical shock. Furthermore, the model would not necessarily be expected to capture the time required for a laminar shock to corrugate or a corrugated shock to relax back to a laminar state.

5.6 Discussion

The ensemble-averaged width of a shock passing through turbulence is effectively a measure of the uncertainty in the instantaneous shock position, and thus this profile is much thicker than laminar shock profiles. A model to produce the thick shock profile in RANS is developed from Linear Interaction Analysis (LIA), and introduces an explicit, physically motivated Reynolds stress near the shock which is independent of the computational mesh.

Separately, a simple approximation to connect existing models for the production and transport of density fluctuations with the correlations in the energy equation is proposed. Unlike diffusion closures, this approach allows correlations other than the Reynolds stresses to alter the shock jump conditions, although in practice this appears to only have a notable effect at low M_s, when acoustic modes are significant. The models do not require empirical tuning, but assume a single component perfect gas and require some knowledge of the relative amplitude of entropic and acoustic turbulent modes.

The proposed models are evaluated as a modification to the BHR-3 RANS model of Schwarzkopf et al. [80] but, because the method only directly affects the averaged momentum and energy equations, it is expected that the method could be used in the presence of other closure models. The modified BHR-3 model is shown to accurately reproduce both the shock width and perturbed shock jump conditions observed by DNS in canonical shock-turbulence interactions, and the turbulence amplification over the shock converges on a far coarser mesh relative to the conventional BHR-3 model. Tracking the production and motion of acoustic modes in the turbulence is found to improve the ability of the RANS to capture the modification of the laminar shock jumps at low shock Mach numbers, but the conventional BHR-3 model that only accounts for Reynolds stress effects also does this reasonably well.

The problem of a spherical, converging shock in the presence of turbulence is also considered. Shock asphericity resulting from the turbulence reduces the compression achieved by the imploding shock, and the shock width is a measure of the asphericity in RANS. Compared with DNS, the proposed model appears to underestimate the deleterious effect of the turbulence on the maximum compression, likely due to dynamic effects not accounted for in the derivation of the model.

Chapter 6

CONCLUSIONS

A study of the canonical shock-turbulence problem, in which an isotropic field of turbulence passes through a nearly stationary shock, is conducted at large Taylor-Reynolds numbers. This regime is out of reach of conventional Direct Numerical Simulation (DNS), requiring the Large Eddy Simulation (LES) and Reynolds-Averaged Navier Stokes (RANS) model-based approaches considered here.

Chapter 3 shows that aliasing errors which result in an overestimation of high-wavenumber turbulent energy may be problematic in LES containing a shockwave. As these spurious, high wavenumber eddies cross a shockwave, they are compressed onto even higher wavenumbers by the mean compression of the shock, and may be compressed onto wavenumbers that are not resolved in the LES. This immediately dissipates the eddies and may result in an abrupt change in the behavior of the Subgrid-Scale (SGS) model, yielding non-physical results such as a decrease in the dissipation rate as the flow crosses the shock. A localized dynamic hyperviscous filter that damps out these aliasing errors, while still introducing only a secondary contribution to the overall dissipation, is presented. The resulting Hybrid Stretched-Vortex Model (HSVM) is shown to improve the ability of LES to capture the behavior of DNS in several test problems, such as decaying isotropic turbulence or a LIA-based model for the turbulence downstream of a shock, and also shows improvement to certain statistics in LES of the full canonical shock-turbulence problem.

Chapter 4 then utilizes the HSVM model to produce LES of the canonical shock-turbulence problem. The LES shows good agreement with existing DNS and mesh convergence behavior is evaluated, regarding both the base mesh and localized mesh refinement about the shock. The previous hypothesis that the corrugation of the shock in response to the upstream turbulence must be resolved for the LES to be accurate [26] is explicitly evaluated by showing the LES progresses towards a $k^{-11/3}$ spectrum in the shock corrugation amplitude, as predicted by LIA, as the mesh is resolved. Various statistical correlations computed in the post-shock turbulence are shown to be in close agreement with the predictions of LIA but, as previously seen in lower Reynolds number DNS [e.g. 45, 46], the LES does not agree with the prediction of LIA that the ratio of the Reynolds stresses favors transverse velocity fluctuations

downstream of strong shocks. This is despite the fact that the LES is performed at high Reynolds numbers and low to modest turbulent Mach numbers, conditions under which scaling arguments suggest that LIA should be accurate [76]. Analysis of the inertial range behavior of the turbulence downstream of the shock suggests that the disagreement between LES and LIA arises from the distribution of energy in the Reynolds stresses as a function of scale. LES initialized with a model post-shock field from LIA is shown to rapidly relax to isotropy in the inertial range scales, and because these scales contain a larger fraction of the transverse Reynolds stress than the streamwise Reynolds stress this results in a net transfer of energy towards streamwise velocity fluctuations and produces Reynolds stress anisotropy ratios that favor the streamwise Reynolds stress. Two dimensional measures of anisotropy from the LES of the canonical shock-turbulence problem are found to be inconclusive on their own, but these two-dimensional measures show close agreement between the full shock-turbulence LES and the LIA-initialized LES, suggesting that the latter method, which is more easily analyzed, behaves in an equivalent manner. The response of statistics to changes in various upstream parameters such as the turbulent Mach number or Reynolds number is also evaluated. Reynolds number effects in most statistics are found to be fairly small once an inertial range has developed.

Given the substantial cost of running LES, there is interest in addressing problems such as the canonical shock-turbulence problem in RANS. Chapter 5 addresses a main difficulty of applying RANS to this problem, which is that most conventional RANS models are not guaranteed to converge quickly upon mesh refinement in the presence of a discontinuity such as a shock. Shocks are usually modeled as discontinuities in numerical investigations of fluids because they are typically extremely thin relative to other lengthscales in the flow, but it is argued that a discontinuity may not be an appropriate representation of a shock in turbulent flow in RANS. RANS aims to reproduce mean profiles in the flow, and it is noted that averaged quantities from DNS, such as the mean density, vary in a smooth manner near a shock even when the shock structure is not resolved in the DNS. The corrugation of the shock results in means that are taken as an average over a distribution of possible shock positions, and this results in mean profiles that are smooth at scales much larger than the mean free path. A model to capture the effect of averaging over these random shock corrugations is constructed from LIA, and is used to investigate the behavior of various correlations of interest to RANS near the shock. Furthermore, the large Reynolds stress that results from averaging over shock corrugations is modeled in such a way that it could be implemented

in a practical RANS simulation. RANS using a version of the BHR-3 model [80] modified to include these shock corrugation effects is shown to accurately reproduce the thickness of averaged profiles near a shock, and the convergence properties of the model as the mesh is refined is greatly improved. A RANS simulation of a converging spherical shock in the presence of background turbulence is presented to illustrate a physical application where capturing mean variable profile widths is of interest. DNS has shown the asphericity that results from the passage of the shock through the turbulent flow reduces the compression achieved at the point where the shock converges [8], and the RANS with the shock corrugation model qualitatively captures this reduction in the compression.

Appendix A

LINEAR INTERACTION ANALYSIS

A.1 Introduction

Linear Interaction Analysis (LIA) [63, 66, 72] models the interaction of a shockwave with turbulence by decomposing the upstream field into its component plane waves. The interaction of each wave with the shock is computed analytically under the assumption of small perturbations in the flow field and shock, and the post shock solutions are combined to reconstruct the downstream turbulence. Ryu and Livescu [76] showed shock-resolved DNS converged to LIA-predicted amplifications over the shock as the turbulent Mach number was reduced, and proposed that LIA is valid if the ratio of the shock thickness to the Kolmogorov scale becomes small. Other DNS (e.g. [40, 45, 46]) have found limited agreement to LIA, and the experiments of Barre et al. [4] agree with the amplification of longitudinal velocity fluctuations predicted by LIA. Despite being applicable to a limited regime of flows in very simple geometries, LIA remains a useful tool for the validation of other techniques.

Under the assumption of isotropy or specific forms of anisotropy LIA may be used to calculate a variety of statistics from turbulence as it passes through a shockwave by integrating over the upstream shell-summed energy spectrum [63]. Alternatively, full 3D fields of shocked, turbulent flow may be approximated by applying LIA to the solenoidal part of the Fourier transform of a turbulent field [55, 76]. The resulting flow field is anisotropic, but remains periodic and homogeneous due to the lack of viscous dissipation in the LIA procedure.

A.2 Interaction of a shock with a plane-wave vorticity/entropy disturbance

Ribner [71] showed that the interaction of a single vortical wave with a normal shockwave can be computed analytically when flow variables upstream of the shock and shock deformations are linearized about small perturbations, e.g. $u'_u/V_s << 1$. This was then extended to investigate the interaction of vorticial, isotropic turbulence with a shock by interacting each mode of the turbulence with shock individually [72], and Mahesh [63] further extended this to investigate upstream flow containing both entropic and vorticial modes.

A summary of the method is as follows, but further details may be found in Mahesh

[63]. Consider a single 2D wave in an ideal gas generating small perturbations from the mean of the form

$$\frac{u'_{1,u}}{V_s} = l_u A_v e^{ik(m_u x + l_u y - V_s m t)}, \tag{A.1a}$$

$$\frac{u'_{2,u}}{V_s} = -m_u A_v e^{ik(m_u x + l_u y - V_s m t)}, \tag{A.1b}$$

$$\frac{\rho'_u}{\bar{\rho}_u} = A_e e^{ik(m_u x + l_u y - V_s m_u t)}, \tag{A.1c}$$

$$\frac{T'_u}{\bar{T}_u} = -\frac{\rho'_u}{\bar{\rho}_u}, \tag{A.1d}$$

$$p'_u = 0, \tag{A.1e}$$

$$l_u = \sin\psi_u, \tag{A.1f}$$

$$m_u = \cos\psi_u. \tag{A.1g}$$

Subscript "u" and "d" indicate preshock and postshock values in the shock stationary frame, and ψ_u is the incident angle of the wave with the shock. The amplitudes of the vorticial and entropic modes are A_v and A_e, respectively. The shock passes through the wave as shown in Figure A.1.

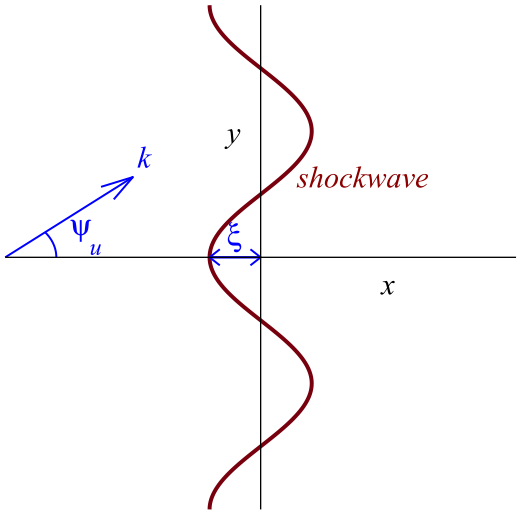

Figure A.1: Domain of Vorticial/Entropic Wave - Shock Interaction

Linearizing the governing equations about the small perturbations, the resulting flow

downstream of the shock can then be shown to be [63]

$$\frac{1}{A_v}\frac{u'_{1,d}}{V_s} = \breve{F}e^{i\breve{k}x}e^{ik(l_u y - V_s m_u t)} + \breve{G}e^{ik(m_u r x + l_u y - V_s m_u t)}, \tag{A.2a}$$

$$\frac{1}{A_v}\frac{u'_{2,d}}{V_s} = \breve{H}e^{i\breve{k}x}e^{ik(l_u y - V_s m_u t)} + \breve{I}e^{ik(m_u r x + l_u y - V_s m_u t)}, \tag{A.2b}$$

$$\frac{1}{A_v}\frac{p'_d}{\bar{p}_d} = \breve{K}e^{i\breve{k}x}e^{ik(l_u y - V_s m_u t)}, \tag{A.2c}$$

$$\frac{1}{A_v}\frac{\rho'_d}{\bar{\rho}_d} = \frac{\breve{K}}{\gamma}e^{i\breve{k}x}e^{ik(l_u y - V_s m_u t)} + \breve{Q}e^{ik(m_u r x + l_u y - V_s m_u t)}, \tag{A.2d}$$

$$\frac{1}{A_v}\frac{T'_d}{\bar{T}_d} = \breve{K}\frac{\gamma-1}{\gamma}e^{i\breve{k}x}e^{ik(l_u y - V_s m_u t)} - \breve{Q}e^{ik(m_u r x + l_u y - V_s m_u t)}, \tag{A.2e}$$

$$\frac{1}{A_v}\frac{1}{V_s}\frac{\partial \xi}{\partial t} = \breve{L}e^{ik(l_u y - V_s m_u t)}, \tag{A.2f}$$

$$\frac{1}{A_v}\frac{1}{V_s}\frac{\partial \xi}{\partial y} = -\frac{l}{m_u}\breve{L}e^{ik(l_u y - V_s m_u t)}. \tag{A.2g}$$

The instantaneous displacement of the shock off of its mean position is given ξ, and the density ratio is $r = \overline{\rho}_d/\overline{\rho}_u$. The downstream flow consists of an acoustic wave, associated with constants $\breve{F}$, $\breve{H}$, and $\breve{K}$, and a vortical/entropic wave associated with $\breve{G}$, $\breve{I}$, and $\breve{Q}$. The value of $\breve{k}$ is imaginary for certain Mach numbers and incident angles, and in these cases the acoustic wave takes the form of an exponentially decaying evanescent wave.

Similarly, the interaction of a acoustic wave with a shock may be calculated [66], although this case in not considered here.

A.3 Integration over a spectrum of upstream turbulence

Mean statistics such as the Reynolds stresses are constructed in LIA by integrating the 2D single wave solutions in spherical coordinates over the spectrum of the upstream turbulence. For comparison of LIA with the inertial range LES discussed in the body of this document, the energy spectrum is selected to be of the form

$$E(k) = \begin{cases} k^2 & 0 \le k < k_0, \\ k_0^2(k/k_0)^{-5/3} & k_0 \le k \le k_{c,LIA}, \\ 0 & k > k_{c,LIA}, \end{cases} \tag{A.3}$$

where k_c is either an appropriate cutoff wavenumber for comparison with the resolved scales of an LES, or a very large number to represent a wide inertial range. The integration is performed by computing the downstream field, (A.2), for every

wavenumber in the energy spectrum of (A.3), with energy distributed between a range of wave orientations ψ_u from the assumption that the upstream turbulence is isotropic. The downstream solutions are then integrated to produce mean statistics in the post-shock flow. The wavenumber associated with energy content in the downstream modes (A.2) is also known, and so energy spectra associated with the downstream flow may also be computed [73].

LIA predicts that far-field amplifications in statistics over the shock are independent of the shape of the upstream energy spectrum, but the spatial variation of the downstream flow depends on the spectrum of the upstream flow. The spectrum (A.3) is qualitatively similar to the spectra developed in forced inertial range turbulence, allowing for comparisons of spectrum dependent quantities such as the near-shock fluctuations and shock corrugation. The implementation of LIA in this document assumes the upstream turbulence consists purely of vorticity modes.

A.4 Application to 3D turbulence

Rather than assuming an isotropic energy spectrum, it is also possible to directly apply LIA to a 3D field of turbulence generated from DNS or LES. A detailed procedure for this is provided in Livescu and Ryu [55], but is summarized here. First, the divergence-free part of the upstream turbulent field is computed in Fourier space by [23]

$$\hat{u}_{i,solenoidal} = \hat{u}_i - \frac{\hat{u}_j k_j}{k_m k_m} k_i. \tag{A.4}$$

This projection isolates the vorticity/entropy modes that are assumed to be upstream of the shock in (A.1). The LIA procedure is simplified if the upstream turbulence does not contain acoustic fluctuations, and so the dilatational part of the velocity field is ignored in this analysis because the pressure fluctuations are small in the upstream turbulence in the scenarios considered in this document. The resulting solenoidal Fourier modes are then rotated to the 2D frame considered in (A.1), and same process of computing the downstream modes given by (A.2) and integrating over the results may be followed as before.

Application of LIA to flow fields from DNS or LES does have the shortcoming that the downstream field may not have a uniform distribution of energy in Fourier space. It is possible that, as LIA computes the interaction of each integer wavenumber mode in the upstream field, it will map little or no energy to specific wavenumbers in the post-shock field. For instance, if the shock corresponds to a factor of two compression, LIA would inject more energy into post-shock modes with even streamwise

wavenumbers than odd streamwise wavenumbers, because odd wavenumbers would correspond to fractional wavenumbers in the upstream flow. Despite this, this form of LIA allows for detailed analysis of shocked flow fields that are out of reach of conventional simulations due to computational cost [76], and avoids the numerical dissipation associated with shock capturing in LES.

Appendix B

MODEL FOR TURBULENT KINETIC ENERGY NEAR A SHOCK

B.1 Convective SGS kinetic energy model

As the flow enters the refined mesh near the shock, all terms in the stretched-vortex SGS model (2.7) remain well defined with the exception of the SGS kinetic energy (2.10), which requires the definition of a cutoff wavenumber k_c. Upstream of the shock, but within the refined mesh, the cutoff wavenumber can be assumed to be equal or close to the cutoff wavenumber of the coarse mesh, because the turbulence does not have time to populate the new wavenumbers opened by mesh refinement as it convects through the narrow band of cells refined in front of the shock. The turbulence is compressed by the shock and mapped towards higher wavenumbers, and thus depending on the shock strength it may fill any number of the high wavenumber modes opened by mesh refinement downstream of the shock. Moreover, the compression from the shock is anisotropic, and a isotropic definition of the cutoff wavenumber may be insufficient. To avoid defining a cutoff wavenumber on the region containing the refined mesh, it is instead assumed that the unresolved kinetic energy remains unchanged through the prolongation process onto the fine mesh. This suggests that a transport model for the SGS turbulent kinetic energy may be useful near the shock.

A transport model for a convection-modeled SGS kinetic energy, $\widetilde{k'_{cm}}$, is introduced to compute the unresolved kinetic energy prior to entering the refined region, and then convect that energy through the region containing the shock using a model of the form

$$\frac{\partial \overline{\rho}\widetilde{k'_{cm}}}{\partial t} + \frac{\partial}{\partial x_j}\left(\overline{\rho}\tilde{u}_j\widetilde{k'_{cm}} - \overline{\nu}\frac{\partial \overline{\rho}\widetilde{k'_{cm}}}{\partial x_j}\right) = \varepsilon_{inject} - \varepsilon_{diss} + \phi_{rc}. \tag{B.1}$$

The left hand side constitutes a conservation law with a resolved shear stress, and the right hand side consists of a source term from the injection of turbulent kinetic energy into the unresolved scales, ε_{inject}, a source term from the dissipation of kinetic energy at the SGS scales, ε_{diss}, and a source term from the rapid compression at the shock, ϕ_{rc}. The injection term is assumed to be equal to the negative of the loss of kinetic energy at the local resolved scales resulting from the stresses in (2.7), with $\tilde{k}'$

calculated from the local resolved structure functions as in (2.10). The dissipation term, ε_{diss}, is taken to be of the same form as the injection but instead dependent on the current amount of energy held in the unresolved scales, namely $\widetilde{k'_{cm}}$. It can be shown that the resolved kinetic energy dissipation arising from (2.7) is

$$\varepsilon = \tilde{S}_{ij}\left(\delta_{ij} - e_i^v e_j^v\right)\tilde{k}', \tag{B.2}$$

and this suggests a model for the convected SGS kinetic energy,

$$\begin{aligned}\frac{\partial \overline{\rho}\widetilde{k'_{cm}}}{\partial t} + \frac{\partial}{\partial x_j}\left(\overline{\rho}\tilde{u}_j\widetilde{k'_{cm}} - \overline{\nu}\frac{\partial \overline{\rho}\widetilde{k'_{cm}}}{\partial x_j}\right) = \\ -\overline{\rho}\tilde{S}_{ij}\left(\delta_{ij} - e_i^v e_j^v\right)\left(\tilde{k}' - \widetilde{k'_{cm}}\right)H(\Delta x) + \phi_{rc}.\end{aligned} \tag{B.3}$$

The switch $H(\Delta x) = 1$ on the coarse mesh, and $H(\Delta x) = 0$ if on a refined mesh. The dissipation and exchange with the resolved scale thus has the effect of forcing $\widetilde{k'_{cm}} \approx \tilde{k}'$ on the coarse mesh, because (B.2) is strictly dissipative with the vortex alignment model for e_i^v that is used in this study [65]. Upon entering the refined region near the shock where $\tilde{k}'$ is not well defined, the source term turns off and the model convects $\widetilde{k'_{cm}}$ downstream through the shock.

B.2 Amplification of the SGS kinetic energy by the shock

The remaining rapid compression term, ϕ_{rc}, is included to ensure the shock amplifies $\widetilde{k'_{cm}}$, as it should amplify all scales of the turbulent flow. The model for ϕ_{rc} selected to enforce that $\widetilde{k'_{cm}}$ is amplified by the far-field predictions of LIA. This is reasonable because the turbulent Mach number associated with $\widetilde{k'_{cm}}$ is small and the Reynolds numbers of the simulations are large, and DNS has generally shown good agreement with LIA regarding turbulent kinetic energy amplification [46]. Furthermore, the SGS flows are small scale and will evolve to their far-field behavior very quickly downstream of the shock.

The method to enforce the LIA predicted amplifications in $\widetilde{k'_{cm}}$ is constructed by decomposing each cell boundary into a one dimensional Riemann problem, as conventionally done in some flux solvers. The evolution of the resulting flow about the boundary between cells centered at x_i and x_{i+1} is shown for one representative case in Figure B.1. The solution of the Riemann problem, giving the types of waves generated at the interface and the flow in the intermediate states (2) and (3), is computed by direct iterative methods. This approach is computationally expensive but this process must only be performed at the shock, corresponding to a small fraction of the domain where WENO is flagged.

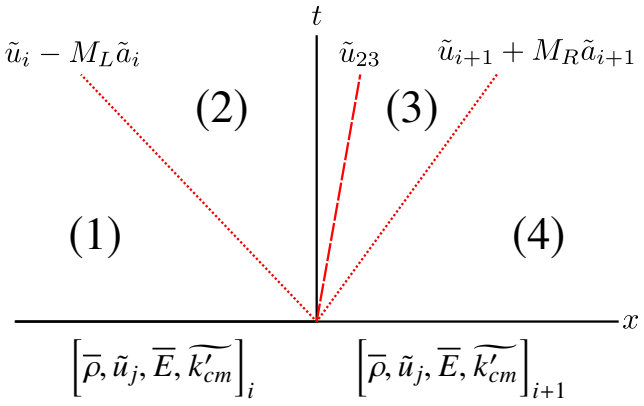

Figure B.1: Two-shock Riemann problem at a cell boundary between cells located at x_i and x_{i+1}. Regions (1) and (4) correspond to unshocked fluid. (2) is fluid initially from cell x_i that has been shocked by the left facing wave, and (3) is from cell x_{i+1} shocked by the right facing wave.

A two-shock solution on the interface between cells centered at x_i and x_{i+1} will be considered here, producing left and right facing shockwaves of Mach numbers M_L and M_R, respectively, and a contact discontinuity moving at velocity $\tilde{u}_{23}$. The case in which one or both of the waves are expansion fans is addressed in the same manner as the two-shock case, except that there is no amplification enforced over the expansions.

The function $\mathcal{L}(M_s)$ is defined as

$$\mathcal{L}(M_s) = \frac{\widetilde{k'}_{cm,post}}{\widetilde{k'}_{cm,0}} - 1, \tag{B.4}$$

where $\widetilde{k'}_{cm,0}$ and $\widetilde{k'}_{cm,post}$ are pre-shock and far-field post-shock kinetic energy from LIA, respectively, such that the subgrid kinetic energy in regions in the intermediate regions (2) and (3) are $\tilde{k}'_{cm,(2)} = \tilde{k}'_{cm,i}(1 + \mathcal{L}(M_L))$ and $\tilde{k}'_{cm,(3)} = \tilde{k}'_{cm,i+1}(1 + \mathcal{L}(M_R))$, respectively. The selection of ϕ_{rc} is set to enforce that, over the duration of one timestep, the subgrid kinetic energy is amplified by the LIA predicted amount, weighted by the fraction of the cell covered by regions (2) and (3). The form of ϕ_{rc} depends on if regions (2) and (3) lie in cell i or $i + 1$, and is given for the possible configurations as

1. $\tilde{u}_i - M_L\tilde{a}_i > 0$ and $\tilde{u}_{i+1} + M_R\tilde{a}_{i+1} > 0$

$$\phi_{rc,i} = 0 \tag{B.5a}$$

$$\phi_{rc,i+1} = \frac{1}{\Delta x}\left((\tilde{u}_{23} - (\tilde{u}_i - M_L\tilde{a}_i))\,\mathcal{L}(M_L)\tilde{k'}_{cm,i} + ((\tilde{u}_{i+1} + M_R\tilde{a}_{i+1}) - \tilde{u}_{23})\mathcal{L}(M_R)\tilde{k'}_{cm,i+1}\right) \tag{B.5b}$$

2. $\tilde{u}_i - M_L\tilde{a}_i < 0$ and $\tilde{u}_{i+1} + M_R\tilde{a}_{i+1} > 0$ and $\tilde{u}_{23} > 0$

$$\phi_{rc,i} = \frac{1}{\Delta x}\left(-(\tilde{u}_i - M_L\tilde{a}_i)\,\mathcal{L}(M_L)\tilde{k'}_{cm,i}\right) \tag{B.6a}$$

$$\phi_{rc,i+1} = \frac{1}{\Delta x}\left(\tilde{u}_{23}\mathcal{L}(M_L)\tilde{k'}_{cm,i} + ((\tilde{u}_{i+1} + M_R\tilde{a}_{i+1}) - \tilde{u}_{23})\mathcal{L}(M_R)\tilde{k'}_{cm,i+1}\right) \tag{B.6b}$$

3. $\tilde{u}_i - M_L\tilde{a}_i < 0$ and $\tilde{u}_{i+1} + M_R\tilde{a}_{i+1} > 0$ and $\tilde{u}_{23} < 0$

$$\phi_{rc,i} = \frac{1}{\Delta x}\left((\tilde{u}_{23} - (\tilde{u}_i - M_L\tilde{a}_i))\,\mathcal{L}(M_L)\tilde{k'}_{cm,i} - \tilde{u}_{23}\mathcal{L}(M_R)\tilde{k'}_{cm,i+1}\right) \tag{B.7a}$$

$$\phi_{rc,i+1} = \frac{1}{\Delta x}\left((\tilde{u}_{i+1} + M_R\tilde{a}_{i+1})\mathcal{L}(M_R)\tilde{k'}_{cm,i+1}\right) \tag{B.7b}$$

4. $\tilde{u}_i - M_L\tilde{a}_i < 0$ and $\tilde{u}_{i+1} + M_R\tilde{a}_{i+1} < 0$

$$\phi_{rc,i} = \frac{1}{\Delta x}\left((\tilde{u}_{23} - (\tilde{u}_i - M_L\tilde{a}_i))\,\mathcal{L}(M_L)\tilde{k'}_{cm,i} + ((\tilde{u}_{i+1} + M_R\tilde{a}_{i+1}) - \tilde{u}_{23})\mathcal{L}(M_R)\tilde{k'}_{cm,i+1}\right) \tag{B.8a}$$

$$\phi_{rc,i+1} = 0 \tag{B.8b}$$

Shocks are nonlinear, and low order numerical shock-capturing schemes that smear a discontinuity across several cell boundaries cannot be expected to be compatible with this approach. The 5th-order WENO solver used here, combined with the moderate shock Mach numbers considered in this report, is sufficiently sharp to give a reasonable amplification in the SGS kinetic energy as it passes through the shock, as shown for a representative case in Figure B.2.

Transport models for the SGS kinetic energy have been employed to control backscatter [29], and this approach may also improve performance when the large scales are temporarily out of equilibrium with the small scales. Unfortunately, for the subject

problem the usefulness of $\tilde{k}'_{cm}$ is limited by the restriction process back onto the coarse mesh downstream of the shock. As shown in Figure B.2, the selection of ϕ_{rc} appears to be effective in enforcing that $\tilde{k}'_{cm}$ approximately agrees with the LIA kinetic energy amplification over a shock. This is the desired result on the refined mesh near the shock because the AMR increases the mesh cutoff wavenumber by a factor greater than the mean compression ratio of the shock, suggesting that all modes that are resolved upstream of the shock are also resolved downstream of the shock within the region of mesh refinement.

The structure function calculation for $\tilde{k}'$ on the coarse mesh sees a noticeably larger amplification, instead matching the kinetic energy amplification from LIA at the unresolved wavenumbers. The LIA result is calculated by performing the full LIA analysis on (3.10) with $k_{c,LIA} = 1024$, and then taking the ratio of the kinetic energy in modes with wavenumbers $k > 128$ in the pre-shock and post-shock field. The amplification in the high wavenumber modes is larger than the full-spectrum result due to the mean flow compression in the shock mapping energy towards larger wavenumbers. In LES on a fixed coarse mesh, the increased amplification is expected, because the shock compresses high wavenumber turbulence onto wavenumbers that the LES does not resolve. The restriction operator from the fine to coarse grid is conservative, and $\tilde{k}'_{cm}$ under-predicts the SGS kinetic energy on the coarse mesh immediately downstream of the shock. In the shown case, $\tilde{k}'_{cm}$ corrects itself fairly quickly, but in low M_t simulations this is not guaranteed. Thus, $\tilde{k}'_{cm}$ is only used in the SGS stresses (2.7) on the refined mesh, and (2.10) is used to calculate the SGS kinetic energy on the coarse mesh. The convection equation for $\tilde{k}'_{cm}$, (B.3), is still computed everywhere in the domain, but is only coupled with the resolved flow equations in within the region of AMR about the shock. Extending $\tilde{k}'_{cm}$ for use in the whole domain would require development of a restriction operator capable of capturing the turbulent kinetic energy lost during restriction from a fine to a coarse mesh.

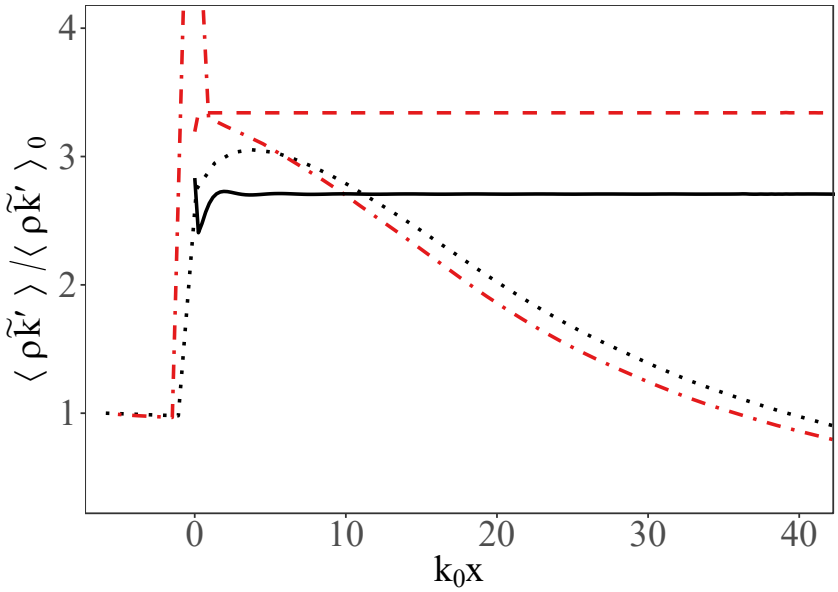

Figure B.2: Amplification in the SGS kinetic energy through a shock. LES results are averaged in time and in the periodic directions. The LES flow conditions are $M_s = 1.5$, $M_t = 0.18$, and $Re_\lambda = 500$ on a $1024 \times 256 \times 256$ base grid, with a factor of 4 refinement at the shock. The LIA results are calculated from (2.10) with $k_{c,LIA} = 1024$. Solid line: LIA kinetic energy amplification. Dashed line: LIA kinetic energy amplification at wavenumbers $k > 128$. Dotted line: convective SGS kinetic energy model $\tilde{k}'_{cm}$. Dash-dotted line: SGS kinetic energy $\tilde{k}'$ calculated from (2.10).

Appendix C

STATISTICS WITHIN THE REGION OF A CORRUGATED SHOCK

Consider the interface between two fluid regions of constant average properties, such that

$$u_1(x, y, z, t) = \overline{u}_{1,u} + \Delta\overline{u}_1 H(x + \xi(y, z, t)) + u'_{turb}(x, y, z, t). \tag{C.1}$$

Specializing the problem to the 2D case of a single vorticity mode passing through the shock, LIA provides the shock surface as

$$\xi = -\frac{1}{mk} L e^{ik\left(ly - \overline{u}_{1,u} mt\right)}, \tag{C.2}$$

where $m = cos(\psi)$ and $l = sin(\psi)$ for a mode of wavenumber k and incident angle ψ with the shock. The field can then be written as

$$u_1(x, y) = \overline{u}_{1,u} + \Delta\overline{u}_1 H\left(x + \frac{L}{m\,k}\cos(k\,l\,y)\right). \tag{C.3}$$

Mean profiles and correlations are of interest, and so the time dependency, which only introduces a phase shift, has been dropped. Likewise, the contribution of u'_{turb} to mean profiles and correlations of interest is small relative the contribution from the shock motion, and so u'_{turb} is subsequently neglected.

The interface is present along the zeros of the argument of H, namely $0 = x + \frac{L}{mk} cos(kly)$. Solving this yields the y-positions, $y_{0,n}$ where the interface crosses a fixed position in x. The three consecutive zeros used in this report are defined as

$$y_{0,1} = \left(-\cos^{-1}\left(\frac{mkx}{L}\right) + \pi\right)\frac{1}{kl}, \tag{C.4a}$$

$$y_{0,2} = \left(\cos^{-1}\left(\frac{mkx}{L}\right) + \pi\right)\frac{1}{kl}, \tag{C.4b}$$

$$y_{0,3} = \left(-\cos^{-1}\left(\frac{mkx}{L}\right) + 3\pi\right)\frac{1}{kl}. \tag{C.4c}$$

The y-averaged profile of $u_1(x, y)$ follows as

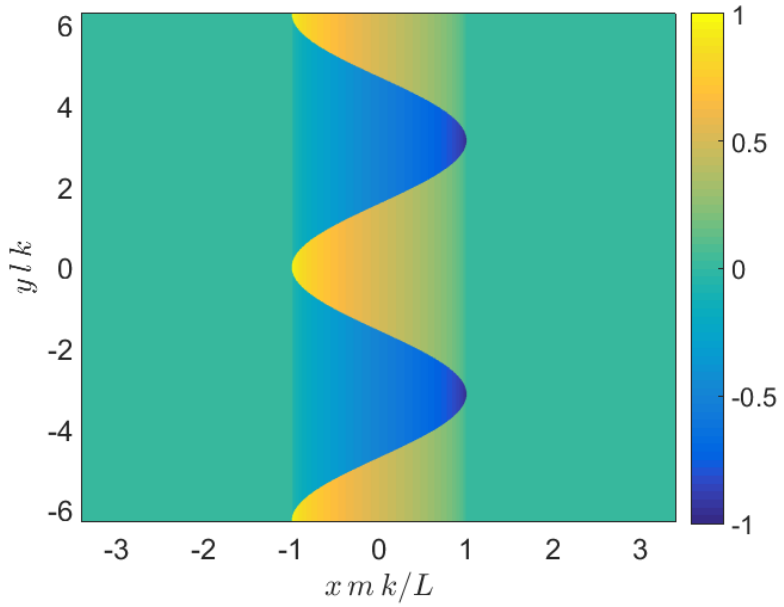

Figure C.1: Fluctuations in the velocity field as given by (C.9), which result from the motion of the shock. The fluctuations are normalized by $\Delta\overline{u}_1$.

$$\overline{u}_1(x) = \frac{1}{y_{0,3} - y_{0,1}} \int_{y_{0,1}}^{y_{0,3}} u_1(x, y) dy, \tag{C.5}$$

$$\overline{u}_1(x) = \frac{1}{y_{0,3} - y_{0,1}} \left(u_{1,u} \left(y_{0,2} - y_{0,1} \right) + u_{1,d} \left(y_{0,3} - y_{0,2} \right) \right), \tag{C.6}$$

$$\overline{u}_1(x) = \frac{1}{2\pi} \left(u_{1,u} \left(2\cos^{-1}\left(\frac{mkx}{L} \right) \right) + u_{1,d} \left(-2\cos^{-1}\left(\frac{mkx}{L} \right) + 2\pi \right) \right), \tag{C.7}$$

$$\overline{u}_1(x) = u_{1,d} - \frac{\Delta\overline{u}_1}{\pi} \cos^{-1}\left(\frac{mkx}{L} \right). \tag{C.8}$$

Defining the fluctuating component of u_1 as $u_1'(x, y) = u_1(x, y) - \overline{u}_1(x)$, then the fluctuations in the pre-shock and post-shock regions are

$$u_{1,u}'(x) = \overline{u}_{1,u} - \overline{u}_1(x) = \frac{-\Delta\overline{u}_1}{\pi} \cos^{-1}\left(\frac{-mkx}{L} \right), \tag{C.9a}$$

$$u_{1,d}'(x) = \overline{u}_{1,d} - \overline{u}_1(x) = \frac{\Delta\overline{u}_1}{\pi} \cos^{-1}\left(\frac{mkx}{L} \right), \tag{C.9b}$$

$$u_1'(x, y) = u_{1,u}'(x) + (u_{1,d}'(x) - u_{1,u}'(x)) H\left(x + \frac{L}{m\,k} \cos(k\,l\,y) \right). \tag{C.9c}$$

The spatial distribution of the fluctuations, (C.9), is plotted in Figure C.1.

The resulting streamwise Reynolds stress is $\overline{u_1' u_1'}(x)$, where

$$\overline{u_1' u_1'}(x) = \frac{1}{y_{0,3} - y_{0,1}} \int_{y_{0,1}}^{y_{0,3}} u_1'(x,y) u_1'(x,y) dy, \tag{C.10}$$

$$\overline{u_1' u_1'}(x) = \frac{1}{y_{0,3} - y_{0,1}} \left(u_{1,u}' u_{1,u}' \left(y_{0,2} - y_{0,1} \right) + u_{1,d}' u_{1,d}' \left(y_{0,3} - y_{0,2} \right) \right), \tag{C.11}$$

$$\begin{aligned} \overline{u_1' u_1'}(x) = \frac{1}{2\pi} \left(\frac{\Delta \overline{u}_1}{\pi} \right)^2 \Bigg[\cos^{-1} \left(\frac{-mkx}{L} \right)^2 \left(2 \cos^{-1} \left(\frac{mkx}{L} \right) \right) + \\ \cos^{-1} \left(\frac{mkx}{L} \right)^2 \left(-2 \cos^{-1} \left(\frac{mkx}{L} \right) + 2\pi \right) \Bigg], \end{aligned} \tag{C.12}$$

$$\begin{aligned} \overline{u_1' u_1'}(x) = \frac{\Delta \overline{u}_1^2}{\pi^3} \cos^{-1} \left(\frac{-mkx}{L} \right) \cos^{-1} \left(\frac{mkx}{L} \right) \\ \times \left(\cos^{-1} \left(\frac{mkx}{L} \right) + \cos^{-1} \left(\frac{-mkx}{L} \right) \right). \end{aligned} \tag{C.13}$$

The Favre-averaged Reynolds stress is given by

$$\begin{aligned} \frac{\overline{\rho u_1'' u_1''}}{\overline{\rho}} = \frac{1}{\left(y_{0,3} - y_{0,1} \right) \overline{\rho}(x)} \Big(\rho_u u_{1,u}'' u_{1,u}'' \left(y_{0,2} - y_{0,1} \right) \\ + \rho_d u_{1,d}'' u_{1,d}'' \left(y_{0,3} - y_{0,2} \right) \Big). \end{aligned} \tag{C.14}$$

$$\begin{aligned} \frac{\overline{\rho u_1'' u_1''}}{\overline{\rho}} = \frac{1}{\left(y_{0,3} - y_{0,1} \right) \overline{\rho}(x)} \Bigg[\rho_u \left(u_{1,u}' - \frac{\overline{\rho' u_1'}(x)}{\overline{\rho}(x)} \right)^2 \left(y_{0,2} - y_{0,1} \right) \\ + \rho_d \left(u_{1,d}' - \frac{\overline{\rho' u_1'}(x)}{\overline{\rho}(x)} \right)^2 \left(y_{0,3} - y_{0,2} \right) \Bigg]. \end{aligned} \tag{C.15}$$

The streamwise density-velocity correlation, $\overline{\rho' u_1'}(x)$, is computed in the same manner as (C.13), yielding

$$\begin{aligned} \overline{\rho' u_1'}(x) = \frac{\Delta \overline{\rho} \Delta \overline{u}_1}{\pi^3} \cos^{-1} \left(\frac{-mkx}{L} \right) \cos^{-1} \left(\frac{mkx}{L} \right) \\ \times \left(\cos^{-1} \left(\frac{mkx}{L} \right) + \cos^{-1} \left(\frac{-mkx}{L} \right) \right), \end{aligned} \tag{C.16}$$

and $\overline{\rho}(x)$ follows the same form as (C.8). Evaluating (C.15) using (C.8), (C.9), and (C.16) yields an equation for the Favre-averaged Reynolds stress,

$$\frac{\overline{\rho u_1'' u_1''}}{\overline{\rho}} = \frac{\overline{\rho}_u \, \overline{\rho}_d \, \Delta \overline{u}_1^2 \, \cos^{-1} \left(\frac{k\,m\,x}{L} \right) \cos^{-1} \left(\frac{-k\,m\,x}{L} \right)}{\left(\overline{\rho}_u \cos^{-1} \left(\frac{k\,m\,x}{L} \right) + \overline{\rho}_d \cos^{-1} \left(\frac{-k\,m\,x}{L} \right) \right)^2}. \tag{C.17}$$

The derivations of Favre-averaged profiles such as (C.17) is tedious but straightforward to perform in symbolic manipulation software such as Maple or Mathematica. In addition to the Reynold stresses, the fluctuating pressure dilatation $\nabla \cdot \overline{p'u'}$ also become large near the shock. From the previous derivation of (C.13) it follows that

$$\overline{p'u'}(x) = \frac{\Delta u \Delta p}{\pi^3} \cos^{-1}\left(\frac{-mkx}{L}\right) \cos^{-1}\left(\frac{mkx}{L}\right) \times \left(\cos^{-1}\left(\frac{mkx}{L}\right) + \cos^{-1}\left(\frac{-mkx}{L}\right)\right). \tag{C.18}$$

The velocity triple correlation $\overline{\rho u_1' u_1' u_1'}$ also appears in some Reynolds averaged models. Averaging the fluctuations computed from (C.9), it can be shown that

$$\overline{u_1' u_1' u_1'}(x) = \frac{1}{y_{0,3} - y_{0,1}} \int_{y_{0,1}}^{y_{0,3}} u_1'(x, y) u_1'(x, y) u_1'(x, y) dy, \tag{C.19}$$

$$\overline{u_1' u_1' u_1'} = \frac{\Delta u^3}{\pi^3} \cos^{-1}\left(\frac{mkx}{L}\right) \cos^{-1}\left(\frac{-mkx}{L}\right) \left(2\cos^{-1}\left(\frac{mkx}{L}\right) - \pi\right). \tag{C.20}$$

BIBLIOGRAPHY

[1] N. A. Adams and S. Stolz. A subgrid-scale deconvolution approach for shock capturing. *Journal of Computational Physics*, 178(2):391–426, 2002.

[2] J. H. Agui, G. Briassulis, and Y. Andreopoulos. Studies of interactions of a propagating shock wave with decaying grid turbulence: velocity and vorticity fields. *Journal of Fluid Mechanics*, 524:143–195, 2005.

[3] Y. Andreopoulos, J. H. Agui, and G. Briassulis. Shock wave—turbulence interactions. *Annual Review of Fluid Mechanics*, 32(1):309–345, 2000.

[4] S. Barre, D. Alem, and J. P. Bonnet. Experimental study of a normal shock/homogeneous turbulence interaction. *AIAA journal*, 34(5):968–974, 1996.

[5] G. K. Batchelor. *The theory of homogeneous turbulence*. Cambridge university press, 1953.

[6] I. Bermejo-Moreno, J. Larsson, and S. K. Lele. LES of canonical shock-turbulence interaction. *Annual Research Briefs, Stanford University*, pages 209–222, 2010.

[7] D. Besnard, F. H. Harlow, R. M. Rauenzahn, and C. Zemach. Turbulence transport equations for variable-density turbulence and their relationship to two-field models. *NASA STI/Recon Technical Report N*, 92, June 1992.

[8] A. Bhagatwala and S. K. Lele. Interaction of a converging spherical shock wave with isotropic turbulence. *Physics of Fluids*, 24(8):035103, 2012.

[9] G. A. Blaisdell. *Numerical simulation of compressible homogeneous turbulence*. PhD thesis, Stanford University, 1991.

[10] V. Borue and S. A. Orszag. Numerical study of three-dimensional Kolmogorov flow at high Reynolds numbers. *Journal of Fluid Mechanics*, 306:293–323, 1996.

[11] N. O. Braun, D. I. Pullin, and D. I. Meiron. Regularization method for large eddy simulations of shock-turbulence interactions. *Journal of Computational Physics*, 361:231–246, 2018.

[12] C.-T. Chang. Interaction of a plane shock and oblique plane disturbances with special reference to entropy waves. *Journal of the Aeronautical Sciences*, 24 (9):675–682, 1957.

[13] D. Chung and D. I. Pullin. Large-eddy simulation and wall modelling of turbulent channel flow. *Journal of fluid mechanics*, 631:281–309, 2009.

[14] D. Chung and D. I. Pullin. Direct numerical simulation and large-eddy simulation of stationary buoyancy-driven turbulence. *Journal of Fluid Mechanics*, 643:279–308, 2010.

[15] M. K. Chung and S. K. Kim. A nonlinear return-to-isotropy model with reynolds number and anisotropy dependency. *Physics of Fluids*, 7(6):1425–1437, 1995.

[16] A. W. Cook and W. H. Cabot. A high-wavenumber viscosity for high-resolution numerical methods. *Journal of Computational Physics*, 195(2):594–601, 2004.

[17] A. W. Cook and W. H. Cabot. Hyperviscosity for shock-turbulence interactions. *Journal of Computational Physics*, 203(2):379–385, 2005.

[18] G. Dantinne, H. Jeanmart, G. S. Winckelmans, V. Legat, and D. Carati. Hyperviscosity and vorticity-based models for subgrid scale modeling. *Applied Scientific Research*, 59(4):409–420, 1997.

[19] R. Deiterding, R. Radovitzky, S. P. Mauch, L. Noels, J. C. Cummings, and D. I. Meiron. A virtual test facility for the efficient simulation of solid material response under strong shock and detonation wave loading. *Engineering with Computers*, 22(3-4):325–347, 2006.

[20] P. E. Dimotakis. The mixing transition in turbulent flows. *Journal of Fluid Mechanics*, 409:69–98, 2000.

[21] T. Dubois, J. A. Domaradzki, and A. Honein. The subgrid-scale estimation model applied to large eddy simulations of compressible turbulence. *Physics of Fluids*, 14(5):1781–1801, 2002.

[22] F. Ducros, V. Ferrand, F. Nicoud, C. Weber, D. Darracq, C. Gacherieu, and T. Poinsot. Large-eddy simulation of the shock/turbulence interaction. *Journal of Computational Physics*, 152(2):517–549, 1999.

[23] G. Erlebacher, M. Y. Hussaini, H. O. Kreiss, and S. Sarkar. The analysis and simulation of compressible turbulence. *Theoretical and Computational Fluid Dynamics*, 2(2):73–95, 1990.

[24] J. B. Freund. Proposed inflow/outflow boundary condition for direct computation of aerodynamic sound. *AIAA journal*, 35(4):740–742, 1997.

[25] E. Garnier, M. Mossi, P. Sagaut, P. Comte, and M. Deville. On the use of shock-capturing schemes for large-eddy simulation. *Journal of Computational Physics*, 153(2):273–311, 1999.

[26] E. Garnier, P. Sagaut, and M. Deville. Large eddy simulation of shock/homogeneous turbulence interaction. *Computers & fluids*, 31(2):245–268, 2002.

[27] M. Germano, U. Piomelli, P. Moin, and W. H. Cabot. A dynamic subgrid-scale eddy viscosity model. *Physics of Fluids A: Fluid Dynamics*, 3(7):1760–1765, 1991.

[28] S. Ghosal. An analysis of numerical errors in large-eddy simulations of turbulence. *Journal of Computational Physics*, 125(1):187–206, 1996.

[29] S. Ghosal, T. S. Lund, P. Moin, and K. Akselvoll. A dynamic localization model for large-eddy simulation of turbulent flows. *Journal of Fluid Mechanics*, 286: 229–255, 1995.

[30] M. Gittings, R. Weaver, M. Clover, T. Betlach, N. Byrne, R. Coker, E. Dendy, R. Hueckstaedt, K. New, W. R. Oakes, et al. The RAGE radiation-hydrodynamic code. *Computational Science & Discovery*, 1(1):015005, 2008.

[31] S. Gottlieb, C. W. Shu, and E. Tadmor. Strong stability-preserving high-order time discretization methods. *SIAM review*, 43(1):89–112, 2001.

[32] O. Grégoire, D. Souffland, and S. Gauthier. A second-order turbulence model for gaseous mixtures induced by Richtmyer-Meshkov instability. *Journal of Turbulence*, (6):N29, 2005.

[33] J. Griffond and O. Soulard. Evaluation of augmented RSM for interaction of homogeneous turbulent mixture with shock and rarefaction waves. *Journal of Turbulence*, 15(9):569–595, 2014.

[34] J. Griffond, O. Soulard, and D. Souffland. A turbulent mixing Reynolds stress model fitted to match linear interaction analysis predictions. *Physica Scripta*, 2010(T142):014059, 2010.

[35] S. Hickel, C. P. Egerer, and J. Larsson. Subgrid-scale modeling for implicit large eddy simulation of compressible flows and shock-turbulence interaction. *Physics of Fluids*, 26(10):106101, 2014.

[36] D. J. Hill and D. I. Pullin. Hybrid tuned center-difference-WENO method for large eddy simulations in the presence of strong shocks. *Journal of Computational Physics*, 194(2):435 – 450, 2004. ISSN 0021-9991.

[37] D. J. Hill, C. Pantano, and D. I. Pullin. Large-eddy simulation and multiscale modelling of a Richtmyer–Meshkov instability with reshock. *Journal of fluid mechanics*, 557:29–61, 2006.

[38] A. E. Honein and P. Moin. Higher entropy conservation and numerical stability of compressible turbulence simulations. *Journal of Computational Physics*, 201(2):531–545, 2004.

[39] L. Jacquin, C. Cambon, and E. Blin. Turbulence amplification by a shock wave and rapid distortion theory. *Physics of Fluids A: Fluid Dynamics*, 5(10): 2539–2550, 1993.

[40] S. Jamme, J.-B. Cazalbou, F. Torres, and P. Chassaing. Direct numerical simulation of the interaction between a shock wave and various types of isotropic turbulence. *Flow, Turbulence and Combustion*, 68(3):227–268, 2002.

[41] J. Jiménez. Hyperviscous vortices. *Journal of Fluid Mechanics*, 279:169–176, 1994.

[42] T. Kitamura, K. Nagata, Y. Sakai, A. Sasoh, and Y. Ito. Changes in divergence-free grid turbulence interacting with a weak spherical shock wave. *Physics of Fluids*, 29(6):065114, 2017.

[43] B. Kosović, D. I. Pullin, and R. Samtaney. Subgrid-scale modeling for large-eddy simulations of compressible turbulence. *Physics of Fluids (1994-present)*, 14(4):1511–1522, 2002.

[44] L. S.G. Kovasznay. Turbulence in supersonic flow. *Journal of the Aeronautical Sciences*, 20(10):657–674, 1953.

[45] J. Larsson and S. K. Lele. Direct numerical simulation of canonical shock/turbulence interaction. *Physics of Fluids*, 21(12):126101, 2009.

[46] J. Larsson, I. Bermejo-Moreno, and S. K. Lele. Reynolds-and Mach-number effects in canonical shock–turbulence interaction. *Journal of Fluid Mechanics*, 717:293–321, 2013.

[47] S. Lee. Large eddy simulation of shock turbulence interaction. *Annual Research Briefs, Stanford University*, 1992.

[48] S. Lee, S. K. Lele, and P. Moin. Direct numerical simulation of isotropic turbulence interacting with a weak shock wave. *Journal of Fluid Mechanics*, 251:533–562, 1993.

[49] S. Lee, S. K. Lele, and P. Moin. Interaction of isotropic turbulence with shock waves: effect of shock strength. *Journal of Fluid Mechanics*, 340:225–247, 1997.

[50] S. K. Lele. Compact finite difference schemes with spectral-like resolution. *Journal of computational physics*, 103(1):16–42, 1992.

[51] S. K. Lele. Shock-jump relations in a turbulent flow. *Physics of Fluids A: Fluid Dynamics*, 4(12):2900–2905, 1992.

[52] R. J. LeVeque. *Finite volume methods for hyperbolic problems*, volume 31. Cambridge university press, 2002.

[53] X.-D. Liu, S. Osher, and T. Chan. Weighted essentially non-oscillatory schemes. *Journal of computational physics*, 115(1):200–212, 1994.

[54] D. Livescu and J.R. Ristorcelli. Variable-density mixing in buoyancy-driven turbulence. *Journal of Fluid Mechanics*, 605:145–180, 2008.

[55] D. Livescu and J. Ryu. Vorticity dynamics after the shock–turbulence interaction. *Shock Waves*, 26(3):241–251, 2016.

[56] D. Livescu, J. R. Ristorcelli, R. A. Gore, S. H. Dean, W. H. Cabot, and A. W. Cook. High-reynolds number rayleigh–taylor turbulence. *Journal of Turbulence*, (10):N13, 2009.

[57] D. l. Livescu and Z. Li. Subgrid-scale backscatter after the shock-turbulence interaction. In *AIP Conference Proceedings*, volume 1793, page 150009. AIP Publishing, 2017.

[58] M. Lombardini. *Richtmyer-Meshkov instability in converging geometries*. PhD thesis, California Institute of Technology, 2008.

[59] M. Lombardini, D.J. Hill, D. I. Pullin, and D. I. Meiron. Atwood ratio dependence of Richtmyer–Meshkov flows under reshock conditions using large-eddy simulations. *Journal of fluid mechanics*, 670:439–480, 2011.

[60] M. Lombardini, D. I. Pullin, and D. I. Meiron. Transition to turbulence in shock-driven mixing: a Mach number study. *Journal of Fluid Mechanics*, 690: 203–226, 2012.

[61] J. L. Lumley. Computational modeling of turbulent flows. 18:123–176, 1979.

[62] T. S. Lundgren. Strained spiral vortex model for turbulent fine structure. *Physics of Fluids (1958-1988)*, 25(12):2193–2203, 1982.

[63] K. Mahesh. *The interaction of a shock wave with a turbulent shear flow*. PhD thesis, Stanford University, 1996.

[64] K. Mahesh, S. K. Lele, and P. Moin. The influence of entropy fluctuations on the interaction of turbulence with a shock wave. *Journal of Fluid Mechanics*, 334(1):353–379, 1997.

[65] A. Misra and D. I. Pullin. A vortex-based subgrid stress model for large-eddy simulation. *Physics of Fluids (1994-present)*, 9(8):2443–2454, 1997.

[66] F. K. Moore. Unsteady oblique interaction of a shock wave with a plane disturbance. 1954.

[67] R. D. Moser. On the validity of the continuum approximation in high reynolds number turbulence. *Physics of Fluids*, 18(7):078105, 2006.

[68] M. R. Petersen and D. Livescu. Forcing for statistically stationary compressible isotropic turbulence. *Physics of Fluids*, 22(11):116101, 2010.

[69] S. B. Pope. *Turbulent flows*. Cambridge University Press, 2000.

[70] D. I. Pullin and P. G. Saffman. Reynolds stresses and one-dimensional spectra for a vortex model of homogeneous anisotropic turbulence. *Physics of Fluids*, 6(5):1787–1796, 1994.

[71] H. S. Ribner. Convection of a pattern of vorticity through a shock wave. Technical report, NACA TN-2864, 1953.

[72] H. S. Ribner. Shock-turbulence interaction and the generation of noise. Technical report, NACA TN-3255, 1954.

[73] H. S. Ribner. Spectra of noise and amplified turbulence emanating from shock-turbulence interaction: Two scenarios. Technical report, University of Toronto, 1986.

[74] H. S. Ribner. Spectra of noise and amplified turbulence emanating from shock-turbulence interaction. *AIAA J*, 25(3):436–442, 1986.

[75] R. S. Rogallo and P. Moin. Numerical simulation of turbulent flows. *Annual review of fluid mechanics*, 16(1):99–137, 1984.

[76] J. Ryu and D. Livescu. Turbulence structure behind the shock in canonical shock–vortical turbulence interaction. *Journal of Fluid Mechanics*, 756:R1, 2014.

[77] R. Samtaney, D. I. Pullin, and B. Kosovic. Direct numerical simulation of decaying compressible turbulence and shocklet statistics. *Physics of Fluids*, 13(5):1415–1430, 2001.

[78] S. Sarkar and C. G. Speziale. A simple nonlinear model for the return to isotropy in turbulence. *Physics of Fluids A: Fluid Dynamics*, 2(1):84–93, 1990.

[79] J. D. Schwarzkopf, D. Livescu, R. A. Gore, R. M. Rauenzahn, and J. R. Ristorcelli. Application of a second-moment closure model to mixing processes involving multicomponent miscible fluids. *Journal of Turbulence*, (12):N49, 2011.

[80] J. D. Schwarzkopf, D. Livescu, J. R. Baltzer, R. A. Gore, and J. R. Ristorcelli. A two-length scale turbulence model for single-phase multi-fluid mixing. *Flow, Turbulence and Combustion*, 96(1):1–43, 2016.

[81] K. Sinha. Evolution of enstrophy in shock/homogeneous turbulence interaction. *Journal of Fluid Mechanics*, 707:74–110, 2012.

[82] K. Sinha and S. J. Balasridhar. Conservative formulation of the k-ϵ turbulence model for shock–turbulence interaction. *AIAA journal*, 2013.

[83] K. Sinha, K. Mahesh, and G. V. Candler. Modeling shock unsteadiness in shock/turbulence interaction. *Physics of fluids*, 15(8):2290–2297, 2003.

[84] T. Tantikul and J.A. Domaradzki. Large eddy simulations using truncated navier–stokes equations with the automatic filtering criterion. *Journal of Turbulence*, (11):N21, 2010.

[85] Y. Tian, F. A. Jaberi, Z. Li, and D. Livescu. Numerical study of variable density turbulence interaction with a normal shock wave. *Journal of Fluid Mechanics*, 829:551–588, 2017.

[86] J. Towns, T. Cockerill, M. l. Dahan, I. Foster, K. Gaither, A. Grimshaw, V. Hazlewood, S. Lathrop, D. Lifka, G. D. Peterson, et al. XSEDE: accelerating scientific discovery. *Computing in Science & Engineering*, 16(5):62–74, 2014.

[87] V. K. Tritschler, B. J. Olson, S. K. Lele, S. Hickel, X. Y. Hu, and N. A. Adams. On the Richtmyer–Meshkov instability evolving from a deterministic multimode planar interface. *Journal of Fluid Mechanics*, 755:429–462, 2014.

[88] J. B. Vemula and K. Sinha. Reynolds stress models applied to canonical shock-turbulence interaction. *Journal of Turbulence*, 18(7):653–687, 2017.

[89] T. Voelkl, D. I. Pullin, and D. C. Chan. A physical-space version of the stretched-vortex subgrid-stress model for large-eddy simulation. *Physics of Fluids*, 12(7), 2000.

[90] J. G. Wouchuk, C. Huete Ruiz de Lira, and A. L. Velikovich. Analytical linear theory for the interaction of a planar shock wave with an isotropic turbulent vorticity field. *Phys. Rev. E*, 79:066315, Jun 2009. doi: 10.1103/PhysRevE.79.066315.

[91] G. P. Zank, Y. Zhou, W. H. Matthaeus, and W.K.M. Rice. The interaction of turbulence with shock waves: A basic model. *Physics of Fluids*, 14(11):3766–3774, 2002.